University of California
Los Angeles

Electronic properties of organic photovoltaic materials

A dissertation submitted in partial satisfaction
of the requirements for the degree
Doctor of Philosophy in Chemistry

by

Christopher David Arntsen

2014

Abstract of the Dissertation

Electronic properties of organic photovoltaic materials

by

Christopher David Arntsen

Doctor of Philosophy in Chemistry

University of California, Los Angeles, 2014

Professor Daniel Neuhauser, Chair

Organic solar cells have gained much attention as an inexpensive alternative to traditional inorganic cells. While experimental efforts have steadily improved the efficiency of organic devices, a large portion of the improvements have been the result of trial-and-error. Therefore, it would be ideal to be able to use theory to predict which types of materials would produce the most efficient devices. This dissertation presents a series of theoretical studies designed to improve understanding of what makes certain solar cells perform well and to serve as a predictive tool to screen potential new materials.

First, a study of electron transfer in pentacene dimers is presented. The study compares several methods for calculating the electronic transfer integral, including time-dependent density function theory, a time dependent semi-empirical method, and several static calculations. The results demonstrate that at large separations, static calculations can underestimate the strength of coupling.

Next, electronic coupling in fullerenes is calculated. In this section, a method for mimicking bulk chemical environments in film through the use of solvation and application of electric fields is developed. The method is a applied to a number of fullerenes used in organic solar cells, and compared with experimental data on

local and bulk electron mobilities. Comparing the theory and experiment allows one to identify beneficial self-assembly behavior in the fullerenes studied.

This method is then extended to a calculation method we have termed direct delocalization. In this method, a field is applied directly to the Fock matrix in order to delocalize frontier orbitals across a dimer. Once this is accomplished, electronic transfer time is calculated within the standard Marcus theory framework. The results are compared to the more thorough methods described above, and found to be in agreement.

Next, the formulation of a stochastic approach to the GW approximation is presented. In this section, a method for calculating the polarization self-energy with stochastic orbitals is introduced. The method is highly efficient, achieving near linear scaling with respect to system size, compared with the theoretical fourth order scaling. The method is applied to large silicon clusters and several fullerenes to accurately calculate quasiparticle energies.

Finally, in the last two chapters, several methods for studying plasmons are presented. The first presents a method for studying the interaction between molecules and plasmonic materials. The method interfaces a semiempirical quantum mechanical calculation (to study the molecules) with a finite-difference time-domain (FDTD) calculation (to study the plasmonic material). The study shows that plasmon propagation can be heavily influenced by the presence of a molecule. In the last section, an alternative FDTD method is presented. This method, labeled near-field, is a time-dependent version of the quasistatic frequency-dependent Poisson algorithm. This approach is advantageous in that it allows for much large time steps in the propagation, greatly expediting the calculation.

The dissertation of Christopher David Arntsen is approved.

Christopher R. Anderson

Peter M. Felker

Daniel Neuhauser, Committee Chair

University of California, Los Angeles

2014

Table of Contents

List of Figures

List of Tables

Acknowledgments

Chapter 1 is a version of: R. Reslan, K. Lopata, C. Arntsen, N. Govind, and D. Neuhauser, Electron transfer beyond the static picture: A tddft/td-zindo study of a pentacene dimer, *The Journal of Chemical Physics* **137**, (2012). We are thankful to the DOE for support.

Chapter 2 is a version of: J. C. Aguirre, C. Arntsen, S. Hernandez, R. Huber, A. M. Nardes, M. Halim, D. Kilbride, Y. Rubin, S. H. Tolbert, N. Kopidakis, B. J. Schwartz, and D. Neuhauser, Understanding local and macroscopic electron mobilities in the fullerene network of conjugated polymer-based solar cells: Time-resolved microwave conductivity and theory, *Advanced Functional Materials* **24**, 784 (2014). We are thankful to the DOE for support.

Chapter 3 is a version of: C. Arntsen, R. Reslan, S. Hernandez, Y. Gao, and D. Neuhauser, Direct delocalization for calculating electron transfer in fullerenes, *International Journal of Quantum Chemistry* **113**, 1885 (2013). We are thankful to the DOE for support.

Chapter 4 is a version of: D. Neuhauser, Y. Gao, C. Arntsen, C. Karshenas, E. Rabani, and R. Baer, Breaking the theoretical scaling limit for predicting quasiparticle energies: The stochastic *gw* approach, *Phys. Rev. Lett.* **113**, 076402 (2014). We are thankful to the DOE.

Chapter 5 is a version of: C. Arntsen, K. Lopata, M. R. Wall, L. Bartell, and D. Neuhauser, Modeling molecular effects on plasmon transport: Silver nanoparticles with tartrazine, *The Journal of Chemical Physics* **134**, (2011). We are grateful to the NSF for support.

Chapter 6 is a version of: A. Coomar, C. Arntsen, K. A. Lopata, S. Pistinner, and D. Neuhauser, Near-field: A finite-difference time-dependent method for simulation of electrodynamics on small scales, *The Journal of Chemical Physics* **135**,

(2011). We are grateful to the NSF for support.

Vita

2006	Pfizer/CBIA Research Fellowship
2007	NSF Research Experience for Undergradiates Research Fellowship
2008	B.S., Chemistry University of Connecticut Storrs, Connecticut
2008	B.S., Mathematics University of Connecticut Storrs, Connecticut
2013	Hanson-Dow Excellence in Teaching Award University of California, Los Angeles

Publications

C. Arntsen, K. Lopata, M. R. Wall, L. Bartell, and D. Neuhauser, Modeling molecular effects on plasmon transport: Silver nanoparticles with tartrazine, *The Journal of Chemical Physics* **134**, (2011).

A. Coomar, C. Arntsen, K. A. Lopata, S. Pistinner, and D. Neuhauser, Near-field: A finite-difference time-dependent method for simulation of electrodynamics on small scales, *The Journal of Chemical Physics* **135**, (2011).

R. Reslan, K. Lopata, C. Arntsen, N. Govind, and D. Neuhauser, Electron transfer beyond the static picture: A tddft/td-zindo study of a pentacene dimer, *The Journal of Chemical Physics* **137**, (2012).

C. Arntsen, R. Reslan, S. Hernandez, Y. Gao, and D. Neuhauser, Direct delocalization for calculating electron transfer in fullerenes, *International Journal of Quantum Chemistry* **113**, 1885 (2013).

J. C. Aguirre, C. Arntsen, S. Hernandez, R. Huber, A. M. Nardes, M. Halim, D. Kilbride, Y. Rubin, S. H. Tolbert, N. Kopidakis, B. J. Schwartz, and D. Neuhauser, Understanding local and macroscopic electron mobilities in the fullerene network of conjugated polymer-based solar cells: Time-resolved microwave conductivity and theory, *Advanced Functional Materials* **24**, 784 (2014).

D. Neuhauser, Y. Gao, C. Arntsen, C. Karshenas, E. Rabani, and R. Baer, Breaking the theoretical scaling limit for predicting quasiparticle energies: The stochastic *gw* approach, *Phys. Rev. Lett.* **113**, 076402 (2014).

Introduction

Organic photovoltaics

Organic solar cells have gained much attention lately as an inexpensive alternative to traditional inorganic cells. As the maximum efficiency in organic photovoltaic (OPV) devices has increased, they have steadily been getting closer to being economically viable [10]. The maximum efficiency of current state-of-the-art devices is now over 10% [11], though typical high performing devices are in the range of 5-7% [12, 13]. Therefore, much needs to be accomplished in order for OPVs to be truly competitive with inorganic counterparts.

The active, light-harvesting region of an OPV device most typically consists of a polymer donor and a fullerene acceptor blended into a film. Upon irradiation with light, an electron on the polymer is promoted from the highest occupied molecular orbital (HOMO) to the lowest unoccupied molecular orbital (LUMO). The electron is then transferred to the fullerene acceptor, leaving a hole on the polymer. Ideally, the electron and hole are then shunted to the electrodes through an interconnected network of fullerene and polymer, respectively (see schematic in Fig. 0.1).

There are many factors limiting the the power conversion efficiency (PCE) of a solar cell, such as electron and hole mobilities, energy level matching of the donor and acceptor, morphology, and interface with electrodes [5, 14]. There has been extensive effort to improve the maximum PCE, inlcuding thermally annealing fabricated devices, solvent annealing active layers, adding solvent additives, and simply changing the donor and acceptor materials used [12, 15–27]. While the device performance has steadily increased, understanding of specifically what types of materials should produce an efficient solar cell is limited.

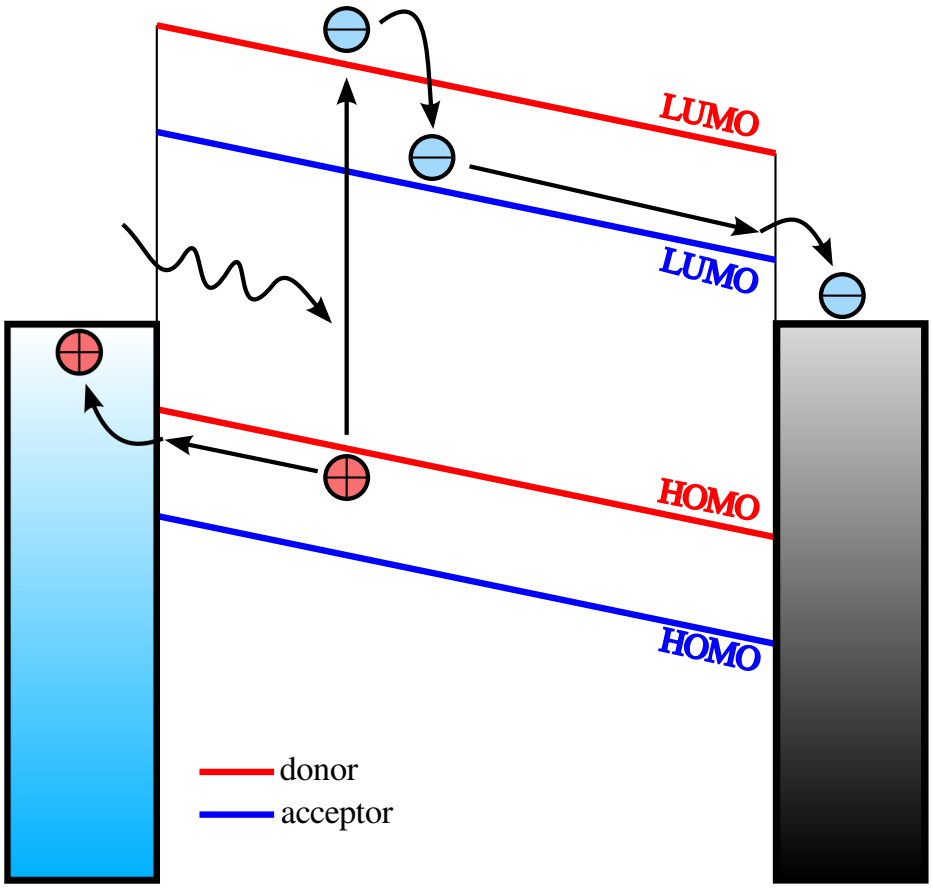

Figure 0.1: Schematic diagram of electron transfer process in OPVs. A photon excites an electron in the donor, which is then transferred to the acceptor. The electron and hole travel to the electrodes via a series of "hops", generating current.

Application of theoretical methods to organic semiconductors

While much of the experimental effort to improve the efficiency of solar cells has been quite successful, more tailored fabrication of devices would be ideal. Theory can therefore be a useful tool to gain understanding of why certain materials yield more efficient devices than others. There are several general theoretical methods commonly used to study various properties of organic photovoltaics, including the drift-diffusion model, density functional theory (DFT), and molecular dynamcs (MD).

Each method offers a useful framework for studying photovoltaics: the drift-diffusion model is capable of reproducing highly accurate current-voltage curves in real devices; DFT is used to study the quantum states of systems (i.e. the orbitals); and MD can be used to study phase separation and morphological properties of materials. This dissertation focuses primarily on the use of DFT to study the properties of materials used in organic photovoltaics. The intent of much the work is to provide an efficient predictive tool which can be used to screen materials prior to their use in actual devices.

One of the most useful theoretical tools used to understand OPV materials is Marcus theory [28]. Marcus theory can be used to calculate the electron transfer rate between states A and B:

$$k_{et} = \frac{2\pi}{\hbar}|H_{AB}|^2 \frac{1}{\sqrt{4\pi\lambda k_b T}} \exp\left(-\frac{(\lambda + \Delta G^o)^2}{4\lambda k_b T}\right)$$

where k_{et} is the electron transfer rate, H_{AB} is the transfer integral, λ is the reorganization energy, and ΔG^o is the free energy difference between states A and B. The most important quantity in the Marcus theory formula is the transfer integral:

$$H_{AB} = \langle \psi_A | H | \psi_B \rangle.$$

The challenge can be accurately describing the wave function associated with states A and B. The Schrödinger equation can be used to generate the appropriate states, where the Hamiltonian is determined using density functional theory (DFT):

$$\left[-\frac{1}{2}\nabla^2 + v(r) + v_H(r) + v_{xc}(r)\right]\psi_i = \epsilon_i \psi_i$$

where the first term is the kinetic energy, $v(r)$ is the external potential, $v_H(r)$

is the Hartree potential, describing the classical electrostatic interactions of the electrons,

$$v_H(r) = \int \frac{n(\boldsymbol{r}')}{|\boldsymbol{r} - \boldsymbol{r}'|} d\boldsymbol{r}',$$

$v_{xc}(r)$ is the exchange-correlation potential, and $n(r)$ is the electron density. Finally, ϕ_i and ϵ_i are the orbitals (eigenvectors of the above Hamiltonion) and orbital energies (eigenvalues), respectively. With the Hamiltonian, orbitals, and energies of the system, one can perform a large number of calculations describing the particular electronic properties of a system (such as Marcus theory rates, as mentioned above). The work described in this dissertation utilizes these tools. For example, the electronic coupling is calculated using the Hamiltonian and wave functions described above.

Synopsis of dissertation

A short summary of the chapters of the dissertation is outlined below. Chapter 1 presents a study of electron transfer in fullerene dimers. The study compares several methods for calculating the electronic transfer integral, including time-dependent density functional theory (TDDFT), a time-dependent semi-empirical method, and static calculations, as well as the use of neutral vs. anionic systems. Compared with time-dependent methods, static calculations underestimate the transfer integral, particularly at large separations. The time-dependent semi-empirical method employed, TD-ZINDO, also underestimates the transfer integral, but a scaling factor can be applied to reproduce TDDFT results. In such a case, TD-ZINDO shows the same fall-off behavior as TDDFT at a fraction of the cost.

Chapter 2 presents a study of static coupling in various fullerene dimers. The main difficulty with these systems is that if environmental effects are ignored,

the orbitals involved in electron transfer can be artificially localized on an individual molecule. Two methods to overcome this difficulty are presented: first, solvating the dimer with point charges in order to mimic the local chemical environment. Second, we apply an electric field to the systems to delocalize the orbitals across the dimer. The electric field method reproduces the solvation method at a fraction of the cost. The calculations are compared to several experimental measurements including device performance, time-resolved microwave conductivity (TRMC), and space-charge-limit current (SCLC). Comparing experiment with theory provides insight into how to why higher efficiency solar cells perform better.

Chapter 3 presents a modified study of static coupling. In the previous chapter, an electric field was used to delocalize the frontier orbitals across the dimer, requiring many self-consistent DFT calculations (one for each electric field strength tested). The method developed in this chapter circumvents the need to perform many DFT calculations by applying a delocalizing bias directly to the Fock matrix. The magnitude of this delocalizing bias is solved self-consistently. The electronic coupling calculated using this method is compared with the aforementioned methods, and is found to be consistent. The method is then applied to numerous fullerene dimers.

Chapter 4 develops a stochastic formulation of the GW approximation (sGW) to many-body perturbation theory (MBPT). GW is used to calculate quasiparticle energies with very high accuracy. However, because GW has a theoretical fourth order scaling, it's application to large systems is not possible. The method presented, through the use of stochastic orbitals, scales near-linearly. To illustrate the performance and accuracy of the method, sGW is applied to hydrogen passivated silicon nanocrystals of over 3000 electrons (or roughly 5 nm in diameter) as well as several fullerene materials. As shown in the chapter, the method yields highly accurate calculations of quasiparticle energies in the fullerenes tested as

compared with experiment.

Chapter 5 presents a method for combing quantum mechanical and classical simulations in order to understand the effect of molecules on plasmon transport between nanoparticles. The simulations describe a system containing three linearly arranged nanoparticles, with a molecule centered between the second and third nanoparticles . x-polarized current is initiated on the first nanoparticle, and x- and y-polarized current is measured on the third. The molecule rotates much of the x-polarized current into the y-direction.

Finally, the development of a finite-difference time-domain method, labeled near-field (NF), is presented in Chapter 6. NF is essentially a time-dependent version of the quasistatic frequency-dependent Poisson algorithm. We assume that the electric field is longitudinal, and hence propagates only a set of time-dependent polarizations and currents. For near-field scales, the time step (dt) is much larger than in the usual Maxwell FDTD approach, as it is not related to the velocity of light; rather, it is determined by the rate of damping and plasma oscillations in the material, so $dt = 2.5$ a.u. was well converged. The method agrees well with Mie-theory in the limit of small spheres. The NF algorithm is especially efficient for systems with small scale dynamics.

CHAPTER 1

Time-dependent electron in pentacene dimers using TDDFT and TDZINDO

1.1 Introduction

Accurately computing electron transfer rates and probabilities is crucial for understanding a wide range of devices and effects, including many types of chemical reactions [29, 30], solar cells [31, 32], nanoelectronics [33], and molecular electronics [34–37]. For example, in fullerene-based organic photovoltaics (OPVs), after photo-excitation of the light harvesting polymer, a charge-separated electron is first transferred to a nearby fullerene molecule, then subsequently shuttled to the electrode via a series of "hops" from one fullerene to another adjacent one. The success of an OPV often hinges on how readily electrons can be shunted from polymer to electrode without recombination with a hole. In general, this is a function of both the device morphology and also the electron transfer probability between two fullerene molecules. Increasing device efficiencies by optimizing transfer between fullerene pairs (e.g., via functionalization) thus offers a tantalizing opportunity. Unfortunately, predictive calculations of transfer probabilities are often elusive as electron transfer in these systems is a complicated process involving coupling between electronic and nuclear motion, in addition to the coupling with environment.

Electron transfer calculations on model systems and simple analogues offer a path forward. There has been much recent progress in modeling electron transfer

between isolated molecules. The electron transfer reaction $A^-B \rightarrow AB^-$ is well established in principle using Marcus theory (for overview see Ref. [28]), where the transfer is computed in the non-adiabatic regime, i.e., weak electronic coupling the donor and acceptor means that inter-conversion from the donor to the acceptor diabatic potential energy surface can be computed semi-classically. Here, two potential surfaces (reactants and products) are required as functions of molecular coordinates, and the transfer probability is computed from three main ingredients: ΔG^0 , the free energy difference between the two states; λ, the energy required to reorganize the system, possibly including a solvent shell, from initial to final state without actually transferring charge; and J, the electronic coupling between the initial and final states. While any number of theoretical approaches can be used within the Marcus framework (e.g., from semi-empirical to correlated methods), density functional theory (DFT) has been the most popular recently, due to good accuracy and modest computational cost [35, 37–41].

For DFT, the main challenge lies in determining proper initial and final states in the transfer integral J in the Marcus formalism

$$J = |\langle \psi_F | H | \psi_I \rangle| \tag{1.1}$$

where $|\psi_I\rangle$ and $|\psi_F\rangle$ are the initial and the final states, and H is the electronic coupling Hamiltonian (for more details, see review by Hsu [42]). Although at first glance this is straightforward, extreme care must be taken in choosing these states to avoid non-physical effects. For example, if one picks $|\psi_I\rangle = A^-B$ and $|\psi_F\rangle = AB^-$ the resulting dynamics could be dominated by electronic relaxation rather than charge transfer.

This issue of correct choice of initial and final states can be bypassed by simply comparing the LUMO and LUMO+1 of the neutral pair, which also gives a rough measure of the coupling. The picture, however, is only qualitative as in reality

the transfer involves the coupling of a negatively charged molecule with a neutral one; this often consists of a significantly perturbed electronic structure from the neutral case.

For predictive calculations, however, the transfer integral J must be computed as accurately as possible, with proper choice of $|\psi_I\rangle$ and $|\psi_F\rangle$. To this end, we recently presented a new approach to electron transfer calculations named time-dependent split (TD-split), where the transfer integral is calculated using the vertical excitation energy of a negatively charged dimer from a fully delocalized ground state [43]; this excitation energy can be computed using virtually any time-dependent method. A related method is generalized Mulliken-Hush (GMH), which computes the coupling using the vertical excitation energy and transition dipole moment between two charge-localized states [44]. In TD-split the nuclear degrees of freedom are frozen, the reaction coordinate is the degree of charge localization, and the resulting transfer integrals are associated with the rate of electron transfer for particular system geometry. This is contrast to traditional Marcus-type calculations, which includes the effect of the vibrational degree of freedom.

Marcus theory gives essentially the exact result (in the non-adiabatic limit) when the electronic transfer integrals are known. For large-scale systems, where the transfer integrals are almost always calculated by DFT, Hartree-Fock (HF), or semi-empirical methods, most of the electronic degrees of freedom are frozen in the calculation. Put differently, the possibly crucial effect of the other electrons on the transfer is neglected in such single-particle static calculations, and TD-split corrects this omission. Therefore, in the non-adiabatic limit the result of TD-split can be viewed as the transfer integral in Marcus theory; when the distortion is weak and the vibrational degrees of freedom do not contribute, TD-split directly yields the transfer rate.

As a first step towards modeling charge transfer in OPVs, in this paper we use

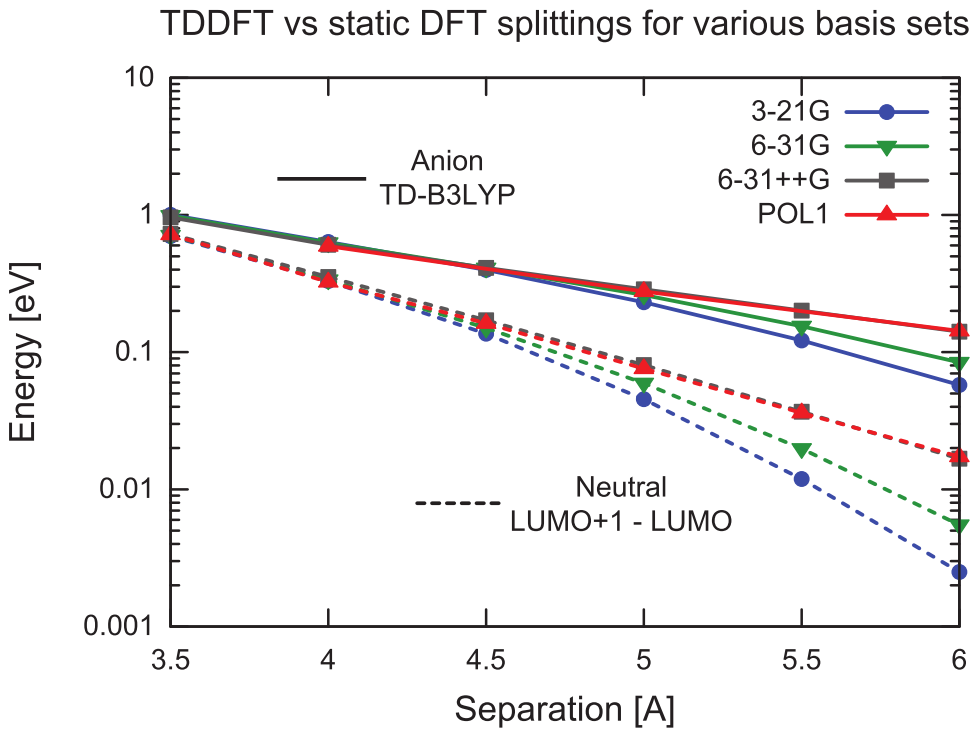

Figure 1.1: Static B3LYP splitting (dashed) and TD-B3LYP energies (solid) for a range of basis sets. Larger separations require a basis set with diffuse functions (e.g., 6-31++G and POL1) to avoid non-phyical super-exponential falloff.

TD-split in conjunction with time-dependent density functional theory (TDDFT) and time-dependent ZINDO [43, 45] to study electron transfer across a pentacene dimer consisting of two planar stacked pentacene molecules with an intermolecular separation ranging from 3.5 Å to 6.0 Å (see Fig. 1.2). The rest of the chapter is structured as follows: In Section 1.2 we briefly review the approach and discuss computational details, in Section 1.3 we present calculations on a pentacene dimer model system, and in Section 1.4 we summarize the results and offer some outlooks on future directions.

1.2 Methodology

1.2.1 Static splittling

In this section, we briefly discuss both the TD-split (dynamic) and static approaches to computing the Marcus coupling term J. In the static picture, one assumes that the charge distribution for the neutral combination is not perturbed (dynamically or statically) by adding an extra electron. If that assumption is correct, the difference in energy between the LUMO+1 and LUMO for the neutral pair AB is equivalent to the Marcus factor for identical dimers with delocalized orbitals. Transition requires that the LUMO and LUMO+1 are delocalized over both fragments, otherwise the splitting will be high but there will be no transition; this effect is easily included with an additional weight term which measures the delocalization of the LUMO and LUMO+1.

1.2.2 Dynamic splitting

In the dynamic picture (TD-split), rather than use the LUMO+1-LUMO of the neutral system to compute the splitting (and thus the charge transfer rate), we instead use the vertical excitation energy (VEE) of the -1 charged dimer from a delocalized ground state, where the extra electron is equally shared between the two fragments. In a Marcus-like picture, this delocalized ground state is akin to an electronic transition state for the transferred electron; i.e., the intermediate situation between the charge on one fragment and the charge on the other, and the VEE is thus the electronic coupling between the two diabatic surfaces. Since the nuclear geometries are fixed, this does not correspond to the Marcus intermediate state, but rather to the halfway point in the electron transfer for the given geometry. By using the VEE of the -1 charged dimer from its delocalized ground state, you have carefully chosen the initial and final states in the transfer integral J to exclude non-physical re-arrangement of the electrons due to local-

ization on one fragment or the other. In contrast, if you instead compute the transfer starting from a system with the extra electron localized on one fragment you will have added an indeterminate amount of energy; the calculation will thus give non-physical results since the localized charge perturbs the electronic density on the other fragment, and the resulting dynamics from this initial state will be dominated by electronic relaxation rather than transfer. An alternate approach is to use an isolating potential to create initial states with well-defined energies [46]. When the vibrational degrees of freedom are weakly coupled, TD-split corresponds directly to the transfer rate. Note that when the system is not completely symmetric, the rate of transfer can still be obtained using the TD-split approach from a flux-flux time-dependent calculation which starts with the system in its ground anionic state (delocalized to a certain extent, depending on the degree of asymmetry) and then propagates the fluxes [43]. The flux-flux result is the equivalent of the $|H_{AB}|^2$ term in Marcus theory.

Schematically, the TD-split approach can be expressed as

$$\delta A \equiv \langle \Psi(t)|A|\Psi(t)\rangle \tag{1.2}$$

where $|\Psi(t)\rangle$ is a perturbed ground state for the entire charged system (including donor, acceptor, and the extra delocalized electron), and A is the perturbation operator. The time-dependent dynamics are thus directly associated with transport since the added charge is delocalized. In this method, the initial state is the ground static density matrix for the entire (donor and acceptor) charged system. A time-dependent excitation is applied and the response to this excitation is a measure of electron transfer rate. As formulated, this method is linear-response in nature. This type of calculation is dynamic in the sense that it goes beyond simply using the static eigenvalues of the single-particle Hamiltonian and instead accounts for electronic structure changes during the excitation. For example, in TDDFT this corresponds to correcting the static Kohn-Sham DFT eigenvalue dif-

ferences with the electron-hole response. As will be shown later, these effects are crucial for properly capturing the separation dependence of the charge transfer.

1.2.3 Compuational details

Both the static and dynamic approaches are flexible, as the orbital energies (LUMO, LUMO+1) and the vertical excitation energies can be computed via any number of static and time-dependent approaches, such as coupled cluster (e.g., equation of motion coupled cluster [47,48]), linear-response [49] or real-time TDDFT [50–54], or time-dependent semi-empirical methods [45, 55]. In this paper, we use DFT and ZINDO to compute the static splitting and VEEs of a -1 charged pentacene dimer. All DFT/TDDFT calculations were performed with atom-centered Gaussian basis sets using a development version of the NWChem software package [56]. Since these methods are commonplace, we omit the details.

The ZINDO and TD-ZINDO results were obtained by using a modified version of ZINDO-MN package [57]. In a nutshell, in ZINDO only the valence electrons are treated, which is done via semi-empirical one-body (i.e., nuclear and core) parameters h_{ij} and two-body interaction parameters v_{ijkl}, which are fit to experimental data,

$$F_{ij} = h_{ij} + \sum_{kl} v_{ijkl} P_{ij}, \tag{1.3}$$

where P is the density matrix in the atomic orbital basis. The time-dependent response is computed using explicit time propagation via the von Neumann equation,

$$i\frac{\partial P}{\partial t} = [F'(P'(t)), P'(t)], \tag{1.4}$$

where the prime denotes quantities in the molecular (orthogonal) basis. The actual

propagation was carried out using a linear response von Neumann operator

$$LZ \equiv \frac{dZ}{dt} = -i\frac{[F'(P_0' + \eta Z), P_0' + \eta Z] - [F'(P_0'), P_0']}{\eta} \tag{1.5}$$

where $Z(t) \equiv P(t) - P_0$ is the deviation of the MO density matrix from the initial state, and η is a small parameter ensuring linearity. $Z(t)$ is propagated from a dipole perturbed ground state $Z_0 = -i[D, P_0']$ via a Chebyshev expansion, and the Fourier transform of the resulting time-dependent dipole moment yields the absorption spectrum, and thus the vertical excitation energies. For all TD-ZINDO simulations, the time step was 0.4 a. u. (0.01 fs) and the ZINDO parameters were taken from the original ZINDO-MN package. For a more complete discussion of the TD-ZINDO approach see Ref. [45].

1.3 Results

1.3.1 Convergence with basis set

The large separations in these systems can pose a serious problem for atom-centered basis sets, so as a first step we confirmed that the TDDFT and static splitting (LUMO+1-LUMO for the neutral dimer) results were all converged with basis.

Fig. 1.1 shows the B3LYP TDDFT VEE for the negatively charged dimer, and the difference in energy between the LUMO and LUMO+1 for the neutral dimer for the 3-21G, 6-31G, 6-31++G, and POL1 basis sets. For shorter separations (R $<$ 4.5 Å), both the static and TDDFT energies are relatively insensitive to basis set, whereas there is a pronounced deviation from exponential behavior at larger separations for the 3-21G and 6-31G basis sets. The super-exponential falloff (nonlinear in log plot) is a non-physical consequence of the insufficient physical extent of the smaller basis sets. The POL1 basis, which is highly diffuse and

optimized for response properties, retains the correct exponential falloff, as does the 6-31++G basis, which is a 6-31G basis with extra diffuse functions. The TDDFT VEEs are less sensitive to basis set than the static DFT LUMO+1-LUMO energies, since individual orbital energies are typically more sensitive to incomplete overlap due to finite basis. Given these results, we henceforth use the 6-31++G basis, which for our purposes yields effectively the same quality results as POL1 with significantly less computational effort (656 basis functions instead of 1308). In general, for calculations of this kind on extended systems, augmenting a small basis with a few diffuse functions offers an affordable way to capture charge transfer processes.

1.3.2 Static versus dyanamic splittings

For the -1 charged system, the HOMO and LUMO are extended across the dimer, and the excitation corresponds to a symmetric → antisymmetric flip for the dimer wavefunction (see Fig. 1.2). This is important because transitions between orbitals localized on individual fragments would result in an apparently large splitting, but with no electron transfer. This situation can be remedied somewhat by applying a delocalizing potential to the system to force a delocalized initial state but this was unnecessary for this symmetric system. The shapes of the neutral LUMO and LUMO+1 are qualitatively similar to the HOMO and LUMO of the negatively charged dimer (not shown), and since they are likewise extended, the difference in their energy is a fair measure of the static splitting.

Fig. 1.3 shows the -1 charged dimer vertical excitation energies using a range of TDDFT exchange-correlation functionals: local-density approximation (LDA) (slater exchange [58] and Vosko-Wilk-Nusair (VWN) correlation [59]), Perdew-Burke-Ernzerhof (PBE) functional [60], B3LYP [61]. The corresponding DFT neutral dimer LUMO+1-LUMO energies are shown for comparison. Overall, all TDDFT VEEs are quite insensitive to exchange-correlation functional; B3LYP

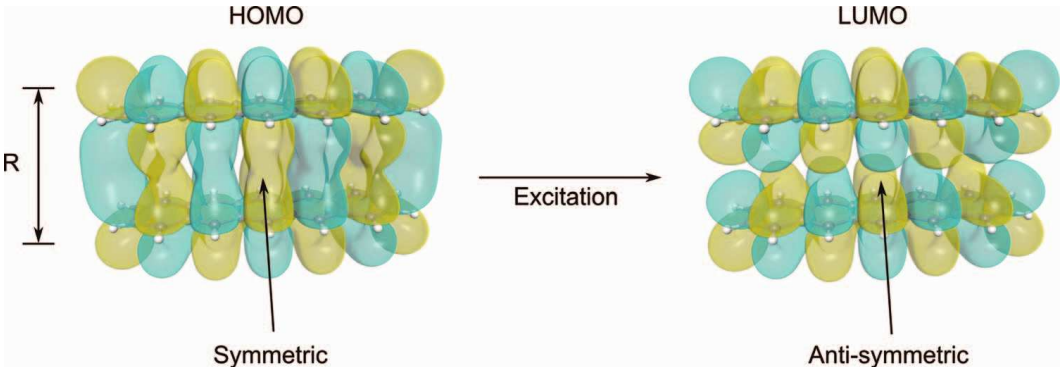

Figure 1.2: Snapshots of the orbitals involved in the vertical excitation of the -1 charged dimer (5 Åseparation, PBE, 6-31++G basis). The excitation corresponds to a symmetric → aysmmetric flip of the wavefunction.

is slightly red-shifted from LDA and PBE, but all have roughly the falloff rate (exponential decay constant 0.73 $Å^{-1}$). For separations less than 4.5 Å, there are intra-fragment excitations which are lower in energy than the HOMO → LUMO excitation. These excitations are independent of separation, however, and with increasing R the HOMO → LUMO transition is guaranteed to become the lowest excitation, since it decays exponentially with separation. The DFT neutral static splittings between the first two virtual states (LUMO+1 vs. LUMO) are likewise insensitive to the functional, but are both significantly shifted lower in energy than the TDDFT VEEs, and also decay much faster (1.5 $Å^{-1}$). Fig. 1.3 also shows the corresponding static and time-dependent ZINDO results. Since we are interested in the slope rather than absolute energies, they were scaled by 1.5 to facilitate comparison with the DFT results. The ZINDO results are qualitatively similar to DFT, except for steeper exponential falloffs. Better tuning of the ZINDO coupling parameter might lead to better agreement with DFT.

Overall, these results suggest that the neutral static picture drastically underestimates the charge transfer rate, and the underestimation grows rapidly with increased separation. For example, whereas the static PBE energy is only 34 %

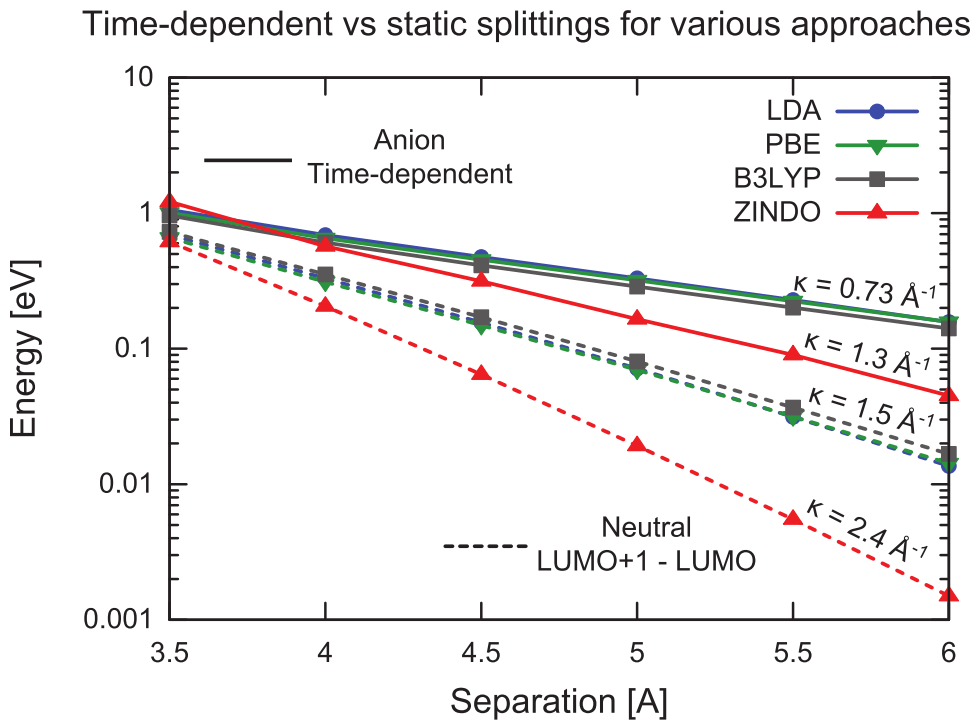

Figure 1.3: Static DFT/ZINDO splitting for the neutral dimer (dashed) and HOMO → LUMO TDDFT/TD-ZINDO vertical excitation energies for the -1 charged dimer (solid); the corresponding exponential decay constants are shown above each curve. All DFT calculations use the 6-31++G basis set. The ZINDO results are scale by 1.5 for easier comparison.

lower than the TD-PBE VEE at 3.5 Å, it is a full order of magnitude smaller at 6 Å. The reason for this is twofold: First, the static picture of orbital energy differences does not include re-arrangement of the electronic density during charge transfer; this is analogous to static DFT orbital energy differences versus TDDFT for traditional excitations. Second, the static picture assumes negligible perturbation of the electronic structure of the fragments upon adding an additional electron. Although the qualitative features of the orbitals (e.g., shape and ordering) are qualitatively unchanged by the additional electron, the orbital energetics are affected. For shorter separations, this effect is lessened since the dimer

is more like a super-molecule. In a similar vein, the electronic structure of larger systems (e.g., fullerenes) is likewise less sensitive to extra electron.

As a final check, we compared the neutral LUMO+1-LUMO splitting to the -1 charged HOMO-LUMO, as shown in Fig. 1.4. For pure DFT functionals (LDA, PBE), the two are virtually identical, which is consistent with the idea that the electronic structure of the dimer is negligibly affected by the addition of an extra electron. The anion splitting for the hybrid functional (B3LYP), however, is significantly overestimated, and falls off in an incorrect subexponential manner. For pure HF (not shown), this is even more pronounced. In a nutshell, HF is driving the system into an ionic-like state rather than a delocalized one, resulting in unphysical orbital energies; this failure of HF to describe anions is well-known. It is not surprising that B3LYP shows this behavior because it contains 20% HF. ZINDO, which is a HF-type method (albeit with modified interaction terms), also suffers from this problem.

There are two things to note from these results: First, they confirm that dynamic (time-dependent) effects (e.g., electronic relaxation) are indeed important, and these calculations are not merely a measure of the anion static HOMO-LUMO splitting. Second, even though HF-based methods break down when describing the anionic orbital energies, the corresponding dynamics are still quite reasonable, i.e., the TD-B3LYP excitation energies are in excellent agreement with TD-LDA and TD-PBE, and TD-ZINDO is in reasonable agreement. Put another way, the response of the system is relatively insensitive to the poor ground state description.

1.4 Conclusion

In summary, we computed the electronic couplings for a -1 charged pentacene dimer as a first step towards modeling electron transfer in organic photovoltaics.

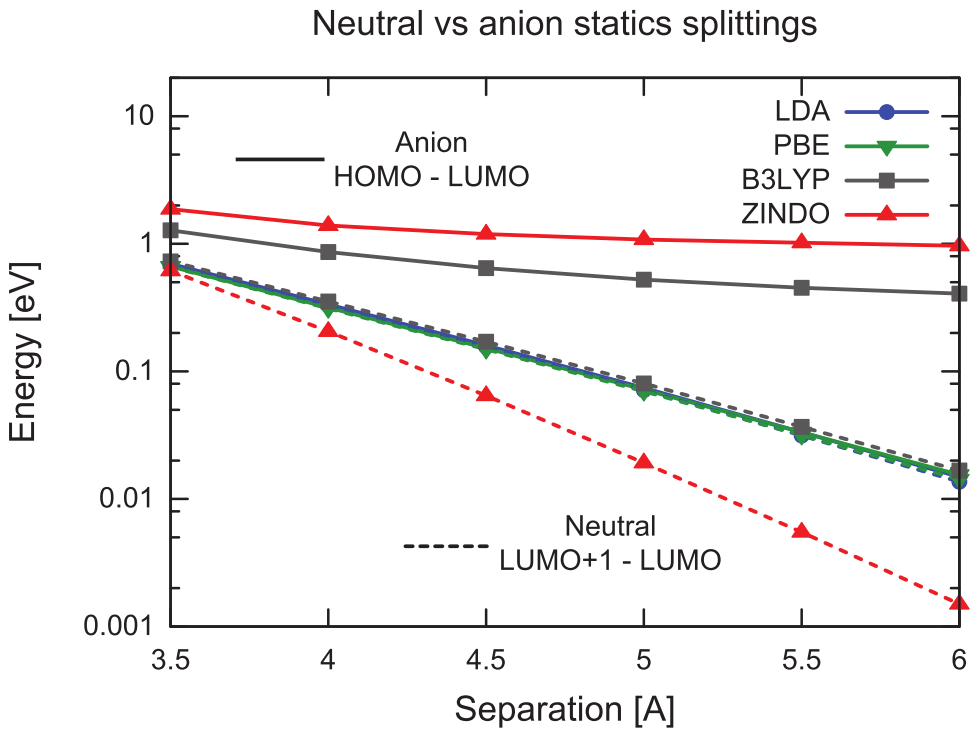

Figure 1.4: Static splitting for the neutral and -1 charged dimer. The two agree well for pure DFT, but the anion is poorly described by B3LYP and ZINDO due to the failure of HF to capture the delocalized ground state.

Two types of splitting were computed: the static DFT and ZINDO LUMO+1-LUMO of the neutral dimer, and the vertical excitation energy of the -1 charged dimer from a delocalized ground state, which was obtained via time-dependent methods (TDDFT and TD-ZINDO). The static picture consistently underestimates the splitting, and results in a far steeper exponential falloff than the dynamic splitting. As a consequence, while the static splitting offers a decent approximation to the transfer at short distances, with increasing separation it becomes ever more important to use the dynamic approach. These results have strong implications in systems like organic photovoltaics, where the LUMO+1-LUMO is a common rule of thumb for estimating charge transfer efficiency, since the addition of an extra electron on a fullerene is usually assumed to not significantly

perturb the electronic structure. Care must be taken, however, as using the static approximation for large separations will drastically underestimate transfer probabilities, perhaps even by orders of magnitude in extreme cases. Future studies will address the accuracy of the static versus dynamic picture for charge transfer across fullerene pairs.

CHAPTER 2

Static coupling in fullerene derivatives: Understaing local and macroscopic electron mobilities in organic solar cells

2.1 Introduction

One of the primary factors limiting OPV performance is device morphology. While there are a number of organic electron donors and acceptors with optimally matched energy level, they can produce poorly performing solar cell devices. Most typically, poor performance from seemingly ideal materials is caused by an improper degree of phase separation when blended together [62, 63]. Because of this, there has been a great of effort using processing conditions to control BHJ morphology, including the use of solvent additives [12, 15, 16], post fabrication thermal annealing [17–19], and sequential deposition of the donor and acceptor layers [20–27]. All of these techniques greatly increase the parameter space for optimizing power conversion efficiency, which is detrimental when most of the progress in increasing PCE for a given set of materials is made via exploring this parameter space through trial-and-error.

Another possible method for fabricating OPV devices with a robust morphology would be to utilize self-assembly. Our experimental collaborators have been using fullerene molecules which stack in a columnar fashion (see Fig. 2.2(b) for example) [64, 65]. The propensity to stack is a result of the five 'feathers' coming

off the fullerene ball (due to their appearence, they have been dubbed 'shuttlecocks'. Refs. [64, 65] show that certain shuttlecocks produce functional OPV devices, whereas other produce devices with exceptionally poor performance, despite being nearly electronically identical. The motivation behind the work in this chapter is then to better understand the connection between morphology and performance by comparing electronic coupling calculations with experimental measurements of local and bulk mobilities. In this chapter, we develop a method for efficiently calculating electronic coupling in asymmetric dimers, apply to several molecules, and conclude from the data that shuttlecocks having a propensity to stack produce superior devices to those that do not stack.

2.2 Methodology

2.2.1 Introduction

As mention in Chapter 1 the problem we consider is transfer of electrons between two fragments, labeled left and right:

$$L^- + R \rightarrow L + R^-$$

where we are most interested in the eletronic coupling, which formally has the form,

$$\gamma(L \rightarrow R) = |\langle \Psi_L | H | \Psi_R \rangle| \tag{2.1}$$

where we introduced the total Hamiltonian and the left- and right-localized wavefunctions for the transferred electron. In Marcus theory, the transfer rate for the electron between the left and right wells is

$$k(L \to R) = \frac{\gamma(L \to R)^2}{\hbar}\sqrt{\frac{\pi}{\lambda k_B T}}\exp\left(-\frac{(\Delta E + \lambda)^2}{4\lambda k_B T}\right) \tag{2.2}$$

where ΔE is the energy difference between the initial and final states, and λ is the reorganization energy associated with the transfer.

There is a complication in the application of this formalism. The two fragments that the electron hops between are, in practice, surrounded by other molecules. Thus, for example, Fig. 2.2 shows two TBP molecules that the electron can hop between. The fullerene caps do not have same environment in the isolated-dimer; one cap is surrounded by feathers from the other fullerene, while the second fullerene cap is exposed. This difference in environment will cause an energy mismatch for an electron in one fragment versus the other, thus causing a bias; however, this bias in unphysical and is an artifact of considering only two fragments. In the actual experimental system, at least within the bulk, each fragment is surrounded by other molecules, making the environment for the electron identical in each fragment. This modified-environment problem will occur for any dimer which is not centro-symmetric, (PCBM, a centro-symmetric molecule, will retain the symmetry between the two fragments even without an environment).

A solution to this problem is outlined in Section 2.2.2. Basically, we show that by introducing an artificial bias (an artificial electric field) we can bring the levels to equilibrate and demonstrate that this artificial field captures quantitatively the same effects as a more sophisticated description with Mulliken charges simulating the other molecules. We label this artificial bias a delocalizing potential. Further, we show that the delocalizing potential does not have to be known accurately, and quite a large range can be used; i.e., the delocalizing potential just has to ensure that the lowest two considered states of the full Hamiltonian (LUMO and LUMO+1) are not localized on the same fragment.

In Chapter 1 on a model system (pentacene dimer) we have shown that the best

way to study such transferred-electron is therefore by using a TDDFT excitation of the ground anionic LR^- system, an approach labeled TD-Split; however, we have also shown that acceptable results follow with a static-DFT treatment of the open shell anionic system, LR^-, and studying the coupling between the HOMO and LUMO levels of this system, labeled static-anionic description, as well as a static-DFT treatment of the neutral system. For large separations, the basis set should include some diffuse functionals and preferably local density functionals rather than Hartree-Fock-exchange based ones, due to the tendency of the latter to localize an electron. We therefore applied both static and neutral approaches. The results presented are for static neutral systems using the B3LYP functional. We found these results were in close agreement to anionic systems. For example, for PCBM, we found that using neutral B3LYP calculations gave a coupling of 1.01×10^{-2} eV, neutral PBE a coupling of 8.72×10^{-3} eV, and anionic PBE 7.16×10^{-3} eV (we disregard anionic B3LYP as this functional is known not to give accurate results for charged systems).

2.2.2 Direct coupling

Given two fragments, in a static study there are two approaches for extracting the splitting. In both, we first define a scaled Fock matrix,

$$\overline{F} \equiv S^{-\frac{1}{2}} F S^{-\frac{1}{2}} \tag{2.3}$$

where we introduce the Fock matrix and the overlap matrix. We then diagonalize the scaled Fock matrix, F:

$$\overline{F} = V \epsilon V^T \tag{2.4}$$

The Fock and overlap matrices are derived from density functional theory (DFT) using STO-3G basis set from NWChem software package, which has been

shown to give good accuracy within the Marcus theory framework. The two levels associated with the transfer are labeled as $I, I+1$, where I is the LUMO for the static-neutral system and the HOMO for the static anionic.

To delocalize the LUMO and LUMO+1 orbitals across the dimer, we apply an artificial bias through the placement of point charges far away, $\pm q$ at $\pm A$ where $A = 200$ Å, and vary q. At each electric field we also calculate the expectation value of the localization of the I and the $I+1$ levels, i.e., $\theta(I, I)$ and $\theta(I+1, I+1)$, where the molecular-orbital localization matrix is:

$$\overline{\theta} = V^T S^{-\frac{1}{2}} \theta S^{-\frac{1}{2}} V \tag{2.5}$$

and θ is the step-function matrix associated with being on the right fragment, i. e.

$$\theta_{ij} = S_{ij} f(i) f(j) \tag{2.6}$$

and,

$$f(i) = \begin{cases} 1 & i \text{ on right fragment} \\ 0 & \text{otherwise} \end{cases} \tag{2.7}$$

As we sweep through the electric field, the physical location of the $I, I+1$ levels switch; at the minimum coupling point, the two levels are delocalized over the two fragments, so $\overline{\theta}(I, I) \approx \overline{\theta}(I+1, I+1) \approx 0.5$.

The difficulty with the using diagonal values of the localization matrix is that the field needs to be precisely determined, especially when the minimum coupling is very small. While this is not terribly problematic since for each iteration it is easy to determine if the field is too large or small by the expectation value of $\overline{\theta}(I, I)$, the method still requires many DFT calculations.

We therefore use a method in which we still have an artificial electric field, but its only purpose is to ensure that the I and $I+1$ levels are not on the same fragment. For example, in an isolated TBP dimer if there is no electric field then both the LUMO and LUMO+1 (and even the LUMO+2) are located on the same

fragment. To prevent this, we apply an electric field. We determine numerically if the electric field is appropriate by considering the 2×2 localization matrix in the $I, I+1$ space, defined as

$$\tilde{\theta} = \begin{pmatrix} \overline{\theta}(I,I) & \overline{\theta}(I,I+1) \\ \overline{\theta}(I+1,I) & \overline{\theta}(I+1,I+1) \end{pmatrix} \tag{2.8}$$

We then diagonalize the $\tilde{\theta}$ matrix, obtaining a diabatic basis which is a combination of the I, $I+1$ elements:

$$\tilde{\theta} = M^T \eta M \tag{2.9}$$

The Fock matrix in the diabatic basis is then defined as:

$$F^D \equiv M^T \begin{pmatrix} \epsilon_I & 0 \\ 0 & \epsilon_{I+1} \end{pmatrix} M = \begin{pmatrix} \epsilon_{left} & \gamma \\ \gamma & \epsilon_{right} \end{pmatrix} \tag{2.10}$$

and the electronic coupling we desire is given directly by $\gamma(L \to R) = |F^D(1,2)|$. The two methods for calculating the coupling give identical results, but the use of the diabatic basis allows a much more lenient range of electric fields: the eigenvalues of the adiabatic eigenstates η_1, η_2 need only be sufficiently close to 0 and 1, whereas when the coupling is calculated as the half-splitting between the LUMO and LUMO+1, the diagonal elements of $\overline{\theta}$ need to be precisely 0.5 (see Fig. 2.1).

2.3 Results

To tie in with the work done by our experimental collaborators on shuttlecocks, we started by examining the coupling between two shuttlecock molecules, 6,9,12,15,18-pentakis(4-tert-butylphenyl)-1-hydro[60]fullerene (TBP) and 6,9,12,15,18-pentakis(4-methylphenyl)-1-hydro[60]fullerene (TOL). We chose these two SC fullerenes because they present a sharp contrast in their ability to self-assemble. Previously,

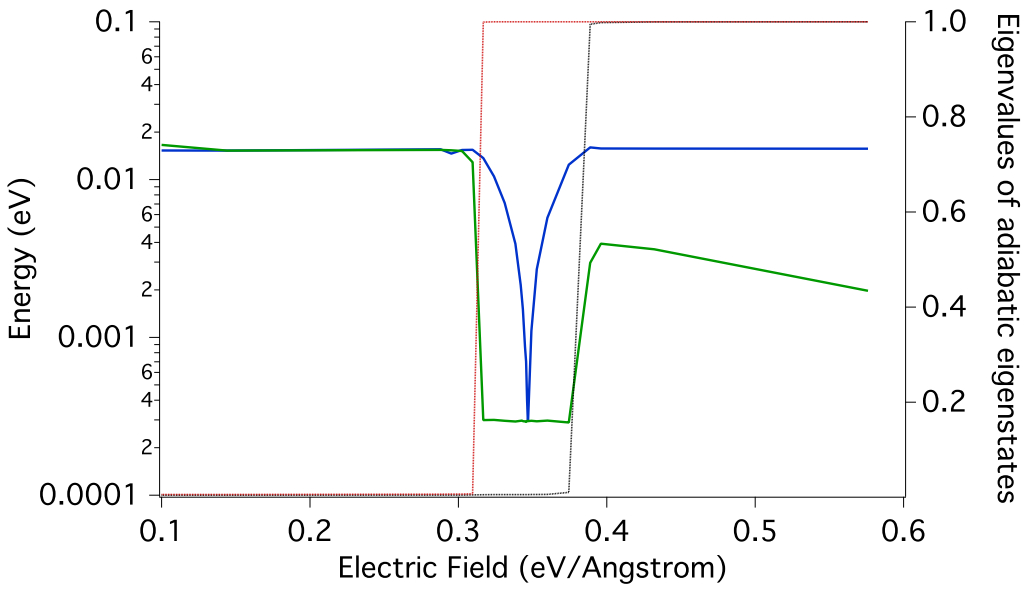

Figure 2.1: Two methods for calculating the 4-*t*Bu coupling as a function of electron field: half-splitting of the LUMO and LUMO+1 orbitals (blue line), and coupling as calculated from Eq. (2.10). Note coupling is accurately calculated for the range of electron field over which the eigenvalues of the adiabatic eigenstates are close to 0 and 1 (balck and red dashed lines).

it was found that TBP was a 'universal stacker', assembling into one-dimensional stacks when crystallized from essentially every solvent explored [64],which in turn lead to the best solar cell performance of all the SC fullerenes examined [64]. In contrast, the TOL molecule, which is electronically identical to TPB (TOL differs structurally from TBP only in the size of the alkyl group on the end of the five SC feathers), appeared to show little propensity for columnar self-assembly, which resulted in exceptionally poor device performance [64,65]. Finally, to understand how local mobility among the fullerenes influences overall device performance, we also elected to examine coupling between molecules of the well-studied PCBM. The chemical structures of the TPB, TOL and PCBM fullerene derivatives, as well as the geometries we used for calculating the electronic coupling between pairs of

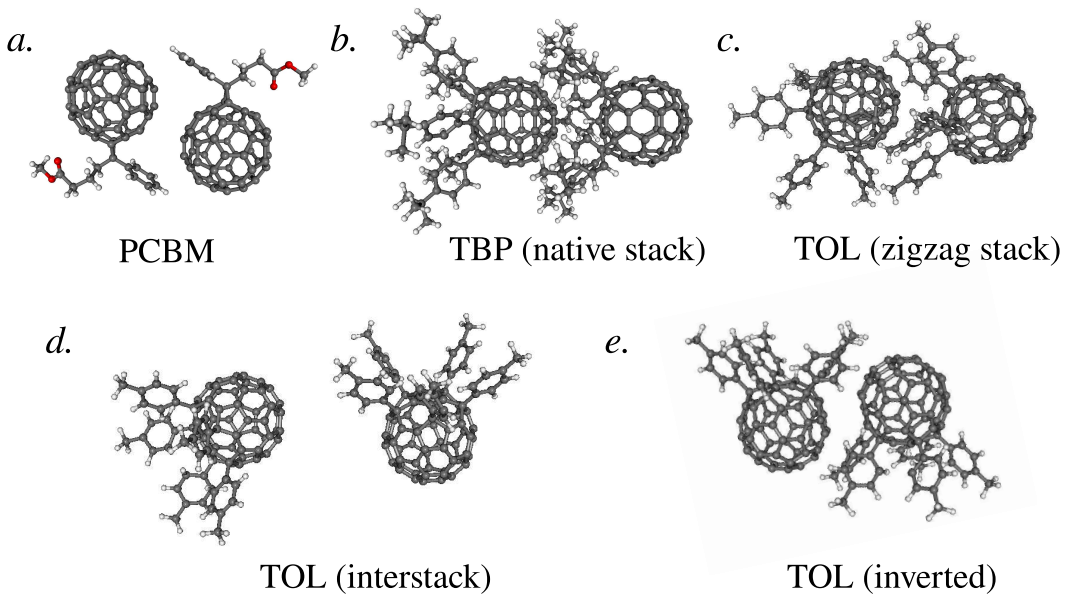

Figure 2.2: Chemical structures of the fullerene derivatives considered in this chapter and the geometries of the fullerene pairs used in our DFT calculations. (a) PCBM; (b) the 4-*t*Bu shuttlecock molecule in its stacked orientation; (c) the 4-Me shuttlecock in its native crystal structurel note the 4-Me molecules crystallize in a 'zigzag' stack motif rather than the linear 'ball-in-cap' exhibited by 4-*t*Bu; (d) the 4-Me molecule in its interstack geometry over which we varied the separation distance of the individual molecule; (e) 4-Me molecules in a head-to-tail ('inverted stack') geometry similar to that of the PCBM molecules.

these molecules, are shown in Fig. 2.2.

Although we do not know the distribution of geometries of pairs of fullerene molecules in a working BHJ device, it seems reasonable that on molecular length scales, the spatial relationship between adjacent fullerene molecules should be similar to that in single crystals. Thus, we chose geometries for our calculations for the TOL and TBP derivatives from the crystal structures found in previous work [65]. For the electronic coupling in TBP dimers, we considered only the linearly stacked orientation found in the crystals derived from most different

organic solvents (Fig. 2.2(b)). For pairs of TOL molecules, we calculated the electronic coupling in a 'zigzag stack' geometry taken from crystals formed in toluene (Fig. 2.2(c)) and an 'inverted' geometry taken from crystals formed in methanol (Fig. 2.2(e)). For completeness, we also calculated the coupling between TOL dimers at their 'interstack' geometry (Fig. 2.2(d)). In the native crystal, the interstack TOL orientation contains interstitial solvent molecules, which prevent the TOL molecules from residing close together. Since there likely is not any solvent present between fullerene molecules in a BHJ device, to calculate the electron transfer probability between TOL molecules in this orientation, we eliminated the solvent from the crystal structure and repeated the calculation over intermolecular distances ranging from 11.2 Å to 15.2 Å center-to-center fullerene separation (the lower end of this range is limited by van der Waals contact between the TOL molecules, while the upper end is what is found in the native crystal with interstitial solvent molecules). Finally, for the electronic coupling between PCBM molecules (Fig. 2.2(a)), we took the geometry from the PCBM crystal structure in Ref. [66].

Using these geometries and our DFT-based method outline above, we calcu-

Molecule	Center-to-center distance [Å]	Coupling (eV)
TBP (native stack)	10.8	2.95×10^{-4}
TOL (zigzag stack)	10.9	2.64×10^{-4}
TOL (interstack)	11.2-15.2	$1.75 \times 10^{-7} - 4.15 \times 10^{-4}$
TOL (inverted)	9.9	1.45×10^{-3}
PCBM	10.2	1.00×10^{-2}

Table 2.1: Calculated electron couplings for fullerene molecular dimers with the geometries in Fig. 2.2.

lated the electronic coupling between multiple pairs of fullerene molecules and obtained the results summarized in Table 2.1. For the SC fullerene derivatives, we find that both the TOL and TBP molecular pairs have essentially the same electronic coupling (within 10%) when placed in their respective 'stacking' orientations; this result makes sense given that TOL and TBP have an identical electronic structure, so the overlap of their LUMOs is about the same when adjacent molecules are forced to have similar geometries. When the SC molecules are not in the desired stacked geometry, the electronic coupling varied strongly (roughly exponentially) with the average distance between the fullerene balls. At the closest possible non-stacked distance (limited by steric hindrance of the alkyl substituents), the coupling is actually slightly higher than that in the stacked geometry. Thus, even though we do not know the precise geometry between neighboring SC fullerene molecules in BHJ devices, we can conclude that as long as these molecules stay in close van der Waals contact, the electronic coupling of the pentaarylfullerenes is comparable in any geometry, lying in the range of 10^{-4} to low 10^{-3} eV.

The fact that the molecular length-scale coupling between pentaaryl fullerenes is similar in nearly every geometry has important implications for solar cells built from these materials. If the local coupling of these molecules is the same, and the molecules have identical electronic structure (i.e., identical HOMO and LUMO levels with similar orbitals), then any difference in device performance must be the result of differences in the macroscopic geometry of the fullerene network. This makes sense given that TBP shuttlecocks self-assemble into long stacks, creating a much better macroscopic fullerene network throughout the active layer than TOL molecules, which phase-segregated from the polymer into unconnected islands [64]. Thus, self-assembly can indeed improve the macroscopic network of polymer-fullerene BHJ solar cells, as we demonstrated experimentally in previous work [67].

To further illustrate the dependence of OPV device performance on morphology, we compare the theoretical results mentioned above to two experimental methods: time-resolved microwave conductivity (TRMC) and space-charge-limit current (SCLC). TRMC is a method in which one measures the time dependent absorption absorption of microwave power. The power absorbed is related to the photoconductance of the sample, from which one can determine the *local* electron mobiltiy. The electron mobility from these experiments was found to be 0.44 $\times 10^{-2}$ cm^2/Vs for TOL and 0.49 $\times 10^{-2}$ cm^2/Vs for TBP [5]. The similarity in these values is not surprising given that these molecules are electronically nearly identical.

SCLC, on the other hand, involves measuring current-voltage behavior of diodes of the materials of interest. One is then able to fit this data to give an estimate of the *bulk* mobility of the material. The SCLC mobilites were measured to be 0.68 $\times 10^{-6}$ cm^2/Vs for TOL and 0.68 $\times 10^{-6}$ cm^2/Vs for TBP [5]. This is a substantial difference, particularly in comparison to the local mobilities.

Thus, using the results of the DFT calculations and TRMC measurements, one finds the two are in agreement that TBP and TOL have similar local mobilities. However, comparing device performanace and SCLC, one finds vastly different bulk mobilities. Given the higher propensity of TBP to stack, one can therefore draw the conclusion that it is in fact this morphological difference between the two fullerenes that causes one to perform better than the other. This is an important idea, as emphasizes the importance of morphology.

Also shown in Table 2.1 are the results of the electronic coupling calculation for a pair of PCBM molecules. We find that the electronic coupling between neighboring PCBM molecules is roughly two orders of magnitude larger than the average coupling between the SC fullerenes. This explains why devices built from the SC fullerenes perform so much more poorly than devices built with PCBM, even though the assembled macroscopic TBP fullerene network is likely better

than the random PCBM network: electrons are simply orders of magnitude more easily able to move between PCBM molecules than between SC molecules.

Why is the electronic coupling so much higher between PCBM molecules than other fullerenes? For PCBM, the LUMO and LUMO+1 orbitals are highly delocalized around the molecules in a nearly spherically symmetry fashion, as shown in Fig. 2.3(a). This allows for greater orbital overlap between neighboring molecules no matter what their relative geometry. In contrast, the frontier orbitals of the TBP and TOL shuttlecocks are fairly localized, with the electron density avoiding the regions near and inside the pentaaryl feathers, as illustrated in Fig. 2.3(b). This means that when the SC molecules are stacked, there is relatively poor overlap of the orbitals on the neighboring molecules: the electron density on the ball of one SC has little to overlap with in the 'bowl' of the next SC in the stack. The non-spherical orbital distribution of the SCs also explains why the electronic coupling in the non-stacking direction is as good as that in the stacked direction.

In summary, our calculations suggest that even though they self-assemble into excellent macroscopic BHJ networks, the electron mobility in pentaarylfullerenes is limited at the local, molecular length scale. Moreover, our calculations also suggest that PCBM is a champion electron acceptor for organic photovoltaics because the electron transfer rate between PCBM molecules is not only outstanding, but also is roughly independent of the molecular geometry. In the next section, we turn to time-resolved microwave conductivity (TRMC) to provide an experimental verification of these ideas concerning local mobility. But most importantly, what these calculations tell us is that if one wishes to create new self-assembling fullerene acceptors, a key design goal must be to have strong orbital overlap between adjacent fullerenes.

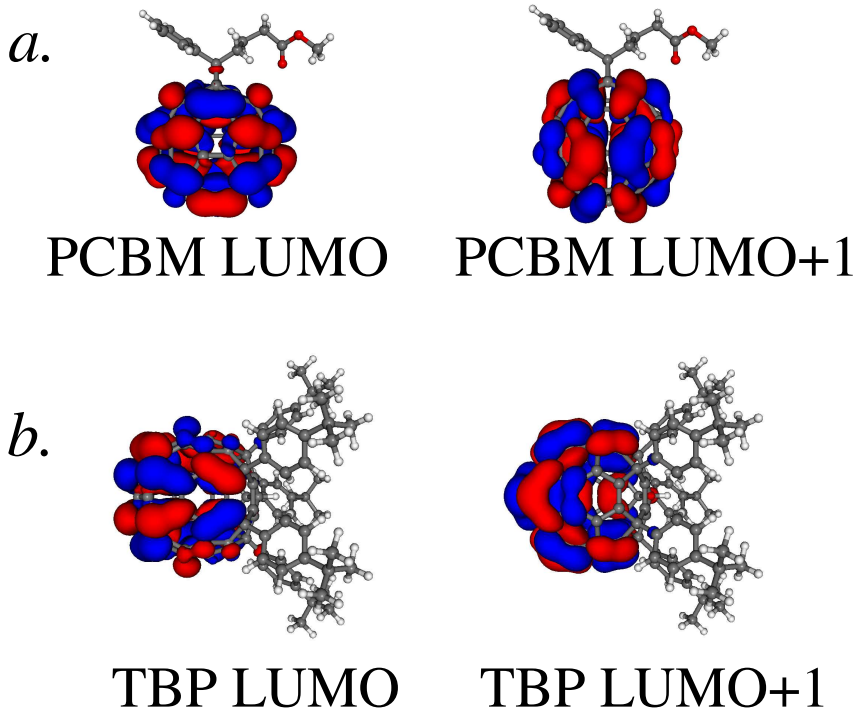

Figure 2.3: Kohn-Sham orbitals from our DFT calculations corresponding to the LUMO and LUMO+1 of the isolated fullerene molecules: (a) PCBM; and (b) 4-*t*Bu. The orbitals were calculated using the B3LYP functional and STO-3G basis set.

CHAPTER 3

Direct delocalization for calculating electron transfer in fullerenes

3.1 Introduction

Due to the large size of fullerene molecules, it is necessary to apply a computationally efficient method for the study of transfer rates. In Chapter 2, we advocated a simple methodology for calculating the coupling between identical molecules in dimeric systems of fullerene derivatives [5]. To reiterate, in spite of the fact that the dimers are chemically identical when they are not placed in a centrosymmetric fashion, the chemical environment seen by each of the individual molecules is different (e.g., see Fig. 2.2). Because of this, the order of the frontier orbitals involved in electron transfer (primarily the LUMO and LUMO+1 orbitals) could be misplaced, for example, in an isolated dimer calculation (where no delocalizing potential is applied), both LUMO and LUMO+1 could be located on the same molecule. In that case, a dimer calculation will show little transfer between the molecules.

To overcome the different-environment problem in isolated dimer calculations, we delocalize the LUMO and LUMO+1 across the two molecules using one of two methods. The first method involves "solvating" the dimer with surrounding molecules. Because the systems are so large, it would be too computationally expensive to explicitly treat solvating molecules; therefore, we solvate the dimer with point charges. The values of the point charges are set self-consistently to

equal the Mulliken charges on the atoms of the dimer. Solving for the values of the point charges is relatively arduous, so we have also shown that the same results can be achieved by applying an electric field to the system to delocalize the frontier orbitals. This method, which we label Delocalizing Field, is much simpler in that one can sweep across a wide range of electric fields to see where the ideal delocalization occurs. However, due to the cost of density functional theory (DFT) simulations on large molecules, the delocalizing field method, while more simple than solvation, is still computationally expensive because it involves a potentially large number of DFT calculations.

We present a substantially more efficient method here. Rather than delocalizing the frontier orbitals with an electric field, we perform a single DFT calculation on a dimer system (here using the B3LYP functional). We then apply a bias directly to the post-self-consistent field (SCF) Fock matrix until the extra electron is balanced evenly between the two molecules in the dimer. We are then able to calculate the transfer rate according to Marcus theory. We show that the new method gives similar results and identical trends to the more complicated methods mentioned above.

The balance of the article is as follows. We present a more detailed description of the methodology in the next section; followed by the Results section, and finally the Discussion section.

3.2 Methodology

Typically, the electron transfer rate is calculated for symmetric organic molecules from the Marcus theory expression [28],

$$k_{MT} = \frac{2\pi}{\hbar}|J_{ij}|^2(4\pi\lambda\kappa_B T)^{-\frac{1}{2}} exp\left(\frac{(\Delta E_{ij}+\lambda)^2}{4\lambda\kappa_B T}\right) \tag{3.1}$$

where i and j denote the initial and final states, located on the donor and acceptor, respectively, J is the transfer integral, ΔE_{ij} is the energy difference between the initial and final states, and λ is the reorganization energy. This expression is appropriate when the electronic states within both the donor and acceptor are well-isolated; however, for large molecules such as fullerenes the distance between electronic states in the valence band is quite small, below 0.1 eV, so that a sum over all initial excited states is required; each initial state will have its own rearrangement energy due to different coupling to the environment vibrational states. Furthermore, in large molecules one does not really calculate the true electronic states but instead uses a single particle (or RPA/TDDFT) approximation, making the degrees of freedom of the other electrons into an effective bath (not necessarily linearly coupled); these can actually enhance the transfer for symmetric systems, unlike vibrational degrees of freedom.

Here we, therefore, use a modified Marcus formalism [68], whereby we sum over all initial states to calculate the total electron transfer rate:

$$k'_{MT} = \frac{2\pi}{\hbar} \sum_{ij} f(\epsilon_i - \mu_L)|J_{ij}|^2 (4\pi\lambda\kappa_B T)^{-\frac{1}{2}} exp\left(\frac{(\Delta E_{ij} + \lambda)^2}{4\lambda\kappa_B T}\right) \tag{3.2}$$

where we introduced the Fermi-Dirac occupation of the donor states, defined as

$$f(\epsilon_i - \mu_0) = \frac{1}{1 + e^{\beta(\epsilon_i - \mu_0)}} \tag{3.3}$$

and ϵ_i is the energy of the donor state. In practice, we report the rate in terms of the transfer time, defined as

$$\tau = \frac{1}{k'_{MT}} \tag{3.4}$$

For the most part, Eq. (3.2) is a straightforward generalization of the Marcus formula for a single pair of states. However, as stated above, each of these

combinations of donor and acceptor states should in principle have a particular rearrangement energy. It is computationally demanding to calculate the reorganization energies for all the initial states, and the whole concept of transfer energy becomes questionable when there are many low lying states; so to simplify, we calculate the transfer rates for a range of values. According to MacKenzie et al. [69], the rearrangement energy for electron transfer in $C_{61}H_2$, that is, a fullerene with the same linker group as PCBM, was calculated to be 0.136 eV when ignoring the outer sphere contribution to the reorganization. We therefore present results for which the reorganization energy was assumed to be 0.1 and 0.15 eV. These choices bracket the relevant range of values and take into account minor differences in the individual couplings and in the outer sphere contribution. While solvent effects are certainly important in electron transfer processes, for computational efficiency, we rely on the reorganization term in the Marcus theory formalism to account for these effects based on prior use of Marcus theory in electron transfer of large molecules (e.g., see Ref. [69]).

The computationally nontrivial aspect of the calculation is the transfer integral. Formally, the flux-operator has the form:

$$\tilde{J} = i[\tilde{F}, \tilde{\theta}] \tag{3.5}$$

where we introduced the Fock operator and the left-theta operator (identity on the left-fragment space, zero on the right); the tilde symbol on the matrices indicates that they refer to an orthogonal basis.

In practice, the calculations are performed by first generating the Fock and overlap matrices, F and S in a nonorthogonal basis using DFT, which has been shown to give good accuracy within the Marcus theory framework [35, 37–41]. The NWChem software package was used for calculations [56]. The matrices were calculated using the B3LYP functional and STO-3G basis set for neutral and

anionic systems. Results for both neutral and anionic systems were similar (i.e., the choice of which Fock operator was used is immaterial in this basis set), and in the results section we use the neutral systems and anionic systems in PCBM, which are in good agreement, and the neutral systems for the other molecules.

The Fock matrix and theta operator are then converted to a local orthogonal basis:

$$\begin{aligned} \tilde{F} &= S^{-\frac{1}{2}} F S^{-\frac{1}{2}} \\ \tilde{\theta} &= S^{-\frac{1}{2}} \theta S^{-\frac{1}{2}} \end{aligned} \tag{3.6}$$

and the theta operator determines whether the orbial of interest is on the left or the right molecule:

$$\theta_{ij} = g(i) S_{ij} g(j) \tag{3.7}$$

where

$$g(i) = \begin{cases} 1, & \text{if } i \in \text{left (donor) fragment} \\ 0, & \text{otherwise} \end{cases} \tag{3.8}$$

We then self-consistently calculate the chemical potential of the neutral and charged species, μ_0 and μ_{-1}, such that the following conditions are met:

$$\begin{aligned} 2Tr[f(\tilde{F} - \mu_0)] &= \sum_{j=1}^{N_o} f(\epsilon_j - \mu_0) = N \\ 2Tr[f(\tilde{F} - \mu_{-1})] &= N + 1 \end{aligned} \tag{3.9}$$

where N is the number of electrons in the neutral system, N_o is the number of orbitals and f is a now a Fermi-Dirac operator

$$f(\tilde{F}\mu_0) = \frac{1}{1 + e^{\beta(\tilde{F} - \mu_0)}} \tag{3.10}$$

The factor 2 in Eq. (3.9) above is due to spin.

We then apply a local bias w to the Fock matrix,

$$\tilde{F} \rightarrow \tilde{F} + w\tilde{\theta} \tag{3.11}$$

such that the extra electron is delocalized evenly between the two fragments. This is essentially the same as applying an external electric field on the system; however, as mentioned, there is significant time saving since the DFT calculation is done only once, and the local bias is applied post SCF convergence.

To calculate the transfer integral, we convert the theta operator into the molecular orbital basis,

$$\tilde{\theta}^E = V^T \tilde{\theta} V \tag{3.12}$$

where V is the eigenvector matrix of the orthogonal-basis Fock matrix, $\tilde{F}$. The transfer integral becomes:

$$J_{ij} = (\epsilon_i - \epsilon_j)\tilde{\theta}^E_{ij} \tag{3.13}$$

The transfer integral is then used to calculate the extended Marcus-theory rate, Eq. (3.2), summing over all initial states.

3.3 Results

We have studied several molecules, as follows: PCBM (Fig. 3.1, penta-(p-t-butylC6H4)-1-hydro-C60 (denoted TBP) (Fig. 2.2(b)), and pentamethyl-monohydro-C60 (denoted $C_{60}Me_5H$) (Fig. 3.2). PCBM is the most commonly used fullerene in organic solar cells, and consists of a phenyl group and butyric acid methyl

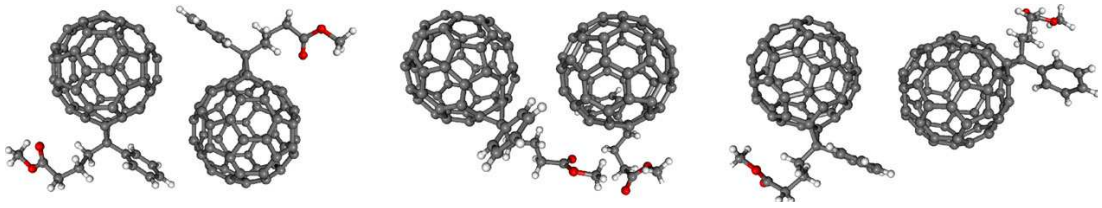

Figure 3.1: The three PCBM orientations studied in this article, denoted in the results section PCBM-1, PCBM-2, and PCBM-3.

ester group attached to the fullerene ball via a methano-linker. Here, we study three dimer orientations of PCBM, each derived from a crystal structure. TBP and $C_{60}Me_5H$ are penta-substituted fullerenes, with tert-butyl phenyl and methyl adducts, respectively; each has an additional hydrogen atom bonded to the fullerene ball to compensate for the breaking of a double bond. The allure of these molecules from a device fabrication perspective is that they tend to self-assemble into columns, which could enhance optimal phase separation in bulk hetero- junction solar cells.

We present data for the extended Marcus theory formalism, that is, summation

	$\lambda = 0.1$ eV		$\lambda = 0.15$ eV	
Dimer	Multiple-state transfer time (fs)	LUMOs transfer time (fs)	Multiple-state transfer time (fs)	LUMOs transfer time (fs)
PCBM-1	335	531	527	950
PCBM-2	322	1710	478	3060
PCBM-3	147	170	251	305
TBP	140,000	773,000	220,000	1,370,000
$C_{60}Me_5H$	24,200	33,800	43,200	60,500

Table 3.1: Results of transfer times with present formalism.

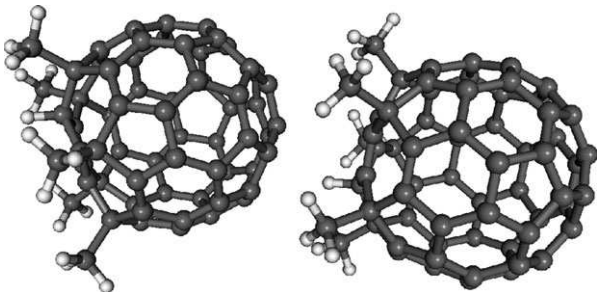

Figure 3.2: $C_{60}Me_5H$.

over all initial states (labeled as "multiple-state transfer time") as well as the traditional Marcus theory formalism, which typically only considers the coupling between the lowest states (LUMOs) on the left and right, which in our language amounts to including only the i, j = LUMO, LUMO+1 (and vice versa) in the sum in Eq. (3.2).

The results for the transfer time, τ, with the present formalism for the alignment potential w [i.e., satisfying Eq. (3.9)] are shown in Table 3.3. Note that in the table we refer to "Multiple-state transfer time," and to "LUMO-transfer time"; these refer to the inverse of the rates in Eqs. (3.2) and (3.1), respectively.

Table 3.3 presents the electron transfer times for PCBM where we calculated the Fock using several methods: neutral system with B3LYP functional, neutral system with PBE functional, and anionic system with PBE functional (we ignore the anionic system with B3LYP functional as B3LYP has been shown to give inadequate results for charged systems). The data show similar results for the three methods, so henceforth we employ the B3LYP functional for neutral species.

Several things in particular stand out about the data. First, we demonstrate that for all the molecules presented, a two-level Marcus formula is insufficient to fully capture the electron transfer behavior. This is because for very large molecules such as fullerene derivatives, the excited states are sufficiently low that they can be thermally excited. Therefore, many levels can be thermally populated

and can contribute to electron transfer.

We also note that for all relative orientations of PCBM, shown in Fig. 3.1, electron transfer rates are very high. Due to the spherical symmetry of the LUMO and LUMO+1 orbitals about the fullerene units in PCBM (shown in Fig. 2.3(a)), the molecule conducts well in a variety of directions, and the rate of transfer is primarily a function of separation between these units. The variation in transfer times and the importance of summing over all initial states is primarily a result of the energy difference between the higher order state and the LUMO. For example, only a minor improvement in transfer time is seen in the third PCBM dimer; in this system, the LUMO+1 and LUMO+2 orbitals are 0.04 and 0.12 eV above the LUMO, respectively. Therefore, the standard Marcus transfer handles this system quite well. Alternatively, in the second PCBM dimer, the LUMO+1 and LUMO+2 are 0.07 and 0.10 eV above the LUMO. This energy difference results in a much more substantial contribution from the LUMO+2.

The results for the variety of methods for TBP are shown in Table 3.3. Comparing the three methods, we note that the total solvation method gives transfer rates about 40% faster than the electric field delocalization and direct delocaliza-

	$\lambda = 0.1$ eV		$\lambda = 0.15$ eV	
Method	Multiple-state transfer time (fs)	LUMOs transfer time (fs)	Multiple-state transfer time (fs)	LUMOs transfer time (fs)
B3LYP neutral	335	531	527	950
PBE neutral	370	747	595	1300
PBE anionic	433	1,100	680	2,000

Table 3.2: Comparison of transfer times with neutral and anionic system in PCBM.

tion, which give very similar results. This is a result of several things. First, the addition of solvating molecules causes the frontier orbitals to have a much greater overlap, that is, the LUMO and LUMO+1 matrix element of the theta operator in the molecular orbital basis is much larger. Second, in the solvation method, the higher order frontier orbitals are closer to the LUMO than in the electric field and direct delocalization methods. For example, in direct delocalization, the LUMO+1 and the LUMO+2 are 5.94×10^{-4} eV and 3.06×10^{-2} eV above the LUMO, respectively; whereas when solvated, these orbitals are 5.10×10^{-4} eV and 2.57×10^{-2} eV above the LUMO. Additionally, excited states higher than the LUMO+2 play only a minor role in electron transfer, as the energy gap above the LUMO prevents significant population. We also note that the transfer times are also more greatly enhanced when one compares the multiple-state method to the LUMOs method. This is due to the higher level orbitals being closer to the LUMO. While the results presented for the several methods for calculating transfer times in TBP vary, we would argue that the solvation method provides the most accurate treatment of the system. The presence of point charges around the dimer, while not explicit treatment of neighboring molecules, most thoroughly mimics the bulk environment of the system. Nonetheless, the direct delocalization method provides a qualitative picture for comparing possible performance device

	$\lambda = 0.1$ eV		$\lambda = 0.15$ eV	
	Multiple-state transfer	LUMOs transfer	Multiple-state transfer	LUMOs transfer
Dimer	time (fs)	time (fs)	time (fs)	time (fs)
Solvated TBP	84,000	3,500,000	141,000	6,220,000
Electric field	128,000	1,120,000	208,000	1,190,000
Direct delocalization	140,000	773,000	2,200,000	1,370,000

Table 3.3: Results for the variety of methods for TBP.

of a number of molecules.

We also investigated the solvent effects of using the polarizable continuum model to solvate a TBP dimer, using the COSMO method in NWChem. We find that similar to calculations on an isolated dimer, the excited state orbitals are localized on a single fragment, and, therefore, no electron transfer is observed. We believe that this unphysical and the polarizable continuum model does not sufficiently capture the electronic behavior of the system. To compare the transfer rates of such a system, we applied the direct delocalization method and find that the multiple-state transfer times are 133,000 and 210,000 fs for reorganization energies of 0.1 and 0.15 eV, respectively. This is in good agreement with our direct delocalization times of the unsolvated dimer.

3.4 Conclusions

We present a simple method to efficiently calculate electron transfer rates between molecular dimers. The method handles vastly asymmetric-placed dimers, where each individual molecule sees a different chemical environment. Additionally, the method is useful in molecules for which higher excited states interact with the frontier orbitals of the system. The proposed method is also highly efficient as it does not require additional DFT calculations.

Of the molecules studied, PCBM and TBP have been fabricated to make OPV devices. According to experiment, PCBM makes significantly more efficient devices than TBP, 5-6% power conversion efficiency versus 1.5% for TBP [67,70,71] . Our study is therefore qualitatively consistent with experiment and can be used to screen new molecules. While our study does not take into account the morphological behavior of these molecules, it gives a good basis for the types of molecules that would make efficient devices. We mention in the Results section, for example, the spherical symmetry of the LUMOs about the fullerene cage provides

multidirectional pathways for electron transfer.

The work presented indicates several important factors relevant in the design of fullerenes for the use of organic solar cells. First, the methano-substituted motif, as in PCBM, conducts electrons well due to the spherical symmetry of the frontier orbitals. Additionally, substitutional motifs that retain this spherical symmetry about the fullerene unit would also make for high transfer rates. We should note, however, that this would not necessarily lead to a top performing cell as the energetics would still need to match those of the electron donor. Nonetheless, the particular motif seems highly efficient.

CHAPTER 4

Breaking the theoretical scaling limit for predicting quasi-particle energies: The stochastic GW approach

4.1 Introduction

The GW approximation [72, 73] to many-body perturbation theory (MBPT) [74] offers a reliable and accessible theory for quasi-particles (QPs) and their energies [73, 75–89], enabling estimation of electronic excitations [2, 90–95], quantum conductance [96–100], and level alignment in hybrid systems [101, 102]. Practical use of GW for large systems is severly limited because of the steep CPU and memory requirements as system size increases. The most computationally intensive element in the GW method, the calculation of the polarization potential (screened Coulomb interaction), involves an algorithmic complexity that scales as the fourth power of the system size [103, 104]. Various approaches have been developed to reduce the computational bottlenecks of the GW approach [79, 89, 93, 103–107]. Despite these advances, GW calculations are still quite expensive for many of the intended application in the fields of materials science, surface sience, and nanosciene.

This chapter outlines a stochastic, orbital-less, formalism for the GW theory, unique in that it does not reference occupied or virtual orbitals and orbital energies in the Kohn-Sham (KS) Hamiltonian. While the approach is inspired by recent

developments in electron structure theory using stochastic orbtials [108–112], it introduces three powerful and basic notions: stochastic decoupling, stochastic matrix compression, and stochastic time-dependent Hartree (sTDH) propagation. The result is a stochastic formulation of GW, where the QP energies become random variable sampled from a distribution with a mean equal to the exact GW energies and a statistical error proportional to the inverse number of stochastic orbitals (iterations, I_{sGW}).

We first illustrate the sGW formalism for silicon nanocrystals (NCs) with varying sizes and band gaps [3, 113] and demonstrate that the CPU time and memory required by sGW scales *nearly linearly* with system size, thereby providing means to study QPs excitations in large systems of experimental and technological interest. We also apply the sGW to several such molecules of interest to the organic photovoltaic community, in particular fullerene and PCBM, and compare the results to experiment. We find the results to be in agreement with experimental QP energies, which ilustrates the sGW method is a powerful tool in predicting energy levels in large organic molecules.

4.2 Methodology

In the reformulation of the GW approach, we treat the QP energy ($\epsilon_{QP} = \hbar\omega_{QP}$) as a perturbative correction to the KS energy [73, 76]:

$$\epsilon_{QP}(\epsilon) = \epsilon + \tilde{\Sigma}^{P}(\omega_{QP};\epsilon) + \Sigma^{X}(\epsilon) - \Sigma^{XC}(\epsilon) \tag{4.1}$$

We view the KS energy ϵ as a variable (rather than an eigenvalue) and the actual values we use is determined from the density of states of the KS Hamiltonian available from the sDFT calculation [111]. For each value of ϵ one needs to evaluate the self energy in Eq. (4.1) given by the sum of the self-energy terms:

$$\begin{aligned}\Sigma^P(t;\epsilon) &= \frac{1}{Q(\epsilon)} tr\left[f_\sigma\left(\hat{h}_{KS}-\epsilon\right)^2 \hat{\Sigma}^P(t;\epsilon)\right] \\ \Sigma^X(\epsilon) &= \frac{1}{Q(\epsilon)} tr\left[f_\sigma\left(\hat{h}_{KS}-\epsilon\right)^2 \hat{\Sigma}^X\right] \\ \Sigma^{XC}(\epsilon) &= \frac{1}{Q(\epsilon)} tr\left[f_\sigma\left(\hat{h}_{KS}-\epsilon\right)^2 v_{XC}\right]\end{aligned} \tag{4.2}$$

The frequency domain polarization self-energy $\Sigma^P(\omega,\epsilon)$ is given in terms of the Fourier transform of the time domain counterpart $\Sigma^P(t,\epsilon)$. $\Sigma^X(\epsilon)$ and $\Sigma^{XC}(\epsilon)$ are the exchange and exchange-correlation self-energies, respectively, and $Q(\epsilon) = tr\left[f_\sigma\left(\hat{h}_{KS}-\epsilon\right)^2\right]$ is a normalization factor. In the above, $v_{XC}(r)$ is the exchange-correlation potential of the KS-DFT Hamiltonian $\hat{h}_{KS}$ and $f_\sigma(\epsilon) = e^{-\epsilon^2/2\sigma^2}$ is an energy filter function of width σ [114]. $\Sigma^X(\epsilon)$, $\Sigma^{XC}(\epsilon)$, and $Q(\epsilon)$ can be calculated using a linear-scaling stochastic approach.

In the GW approximation, the most demanding calculation involves the polarization self-energy, formally given by [73]:

$$\Sigma^P(\boldsymbol{r}_1,\boldsymbol{r}_2,t;\epsilon) = \left\langle \boldsymbol{r}_1 \left| \hat{\Sigma}^P(t;\epsilon) \right| \boldsymbol{r}_2 \right\rangle = i\hbar G_0(\boldsymbol{r}_1,\boldsymbol{r}_2,t) W^P(\boldsymbol{r}_1,\boldsymbol{r}_2,t;\epsilon), \tag{4.3}$$

where

$$i\hbar G_0(\boldsymbol{r}_1,\boldsymbol{r}_2,t) \equiv \left\langle \boldsymbol{r}_1 \left| e^{-i\hat{h}_{KS}t/\hbar}\hat{P}_\mu(t) \right| \boldsymbol{r}_2 \right\rangle \tag{4.4}$$

is the Green function and

$$W^P(\boldsymbol{r}_1,\boldsymbol{r}_2,t;\epsilon) \equiv \langle \boldsymbol{r}_1 | u_C \otimes \chi(t;\epsilon) \otimes u_C | \boldsymbol{r}_2 \rangle \tag{4.5}$$

is the polarization potential. In the above equations, $\hat{P}_\mu(t) \equiv \left[\theta(t) - \theta_\beta\left(\mu - \hat{h}_{KS}\right)\right]$, $\theta(t)$ and $\theta_\beta(E) = \frac{1}{2}[1+\mathrm{erf}(\beta E)]$ are the Heaviside and smoothed Heaviside functions, respectively, μ is the chemical potential, $u_C(|\boldsymbol{r}_1-\boldsymbol{r}_2|) = e^2/4\pi\epsilon_0|\boldsymbol{r}_1-\boldsymbol{r}_2|$ is

the bare Coulomb potential, and $\chi(\boldsymbol{r}_1, \boldsymbol{r}_2, t; \epsilon)$ is the time-ordered density-density correlation function [74]. The symbol $\otimes$ represents a space convolution.

Instead of performing the trace operations in Eqs. (4.2) – (4.5) using the full basis of $\hat{h}_{KS}$, which for large systems is prohibitive, we use real stochastic orbitals $\phi(\boldsymbol{r})$ [115–118] for which formally $\mathbf{1} = \langle|\phi\rangle\langle\phi|\rangle_\phi$ where $\langle ...\rangle_\phi$ denotes a statistical average over ϕ. The choice of $\phi(\boldsymbol{r})$ satisfying these requirements is not unique. The form used here assigns a value of $\pm h^{-3/2}$ at each grid point with equal probability, where h is the grid spacing. This is a crucial step which allows us to rewrite the self-energy in Eq. (4.2) as:

$$\Sigma^P(t;\epsilon) = \left\langle \iint \phi_\epsilon(\boldsymbol{r}_1)\Sigma^P(\boldsymbol{r}_1, \boldsymbol{r}_2, t; \epsilon)\phi(\boldsymbol{r}_2)d^3\boldsymbol{r}_1 d^3\boldsymbol{r}_2 \right\rangle_\phi \tag{4.6}$$

where $|\phi_\epsilon\rangle = f_\sigma(\hat{h}_{KS} - \epsilon)|\phi\rangle$ is the corresponding filtered state at energy ϵ, which can be obtained by a Chebyshev expansion of the Gaussian function with σ chosen as a small parameter [119, 120]. We note in passing that the Chebyshev method enables you to obtain simultaneously $\Sigma^P(t;\epsilon)$ for several values of ϵ.

To obtain $\Sigma^P(\boldsymbol{r}_1, \boldsymbol{r}_2, t; \epsilon)$ in Eq. (4.6) we need to calculate the non-interacting Green function $i\hbar G_0(\boldsymbol{r}_1, \boldsymbol{r}_2, t)$ in Eq. (4.4) and the polarization potential $W^P(\boldsymbol{r}_1, \boldsymbol{r}_2, t; \epsilon)$ in Eq. (4.5). For the former, we introduce an additional set of real stochastic orbitals, $\zeta(\boldsymbol{r})$,and describe it as a stochastic average

$$i\hbar G_0(\boldsymbol{r}_1, \boldsymbol{r}_2, t) = \langle \zeta_\mu(\boldsymbol{r}_1, t)\zeta(\boldsymbol{r}_2)\rangle_\zeta \tag{4.7}$$

where $\zeta_\mu(\boldsymbol{r}_1, t) = \left\langle \boldsymbol{r} \left| e^{-i\hat{h}_{KS}t/\hbar}\hat{P}_\mu(t) \right| \zeta \right\rangle$ is a "propagated projected" stochastic orbtial whcih can be obtained by a Chebyshev expansion of the function $e^{-i\epsilon t/\hbar}[\theta(t) - \theta_\beta(\epsilon - \mu)]$ [119, 120]. One appealing advantage of the stochastic form of Eq. (4.7) is that it provides a compact representation for $G_0(\boldsymbol{r}_1, \boldsymbol{r}_2, t)$, equivalent to matrix compression where $\boldsymbol{r}_1$ and $\boldsymbol{r}_2$ are decoupled. This allows a drastic simplification of the representation of the polarization self-energy obstaing

by combing Eqs. (4.6) and (4.7):

$$\Sigma^P(t;\epsilon) = \langle\langle \phi_\epsilon \zeta_\mu(t)^* \left| u_C \otimes \chi(t) \otimes u_C \right| \zeta\phi \rangle\rangle_{\phi\zeta} \,. \tag{4.8}$$

Next, we employ a temporal decoupling scheme by introducing an additional set of real stochastic orbitals $\psi(\boldsymbol{r})$:

$$\Sigma^P(t;\epsilon) = \langle\langle \phi_\epsilon \zeta_\mu(t)^* \left| \psi \right\rangle \left\langle \psi \right| u_C \otimes \chi(t) \otimes u_C \left| \zeta\phi \right\rangle\rangle_{\phi\zeta\psi} \,, \tag{4.9}$$

which allows us to disassociate the two temporal terms $\langle \phi_\epsilon \zeta_\mu(t)^* | \psi \rangle$ and $\langle \psi | u_C \otimes \chi(t) \otimes u_C | \zeta\phi \rangle$. Note that the average $\langle ... \rangle_{\phi\zeta\psi}$ in Eq. (4.9) is performed over I_{sGW} pairs of ϕ and ζ stochastic orbitals, and for each such pair we use a different set of N_ψ stochastic ψs. The term $\langle \phi_\epsilon \zeta_\mu(t)^* | \psi \rangle$ is straightforward to obtain while $\langle \psi | u_C \otimes \chi(t) \otimes u_C | \zeta\phi \rangle$ is determined from the time-retarded polarization potential, $\langle \psi | u_C \otimes \chi^r(t) \otimes u_C | \zeta\phi \rangle$, calculated from the linear response relation:

$$\left\langle \psi \left| u_C \otimes \chi^r(t) \otimes u_C \right| \zeta\phi \right\rangle = \left\langle \psi \left| u_C \right| \delta n(t) \right\rangle , \tag{4.10}$$

where $\delta n(\boldsymbol{r}, t)$ is the causal density response to the impulsive perturbation $\delta v(\boldsymbol{r}, t) = \langle \boldsymbol{r} | u_C | \zeta\phi \rangle \delta(t)$ calculated by the time-dependent Hartree (TDH) approach [54, 121, 122]. Alternatively, a full time-dependent density functional theory (TDDFT) propagation [123] is often found to yield better QP energies than the TDH propagation [2]. Once the retarted response $\langle \psi | u_C | \delta n(t) \rangle$ is calculated and stored for each time t, the corresponding time-ordered response $\langle \psi | u_C \otimes \chi(t) \otimes u_C | \zeta\phi \rangle$ is obtained by a standard transformation [74].

The TDH (or TDDFT) propagation is usually performed using the full set of occupied KS eigenfunctions, but we deliberately avoid these in our formulation. Instead, we introduce, once again, a stochastic way to perform the TDH or TDDFT propagation where a new set of N_φ occupied projected stochastic orbitals, $\varphi_\mu(\boldsymbol{r}, 0) = \langle \boldsymbol{r} | \theta(\mu - \hat{h}_{KS}) | \varphi \rangle$ are used (as before, $\varphi(\boldsymbol{r})$ are real random

orbitals for which $\mathbf{1} = \langle|\varphi\rangle\langle\varphi|\rangle_\varphi$). The so-called sTDH (or sTDDFT) propagation is carried out identically to a TDH propagation, except one propagates only the N_φ stochastic orbtials and at each time step (rather than all ocupied orbitals), and the density is calculated as $n(\boldsymbol{r}, t) = \langle|\varphi(\boldsymbol{r}, t)|^2\rangle_\varphi$ from which the Hartree potential is updated in the usual way. We verified that for a given accuracy the number of propagated orbtials N_φ does not increase (and actually somewhat decreases) with system size. This suggests that the computational complexity (storage and compuational time) of the sTDH (or sTDDFT) step scales linearly with system size.

4.3 Results

We validate our formalism by first applying it to a small model system where a deterministic GW calculation is available as a benchmark. In Fig. 4.1 we show the estimates for the real part of the polarization self-energy, obtained by both the deterministic and the stochastic methods. The stochastic calculation employed a large number of iterations ($I_{sGW} = 10,000$) to achieve a small statistical error. The agreement between the results of the two calculations for all relevant frequencies as seen in Fig. 4.1 is impressive for both the highest quasihole and lowest quasielectron levels, validating the stochastic formulation.

Next we performed a set of sGW calculation for a series of hydrogen passivated silicon NCs as detailed in Table 4.1. The sDFT [111] method was used to generate the KS Hamiltonian within the local density approximation (LDA). The calculation employed a real-space grid of spacing $h = 0.6a_0$, the Troullier-Martins norm-conserving pseudopotentials [124], and fast Fourier transforms for implementing the kinetic and Hartree energies. The CPU time needed to converge the sDFT to a stistical error in the total energy per electron of about 10 meV was ≈ 5000 hrs for the entrire range of systems studied.

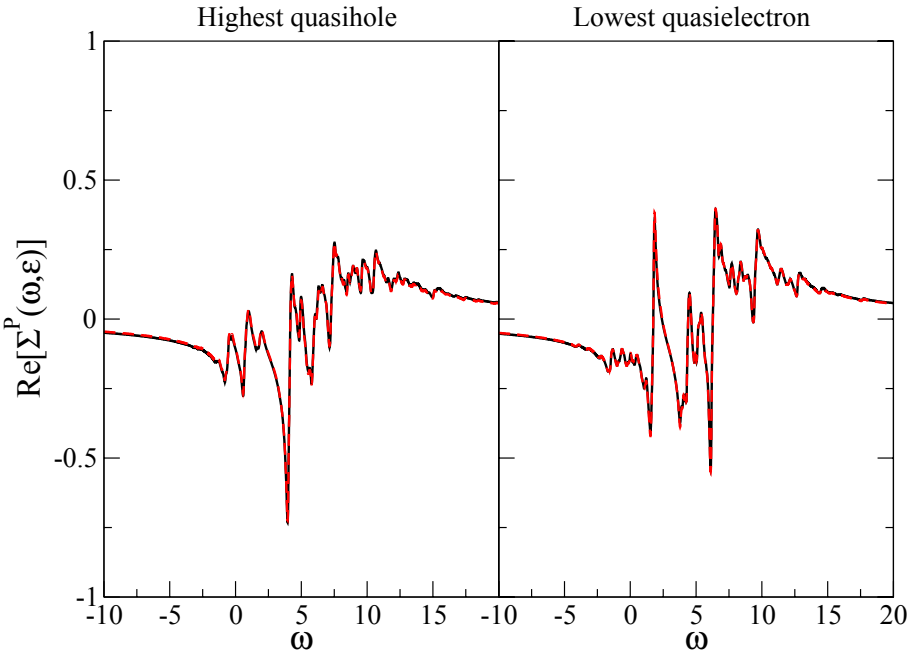

Figure 4.1: Comparison of the schochastic (dashed red) and deterministic (black) estimates of the real part of the polarization self-energy $\Sigma^X(\omega, \epsilon)$ for the 14 electron benchmark model corresponding to the highest quasihole and lowest quasielectron levels. Frequency scale in atomic units.

In the lower panel of Fig. 4.2 we plot the QP energies of the highest quasihole and lowest quasielectron levels for the silicon NCs. We have used $I_{sGW} = 1000$ stochastic iterations, each one involviong one pair or random ϕ and ζ orbitals, and a set of $N_\psi = 100$ stochastic ψ orbitals. As can be seen, the statistical error in the values of the QP energies is very small (<0.1 eV) and can be reduced by increasing I_{sGW}. The quasihole (quasielectron) energy increases (decreases) with system size dues to the quantum confinement effect. The quasiparticle energies tend to plateau and approach the bulk value as the size of the NC increases. The onset of the plateau for electrons seems to exceed the size systems studied. This is consistent with the fact that the effective mass of the electron is smaller than that of the hole. The middle panel of Fig. 4.2 shows the QP energy difference

from the KS values for the holes and electrons. Larger deviations are observed for small NCs in the strong confinement regime. The corrections for the holes are larger than that for the electrons. This is rather surprising, given that for small systems, the error in the frontier orbital energies in KS-DFT within LDA should be divided equally between the electron and the hole [125, 126].

The upper panel of Fig. 4.2 shows the CPU time scaling of the entire sGW approach for the combined calculation of $\Sigma^X(\epsilon)$, $\Sigma^{XC}(\epsilon)$, and $\Sigma^P(t,\epsilon)$. The scaling is nearly linear with the number of electrons, breaking the quadratic theoretical limit. This near-linear scaling behavior kicks in already for the smallest system studied, and therefore the stochastic method outperforms the ordinary $O(N^4)$ GW approach for systems studied beyond SiH_4. It is important to note that for almost the entire range of NC sizes the sGW calculations were cheaper than the sDFT.

We have also test the sGW approach on PCBM, a large nonsymmetric system.

						$E_{\text{gap}}^{\text{QP}}$ (eV)		
System	N_e	N_g	I_{sDFT}	N_φ	β_{GW}^{-1}	sGW	GW_f	ΔSCF
$Si_{35}H_{36}$	176	60^3	3000	16	0.020	6.2	7.0[a]	6.2[a]
$Si_{87}H_{76}$	424	64^3	1600	16	0.012	4.8		
$Si_{147}H_{100}$	688	70^3	800	16	0.010	4.1	5.0[a]	4.1[a]
$Si_{353}H_{196}$	1608	90^3	400	16	0.008	3.0		2.9[b]
$Si_{705}H_{300}$	3120	108^3	200	16	0.007	2.2		2.4[b]

Table 4.1: The of electrons (N_e), size of grid (N_g), number of sDFT iterations (I_{sDFT}), number of stochastic orbitals in sTDDFT (N_φ), the value of $\beta_{GW}^{-1}(E_h)$ in the sGW calculation, and the resulting QP energy gap (E_{gap}^{QP}) compared to GW_f (taken from [2]) and self-consistent-field energy differences (ΔSCF) (taken from [3]) calculations.

We obtained $\epsilon_{QP} = 7.1 \pm 0.1$eV for the hole and $\epsilon_{QP} = 3.4 \pm 0.1$eV for the electron using $I = 600$ iterations. These results can be compared to the experimental results ofr the ionization potential $E_{\mathrm{IP}} = 7.17$eV and the electron affinity $E_{\mathrm{EA}} = 2.633$V [127, 128]. The agreement for the electron affinity can be improved by replacing the RPA screening with TDDFT screening [129], which gives $\epsilon_{QP} = 2.5 \pm 0.1$eV for the electron. We find similar behavior for C_{60}. The results are summarized in Table 4.2. The error per iteration is thus similar to that of the symmetric silicon nanocrystalline systems.

PCBM			C_{60}	
method	IP	EA	IP	EA
sGW(TDH)	7.75	3.36	7.78	3.70
sGW (TDDFT)	6.38	2.51	6.80	2.78
experiment	7.17	2.63	7.6	2.7

Table 4.2: Comparison ionization potentials and electron affinites between sGW and experiment. Quasiparticle energies using sGW were calculating using both TDH and full TDDFT.

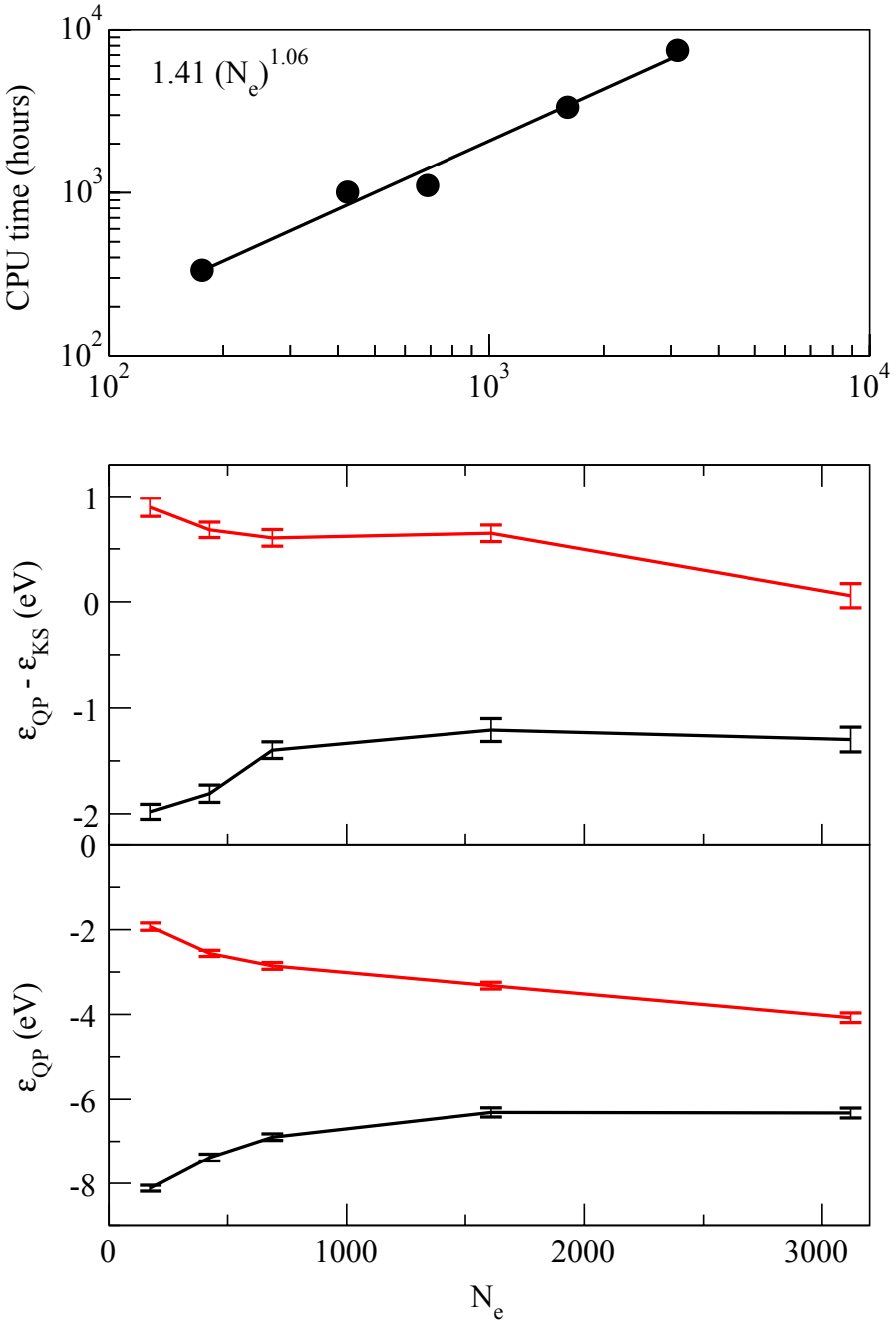

Figure 4.2: Lower panel: QP energies for the highest quasihole (black) and lowest quasielectron (red) levels. Middle pane: QP energy difference from the KS energy for the highest quasihole (black) and lowest quasielectron (red) levels. Upper panel: CPU time versus the number of electrons. The power law fit (solid line) yields an exponent close to 1.

4.4 Conclusion

In conclusion, we have reformulated the GW approximation to MBPT for QP energies as a stochastic process without directly referring to KS eigenstates (or, equivalently, the single-particle density matrix). The sGW approximation is a fully quantum paradigm shift and removes the main obstacle for addressing large systems up to the mesoscopic limit. Indeed, the application to silicon NCs of size far exceeding the current state-of-the-art indicates that the complexity is near linear with system size, breaking the theoretical limit. Some fo the concepts presented here may be applicable to other forms of MBPT, such as propagators [130] and Green function theories.

The sGW method developed here has several appealing advantages: (i) Representation: It is especially suitable for real-space-grid and/or plane-wave pseudopotential representations for which the Hamiltonian operation on a stochastic orbital scales linearly. These representations are natural for large-scale electronic structure computations. The approach is also useful for periodic systems with very large super-cells. (ii) CPU time scaling: The present method enables a GW calculation that scales near linearly in CPU time. Existing methods have been able to reduce the complexity to cubic and it was implicitly assumed that linear scaling is impossible due to the complexity of RPA. The present method circumvents this by developing sTDH. The scaling of our approach is insensitive to the sparsity of the density matrix and thus represents a significant improvement over existing GW implementations. (iii) Storage scaling (matrix compression): The introduction of stochastic orbitals circumvents the need to store huge matrices of the Green function and the polarization potential (or the inverse dielectric matrix ϵ^{-1}, etc.), thus acheiving considerable savings in memory. The scaling of storage is $O(N_g)$, which makes the sGW calculation applicable to a large system without recourse to various energy cutoff approximations in the unoccupied space [84, 131, 132].

(iv) Parallelization: The stochastic character of the sGW formalism allows for straightforward parallelization—self-energies are averaged over different stochastic orbitals and each processor performs its own independent contribution to this average.

These features make sGW the method of choice for studying QP excitations in large complex materials not accessible by other approaches.

Appendix 4.A Using stochastic orbitals

4.A.1 Real random orbitals

A real random orbital $\zeta(\boldsymbol{r})$ is a set of random numbers associated with each grid point and can take the values $\pm h^{-3/2}$ with equal probability, where h is the grid spacing. In the algorithm below by "draw a random orbital" we mean that one has to produce by a pseudorandom number generator a sample of $\zeta(\boldsymbol{r})$.

The mean of the projection $\langle|\zeta\rangle\langle\zeta|\rangle_\zeta$ is the unit operator on the grid:

$$\langle|\zeta\rangle\langle\zeta|\rangle_\zeta = \hat{\mathbf{1}}.$$

For an operator $\hat{A}$ the stochastic trace formula is

$$\mathrm{tr}\left[\hat{A}\right] = \left\langle\left\langle \zeta \left| \hat{A} \right| \zeta \right\rangle\right\rangle_\zeta .$$

4.A.2 Chebyshev evaluation

The algorithm below assumes we need to compute the self-energy $\tilde{\Sigma}(\omega;\epsilon)$ for several Kohn-Sham energies ϵ (say, ϵ_n, $n = 1, ..., N_\epsilon$). A filtered real random orbital is associated with each energy ϵ using an appropriate filtered $\phi_\epsilon = f_\sigma(\hat{h}_{KS} - \epsilon)\phi$ where ϕ is a random orbital.

The filter function $f_\sigma(\hat{h}_{KS} - \epsilon)$ is applied onto ϕ using Chebyshev expan-

sion techniques by which $\phi_\epsilon = \sum_m c_m(\epsilon)\phi_m$ where $\phi_0 = \phi$, $\phi_1 = \hat{h}\phi$ and the following iteration is used for the other terms: $\phi_{m+1} = 2\hat{h}\phi_m - \phi_{m-1}$. Note that only 3 auxilary wave functions are needed for applying this series. Here, $\hat{h} = \frac{\hat{h}_{KS} - \overline{h}}{\Delta h}$ is a shifted-scaled Hamiltonian, such that the eigenvalues of $\hat{h}$ are contained in the interval [-1,1] and the expansion coefficients are obtaned from $c_m(\epsilon) = \int_0^\pi f_\sigma(\Delta h \cos\theta + \overline{h} - \epsilon)\cos m\theta d\theta$.

When ϕ_ϵ for several values of the parameters ϵ are needed one can save numerical effort by exploiting the fact that ϵ_m are not ϵ dependent and thus summing $\phi_\epsilon = \sum_m c_m(\epsilon)\phi_m$ simultaneously for all values of ϵ.

4.A.3 The use of ϕ

For evaluating the expectation value

$$a_\epsilon = Q(\epsilon)^{-1} tr\left[f_\sigma\left(\hat{h}_K S - \epsilon\right)^2 \hat{A}\right],$$

where

$$Q(\epsilon) = tr\left[f_\sigma\left(\hat{h}_{KS} - \epsilon\right)^2\right],$$

one can use the stochastic trace formula

$$a_\epsilon = Q(\epsilon)^{-1}\left\langle\left\langle \phi_\epsilon \left|\hat{A}\right| \phi\epsilon\right\rangle\right\rangle_\phi,$$
$$Q(\epsilon) = \langle\langle\phi_\epsilon|\phi_\epsilon\rangle\rangle_\phi.$$

However, this is expensive numerically, since one needs to operate with $\hat{A}$ on ϕ N_ϵ times, for each desired value of ϵ. Instead, one can define $\overline{\phi} = \sum_\epsilon \phi_\epsilon$ and then $a_\epsilon = Q(\epsilon)^{-1}\left\langle\left\langle \phi_\epsilon \left|\hat{A}\right| \overline{\phi}\right\rangle\right\rangle_\phi$, where now $Q(\epsilon) = \left\langle\left\langle \phi_\epsilon|\overline{\phi}\right\rangle\right\rangle_\phi$. Since $\overline{\phi}$ does not depend on ϵ, one has to act with $\hat{A}$ on $\overline{\phi}$ only once and then for each value of ϵ perform the stochastic average to obtain a_ϵ.

4.A.4 Matrix/Operator compression and decoupling

Given and operator $\hat{A}$ we draw a random orbital $\zeta(\boldsymbol{r})$ and $\hat{A} = \left\langle \hat{A}|\zeta\rangle\langle\zeta| \right\rangle_\zeta = \langle|\zeta_A\rangle\langle\zeta|\rangle_\zeta$; therefore, as a grid-matrix:$\left\langle \boldsymbol{r}_1 \left| \hat{A} \right| \boldsymbol{r}_2 \right\rangle = \langle\zeta_A(\boldsymbol{r}_1)\zeta(\boldsymbol{r}_2)^*\rangle_\zeta$ and one achieves a compact and "decoupled" stochastic representation of $\hat{A}$.

4.A.5 Compression of the density matrix and the exchange self-energy

The exchange self-energy at orbital energy ϵ can be obtained by one of two choices. The first uses $\overline{\phi}$ and ϕ_ϵ as defined above to calculate the exchange self-energy for all sampled energies simultaneously:

$$\Sigma^X(\epsilon) = -\frac{1}{\langle\langle\phi_\epsilon|\overline{\phi}\rangle\rangle_\phi} \left\langle \iint \phi_\epsilon(\boldsymbol{r}_1)\frac{\rho(\boldsymbol{r}_1,\boldsymbol{r}_2)}{|\boldsymbol{r}_1-\boldsymbol{r}_2|}\overline{\phi}(\boldsymbol{r}_2)d^3\boldsymbol{r}_1 d^3\boldsymbol{r}_2 \right\rangle_\phi . \tag{4.11}$$

For large enough β ($\beta \gg \frac{1}{E_g}$, where E_g is the QP gap), the density matrix (DM), $\rho(\boldsymbol{r}_1,\boldsymbol{r}_2)$, can be expressed as the matrix elements of the operator

$$\hat{\rho} \equiv \theta_\beta\left(\mu - \hat{h}_{KS}\right) = \frac{1}{2}\left\{1 + \mathrm{erf}\left[\beta\left(\mu - \hat{h}_{KS}\right)\right]\right\} \tag{4.12}$$

where $\hat{h}_{KS}$ is the KS Hamilonian and μ is the chemical potential. Since $\hat{\rho} = \hat{\rho}^2$, one can define a compact representation of $\hat{\rho}$ in terms of a new set of stochastic orbitals, φ, as $\langle\varphi_\mu(\boldsymbol{r}_1)\varphi_\mu(\boldsymbol{r}_2)^*\rangle_\varphi$, where $\varphi_\mu = \frac{1}{2}\left[1 + \mathrm{erf}\left[\beta\left(\mu - \hat{h}_{KS}\right)\right]\right]\varphi$. Note that these are exactly the same orbitals used for the stochastic time propagation. Using this representation of $\hat{\rho}$, we rewrite the exhange self energy as:

$$\Sigma^X(\epsilon) = -\frac{1}{\langle\langle\phi_\epsilon|\overline{\phi}\rangle\rangle_\phi} \left\langle \iint d^3\boldsymbol{r}_1 d^3\boldsymbol{r}_2 \phi_\epsilon(\boldsymbol{r}_1)\varphi_\mu(\boldsymbol{r}_1)\frac{1}{|\boldsymbol{r}_1-\boldsymbol{r}_2|}\varphi_\mu(\boldsymbol{r}_2)\overline{\phi}(\boldsymbol{r}_2) \right\rangle_{\varphi\phi} . \tag{4.13}$$

For every pair of random orbitals φ and ϕ we need to compute φ_μ, ϕ_ϵ, and $\overline{\phi} = \sum_\epsilon \phi_\epsilon$, and then through a Fourier transform perform the convolution to obtain

the exchange energy.

The second variant uses the fact that most of the numerical effort in the exchange energy goes towards the determination of the orbitals φ_μ rather than the actual calculation of the exchange integral in Eq. (4.13). Therefore, a better numerical convergence with very little additional cost is achieved if the exchange energy is calculated for each energy separately, replace $\overline{\phi}$ by ϕ_ϵ:

$$\Sigma^X(\epsilon) = -\frac{1}{\langle\langle\phi_\epsilon|\phi_\epsilon\rangle\rangle_\phi}\left\langle\iint d^3\boldsymbol{r}_1 d^3\boldsymbol{r}_2 \phi_\epsilon(\boldsymbol{r}_1)\varphi_\mu(\boldsymbol{r}_1)\frac{1}{|\boldsymbol{r}_1-\boldsymbol{r}_2|}\varphi_\mu(\boldsymbol{r}_2)\phi_\epsilon(\boldsymbol{r}_2)\right\rangle_{\varphi\phi}.$$

This is the variant we used in the computations reported in this chapter. We find that for a fixed statistical error, the number of φ's and ϕ's is independent of system size, which implies that the calulations of the exchange self-energy is scaling linearly.

Appendix 4.B Algorithm

The steps below are done I_{sGW} times. In each stochastic sampling we

1. Draw a real random orbital $\zeta(\boldsymbol{r})$ and a real random orbital $\phi(\boldsymbol{r})$ and by filtering produce $\phi_\epsilon(\boldsymbol{r}) = \left\langle \boldsymbol{r}\left| f_\sigma\left(\hat{h}_{KS}-\epsilon\right)\right|\phi\right\rangle$. Generate $\overline{\phi} = \sum_\epsilon \phi_\epsilon$. Typically we filtered two or four orbitals simultaneously, e.g., two near the HOMO and two near the LUMO. This is done with a single Chebyshev expansion, as explained above.

2. Add the contribution to the exchange energy, $\int v_{XC}(\boldsymbol{r})|\phi_\epsilon(\boldsymbol{r})|^2 d^3\boldsymbol{r}$, and the contributions $\int |\phi_\epsilon(\boldsymbol{r})|^2 d^3\boldsymbol{r}$ and $\int \phi_\epsilon(\boldsymbol{r})\overline{\phi}(\boldsymbol{r})d\boldsymbol{r}$ to the denominators, $Q(\epsilon) = \langle\langle\phi_\epsilon|\overline{\phi}\rangle\rangle$ (used for the polarization) and $\langle\langle\phi_\epsilon|\phi_\epsilon\rangle\rangle$ (used for the exchange and the Kohn-Sham energy).

3. Draw N_ψ real random orbitals $\psi_l(\boldsymbol{r})$, $l = 1, ..., N_\psi$. These will be used to

generate $W^r(\zeta\phi_\epsilon, \psi_l, t_k)$ and $\langle\phi_\epsilon\overline{\zeta}(t)^*|\psi_l\rangle$ in steps 5 and 8.

4. Calculate $\Delta(\boldsymbol{r}) = \int u_C(\boldsymbol{r}-\boldsymbol{r}')\zeta(\boldsymbol{r}')\overline{\phi}(\boldsymbol{r}')d^3\boldsymbol{r}'$.

5. Draw N_{TDH} random orbitals $\varphi_m(\boldsymbol{r})$, $m = 1, ..., N_{TDH}$ and project each one on the occupied space: $\varphi_{m,\mu}(\boldsymbol{r}) = \left\langle \boldsymbol{r} \left| \theta_\beta\left(\mu - \hat{h}_{KS}\right) \right| \varphi_m \right\rangle$. These orbitals are then used for two purposes:

   (a) Evaluate the Fock exchange self-energy for which we accumulate the contribution:

   $$-\frac{1}{N_{TDH}} \sum_{m=1}^{N_{TDH}} \iint \phi_\epsilon(\boldsymbol{r})\varphi_{m,\mu}(\boldsymbol{r})u_C(|\boldsymbol{r}-\boldsymbol{r}'|)\phi_\epsilon(\boldsymbol{r}')\varphi_{m,\mu}(\boldsymbol{r}')d^3\boldsymbol{r}d^3\boldsymbol{r}'. \tag{4.14}$$

   (b) Propagate the orbitals using the stochastic time-dependent Hartree equations (only for positive times):

   $$\begin{aligned} i\hbar\dot{\varphi}_{m,\mu}(\boldsymbol{r},t) &= \left[\hat{h}_{KS} + \int \frac{\delta n(\boldsymbol{r}',t)}{|\boldsymbol{r}-\boldsymbol{r}'|}d^3\boldsymbol{r}'\right]\varphi_{m,\mu}(\boldsymbol{r},t) \\ \delta n(\boldsymbol{r},t) &= \frac{2}{N_{TDH}} \sum_{m=1}^{N_{TDH}} \left(|\varphi_{m,\mu}(\boldsymbol{r},t)|^2 - |\varphi_{m,\mu}(\boldsymbol{r},0)|^2\right) \end{aligned} \tag{4.15}$$

   This is done on a time grid $t = \tau\delta t$, $\delta t \equiv \frac{T}{N_T}$, $\tau = -N_T, ..., N_T$ containing $2N_T + 1$ points for a maximum time $T \approx 100\hbar E_h^{-1}$ using a split operator technique with $\delta t = 0.05$au. The propagation is done twice:

   i. For an initial state $\varphi^i_{m,\mu}(\boldsymbol{r}, t=0) = e^{-i\Delta(\boldsymbol{r})\eta}\varphi_{m,\mu}(\boldsymbol{r})$.

   ii. For an initial state $\varphi^{ii}_{m,\mu}(\boldsymbol{r}, t=0) = \varphi_{m,\mu}(\boldsymbol{r})$.

6. Use $\Delta n(\boldsymbol{r}, \tau\delta t) = \frac{1}{\eta}[\delta n^i(\boldsymbol{r}, \tau\delta t) - \delta n^{ii}(\boldsymbol{r}, \tau\delta t)]$ to form N_ψ time-dependent retarted (r) overlaps:

   $$W^r(\epsilon, l, \tau) = \theta(\tau\delta t) \iint d^3\boldsymbol{r}_1 d^3\boldsymbol{r}_2 \psi_l(\boldsymbol{r}_1) \int u_C(\boldsymbol{r}_1 - \boldsymbol{r}_2)\Delta n(\boldsymbol{r}_2, \tau\delta t). \tag{4.16}$$

7. Multiply the time-dependent overlaps $W^r(\epsilon, l, \tau)$ by a regularization function $g(\tau\delta t) = \exp\left\{-\frac{(\Gamma\tau\delta t)^2}{2}\right\}$, where Γ is a damping parameter (typically we set

$\Gamma = 0.03\hbar^{-1}E_h$). Performing the transformation

$$\tilde{W}(\epsilon, l, \omega_\tau) = \tilde{W}^r(\epsilon, l, \omega_\tau)\theta(\omega_\tau) + \tilde{W}^r(\epsilon, l, \omega_\tau)^*\theta(-\omega_\tau) \tag{4.17}$$

where $\tilde{W}^r(\epsilon, l, \omega_\tau)$ is the discrete Fourier transform of $W^r(\epsilon, l, \tau)$. Transform $\tilde{W}(\epsilon, l, \omega_\tau)$ back to the time domain to generate the time-ordered overlaps $W(\epsilon, l, \tau)$.

8. Filter the random orbitals ζ to yield its occupied and unoccupied parts,

$$\begin{aligned} \zeta^-(\boldsymbol{r}, t=0) &= \langle \boldsymbol{r}|\theta_\beta(\mu - \hat{h}_{KS})\rangle \\ \zeta^+(\boldsymbol{r}, t=0) &= \zeta(\boldsymbol{r}) - \zeta^-(\boldsymbol{r}, t=0) \end{aligned} \tag{4.18}$$

9. Propagate ζ^+ forward in time and ζ^- backward in time under $\hat{h}_{KS}$.

10. Calculate and store $G(\epsilon, l, \tau) = \langle \phi_\epsilon \overline{\zeta}(\tau\delta t)^*|\psi_l\rangle$, where $\overline{\zeta} = \theta(t)\zeta^+(t) - \theta(-t)\zeta^-(-t)$.

11. Average the polarization self-energy

$$\Sigma^P(\tau\delta t, \epsilon) = \frac{g(\tau\delta t)}{N_\psi}\sum_{l=1}^{N_\psi}\langle G(\epsilon, l\tau)W(\epsilon, l, \tau)\rangle_{\phi\zeta}.$$

At the end of the stochastic iterations, Eq. (4.1) is solved to yield the final quasiparticle energy.

CHAPTER 5

Modeling molecular effects on plasmonic transport

5.1 Introduction

Plasmonic materials [133, 134], where electrons oscillate collectively, are interesting to study due to a wide range of properties. Plasmon frequencies are tunable by modifying size [135], shape [136], and geometry [137]. The propagation and transmission of surface plasmons through plasmonic materials can be specifically modulated [138], including subwavelength focusing of electromagnetic energy [139]. Plasmonic materials also generate highly intense fields at their surfaces when excited [133], resulting in a strong interaction with neighboring molecules [140]. The most common example is surface enhanced Raman spectroscopy, where intense fields lead to very sensitive measurements (up to 15 orders of magnitude more sensitive than that of the traditional Raman spectroscopy) [141]. Recently, chlorophyll has been shown to have an 18-fold increase in fluorescence as a result of plasmon interactions when placed near a silver surface [142].

Given the intensity of the fields surrounding excited plasmonic materials, it is not surprising that these materials have a strong effect on neighboring molecules. It is remarkable that a few [143] or even individual molecules can also greatly affect a plasmonic material. We have recently shown that two-level molecules can rotate plasmon polarization transmitted between nearby nanoparticles as well as greatly affect the energy transmission [144]. To expand this work, we investigate the effect

of a large fluorophore having a strong transition dipole moment on the polarization and transmission of current through similar arrays of metal nanoparticles.

In previous papers [144, 145] on a two-level molecule, we showed that for a pronounced effect on the polarization and transmission of current through metal nanoparticles to occur, the molecule must have an excitation energy similar to the plasmon resonance frequency of the metal. Here, we investigate the effects on silver nanoparticles, and therefore chose a yellow fluorophore, tartrazine (Fig. 5.1), as its excitation energy is similar to the plasmon resonance frequency of silver. While Ref. [144] studies a similar system with a two-level model for the molecule, a more thorough study is warranted. Two-level systems could have vastly different properties in principle; primarily, this is because each time the molecule is excited it relaxes to the same ground level. A realistic description of a molecule, with its variety of excited states and a wide absorption profile could yield very different results, which, a priori, could have masked the effect. Fortunately, as we show below, this is not the case, and a strong molecular effect remains.

On the length scales relevant to metal nanoparticles, metal electrons can be well treated classically [146]. We thus employ the finite-difference time-domain (FDTD) method, which has been shown to accurately model metal nanoparticles [147]. The molecule was subsequently modeled using time-dependent parameterized method number 3 (TDPM3), a time-dependent version of a semiempirical quantum mechanical routine [148]. TDPM3 was chosen over more common methods such as time-dependent density functional theory (TDDFT) as it is significantly faster.

TDPM3 has recently been shown to fairly accurately model large organic molecules, yielding excitation energies within 15% of experiment and TDDFT [45]. The method is very efficient because of the ease of applying the Fock operator and the small (minimal) basis set. Thus, TDPM3 allows the simulation of large fluorophores, which have a strong transition dipole moment.

The resulting simulations, discussed below, show that a single molecule can

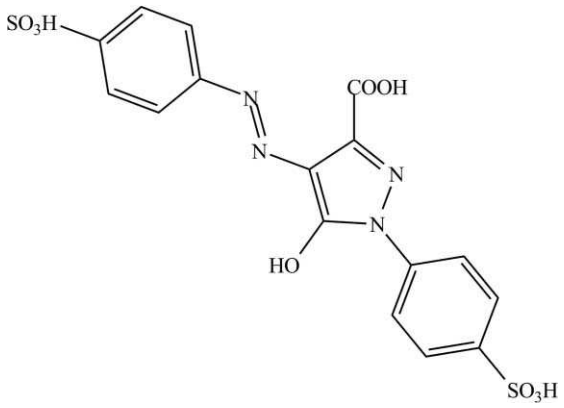

Figure 5.1: The yellow fluorophore tartrazine as oriented in this work.

sufficiently modify the transmitted current and rotate its direction to potentially conceive devices that could measure such a change in the y-polarized current and give single molecule detection. Further, future simulations will investigate how plasmon propagation can be modified by a larger set of molecules.

Section II A describes the FDTD method used to model the silver nanoparticles, Sec. II B the TDPM3 method used for the molecule, and Sec. II C the interaction between the two. Section III describes the investigated system and discusses the results. Conclusions follow in Sec. IV.

5.2 Theory

5.2.1 Classical treatment

To treat the metal and vacuum background classically, we set interlocking Yee grids to describe the electric field, magnetic field, and plasmon generated current [146]. To avoid double counting of the self-interaction of the molecule (beyond the inherent Coulomb integrals in the time-dependent TDPM3 Hamiltonian), we also establish such grids for a separate molecule-induced field, so that the molecule is only influenced by the external field and by the TDPM3 Hamiltonian, and not

by its induced electric field.

We label the fields generated by the molecule with subscript m and the fields generated by the plasmons with subscript p. Thus, the total fields are (see Ref. [144])

$$\boldsymbol{E}_{tot}(\boldsymbol{r},t) = \boldsymbol{E}_p(\boldsymbol{r},t) + \boldsymbol{E}_m(\boldsymbol{r},t) \tag{5.1}$$

$$\boldsymbol{H}_{tot}(\boldsymbol{r},t) = \boldsymbol{H}_p(\boldsymbol{r},t) + \boldsymbol{H}_m(\boldsymbol{r},t) \tag{5.2}$$

$$\boldsymbol{J}_{tot}(\boldsymbol{r},t) = \boldsymbol{J}_p(\boldsymbol{r},t) + \boldsymbol{J}_m(\boldsymbol{r},t) \tag{5.3}$$

The total fields are defined and evolved in time in terms of the Maxwell equations:

$$\frac{\partial \boldsymbol{E}_{tot}(\boldsymbol{r},t)}{\partial t} = \frac{1}{\epsilon_{eff}(\boldsymbol{r})}[\nabla \times \boldsymbol{H}_{tot}(\boldsymbol{r},t) - \boldsymbol{J}_{tot}(\boldsymbol{r},t)] \tag{5.4}$$

$$\frac{\partial \boldsymbol{H}_{tot}(\boldsymbol{r},t)}{\partial t} = -\frac{1}{\mu_0}\nabla \times \boldsymbol{E}_{tot}(\boldsymbol{r},t) \tag{5.5}$$

The plasmonic current is calculated as (Ref. [146])

$$\frac{\partial \boldsymbol{J}_p(\boldsymbol{r},t)}{\partial t} = \alpha(\boldsymbol{r})\boldsymbol{J}_p(\boldsymbol{r},t) + \beta(\boldsymbol{r})\boldsymbol{E}_{tot}(\boldsymbol{r},t) \tag{5.6}$$

where, as usual, the metal susceptibility function, ϵ_{eff}, α, and β are defined according to

$$\epsilon_{eff}(\boldsymbol{r}) = \epsilon_0\epsilon_{r,\infty}(\boldsymbol{r}), \tag{5.7}$$

$$\alpha(\boldsymbol{r}) = -\gamma_D(\boldsymbol{r}), \tag{5.8}$$

$$\beta(\boldsymbol{r}) = \epsilon_0[\omega_D(\boldsymbol{r})]^2 \tag{5.9}$$

$\epsilon_{r,\infty}(\boldsymbol{r})$, $\gamma_D(\boldsymbol{r})$, and ω_D are the Drude asymptotic relative permittivity, damping constant, and plasma frequency, respectively. The parameters are material dependent, and fitted to experimental values [146, 147, 149] (parameters used in the simulations were taken from Ref. [149]).

The plasmonic fields are evolved in time by the Maxwell equations:

$$\frac{\partial \boldsymbol{E}_p}{\partial t} = \frac{1}{\epsilon_{eff}} \nabla \times \boldsymbol{H}_p + \left(\frac{1}{\epsilon_{eff}} - \frac{1}{\epsilon_0} \right) \nabla \times \boldsymbol{H}_m - \frac{1}{\epsilon_{eff}} \boldsymbol{J}_p \tag{5.10}$$

$$\frac{\partial \boldsymbol{H}_p}{\partial t} = -\frac{1}{\mu_0} \nabla \times \boldsymbol{E}_p \tag{5.11}$$

Note that Eq. (5.10) has a contribution from the molecular magnetic field, unlike Eq. (5.11). This is because the plasmons electric field is the difference of the total and molecular components, and each of these is affected by a different susceptibility, leading to the term from the molecular magnetic field. As the magnetic susceptibility is assumed constant between the plasmons and the surrounding air, no such term exists for Eq. (5.11), which is therefore much simpler. The full derivation can be found in Ref. [144]. The last ingredient is the molecular current, which is derived below from the quantum mechanical density matrix.

5.2.2 Quantum mechanical treatment

To model the contribution of the molecule, we employ the TDPM3 method [45]. TDPM3 is a semiempirical time-dependent method which greatly reduces the computational cost of modeling the molecule. TDPM3 gains efficiency in several ways. First, it treats the inner shell electrons of an atom and the nucleus as a fixed core, and thus only explicitly treats the valence electrons. Second, the

PM3 Hamiltonian is defined in terms of parameterized variables, optimized to fit experimental data:

$$H_{\mu\mu} = U_{\mu\mu} + \sum_{B} V_{\mu\mu,B} \tag{5.12}$$

$$H_{\mu\nu} = \sum_{B} V_{\mu\nu,B} \tag{5.13}$$

$$H_{\mu\lambda} = \frac{1}{2}(\beta_{\mu}^{A} + \beta_{\lambda}^{B})S_{\mu\lambda} \tag{5.14}$$

Here, $U_{\mu\mu}$ corresponds to the sum of the kinetic energy of the electron in orbital μ and the potential energy resulting from the attraction of the electron in orbital μ and the core of the atom on which that orbital is located. $V_{\mu\nu,B}$ corresponds to the attraction of an electron in atom A to the core of atom B. The β values are parameters specific to the orbital type and atom. These parameters are typically fitted to spectroscopic data. Finally, $S_{\mu\lambda}$ is an element of the overlap matrix. The β terms are used to describe the group state of a molecule.

Note that no image potential is used on the metal; formally, it will be required in a static or near static treatment, where the metals reflectivity effect manifests itself as an image charge. However, we are interested at higher frequencies, where the metal is no longer a purely reflecting substance and instead its properties are explicitly accounted for by the Maxwell equation and the frequency dependent susceptibility.

The electric field is included by a usual dipole moment, as we ignore the effect of the magnetic field on the molecule:

$$H_{ij} = H_{0,ij} + \boldsymbol{E}_p \cdot \boldsymbol{d}_{ij} \tag{5.15}$$

H_{ij} is a matrix element of the corrected, excited state Hamiltonian, $H_{0,ij}$ is the

corresponding matrix element of the ground state Hamiltonian described above in Eqs. (5.12) – (5.14), E_p is the plasmon-induced electric field at the molecules location, and d_{ij} is the dipole matrix of the molecule. The calculations are concerned with qualitative effects so that the inherent accuracy of TDPM3, about 15%-20% for excited states of organic molecule, is quite acceptable.

The Fock matrix in PM3 calculations is composed of the Hamiltonian and 2-electron terms only, and since 3- and 4- center contributions are neglected, the method is very efficient. The 1-center α (spin-up) Fock matrix is defined as

$$\begin{aligned} F^{\alpha}_{\mu\nu} &= H_{\mu\nu} + 2P^{\alpha+\beta}_{\mu\nu}(\phi^A_\mu\phi^A_\nu, \phi^A_\mu\phi^A_\nu) \\ &\quad - P^{\alpha}_{\mu\nu}[(\phi^A_\mu\phi^A_\nu, \phi^A_\mu\phi^A_\nu) + (\phi^A_\mu\phi^A_\mu, \phi^A_\nu\phi^A_\nu)] \\ &\quad + \sum_B \sum_{\lambda,\sigma} P^{\alpha+\beta}_{\lambda\sigma}(\phi^A_\mu\phi^A_\nu, \phi^B_\mu\phi^B_\nu), \end{aligned} \tag{5.16}$$

while the 2-center matrix elements are written as

$$F^{\alpha}_{\mu\lambda} = H_{\mu\lambda} - \sum_{\mu} \sum_{\sigma} P^{\alpha}_{\nu\sigma}(\phi^A_{mu}\phi^A_{nu}, \phi^B_\lambda\phi^B_\sigma). \tag{5.17}$$

Here, P is the density matrix, and we introduced the repulsion integrals of atomic orbitals ϕ of the specified atom. These repulsion integrals are semiempirically fitted to atomic properties (see Ref. [148]). Note the inclusion of only 1- and 2-center integrals.

5.2.3 Interaction between molecule and FDTD grid

The interaction between the quantum-mechanically treated molecule and the classically treated metal nanoparticles is through the molecular current term, which is obtained from the von Neumann equation for the evolution of the density matrix:

$$\frac{dP}{dt} - i[F(P), P] - \frac{P - P_0}{\tau} \tag{5.18}$$

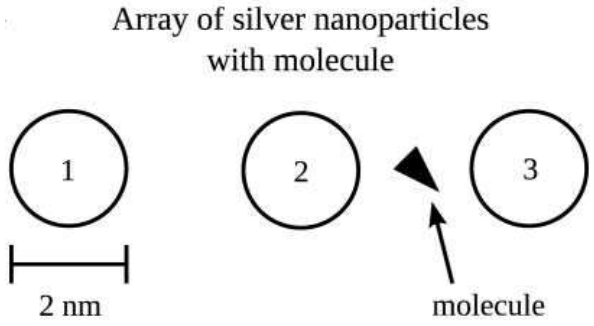

Figure 5.2: The system studied consists of three silver nanoparticles, each with a 2 nm diameter and a center-to-center distance of 4 nm. The molecule is located halfway between the second and third nanoparticles.

where F is the Fock matrix and $-(P - P_0)/\tau$ represents a phenomenological damping of the density matrix. Without this latter term, an excited molecule would only dissipate energy radiatively and would remain excited much longer than is physically reasonable.

We found that the transmitted current in Fourier space is insensitive to the value of the damping constant unless it is realistically too short (30 a.u., i.e., less than 1 fs, or lower). The reason is that almost all the transport happens on a very short time scale (the scale of transport from field to molecule and vice versa), so that the damping of the residual values of the current does not change its Fourier transform. Note that the overall dynamics takes reasonably long times (hundreds of atomic units, more than 10 fs, as presented later), but since the molecule mainly acts as a scatterer, only its short time dynamics is relevant; so there is no dependence on the damping constant.

Note that from Eq. (5.15) the Fock matrix includes the electric field. It should also be noted that the molecule and the grid act entirely through this current term, and that electrons are not actually shared between the two regimes.

The dipole moment $\boldsymbol{\mu}$ of the molecule is

$$\boldsymbol{\mu} = \sum_{ij} \boldsymbol{d}_{ij} \cdot P_{ij} \tag{5.19}$$

and the current is calculated as

$$\boldsymbol{J}_m = \frac{\partial \boldsymbol{\mu}}{\partial t} \tag{5.20}$$

The FDTD equations [Eqs. (5.4) – (5.6)] are solved simultaneously with the TDPM3 equations for the density matrix and the current [Eqs. (5.18) and (5.20)]. In practice, the evolution is done by alternating between an FDTD evolution of the electromagnetic fields and plasmonic current, and a TDPM3 evolution of the density matrix.

5.3 Results

Fig. 5.2 shows the basic setup. Plasmons are induced in the first nanoparticle (labeled 1) through adding a pulse of current (i.e., a delta function in time) as from a tip. The current is then propagated through the array via plasmon transfer as defined by the Maxwell equations, listed above in Section 5.2.1. Fig. 5.3 shows the induced current on the first nanoparticle. While a 2 nm diameter metal sphere is very small, experimentally, we chose to use such a size in our investigation, as it is sufficiently small for a single molecule that has a strong effect. We investigated systems with a more experimentally common size of 5 nm, but the effect is diminished. Future work will examine the effect of using a set of molecules rather than a single one, on larger spheres.

The molecule used is tartrazine, shown in Fig. 5.1. We chose this molecule due to its strong transition dipole moment at 3.406 eV/$\hbar$ which is very close to the plasmon frequency of silver nanoparticles, 3.397 eV/$\hbar$ (Fig. 5.4). The molecule is oriented along the negative xy-axis as indicated in Fig. 5.1.

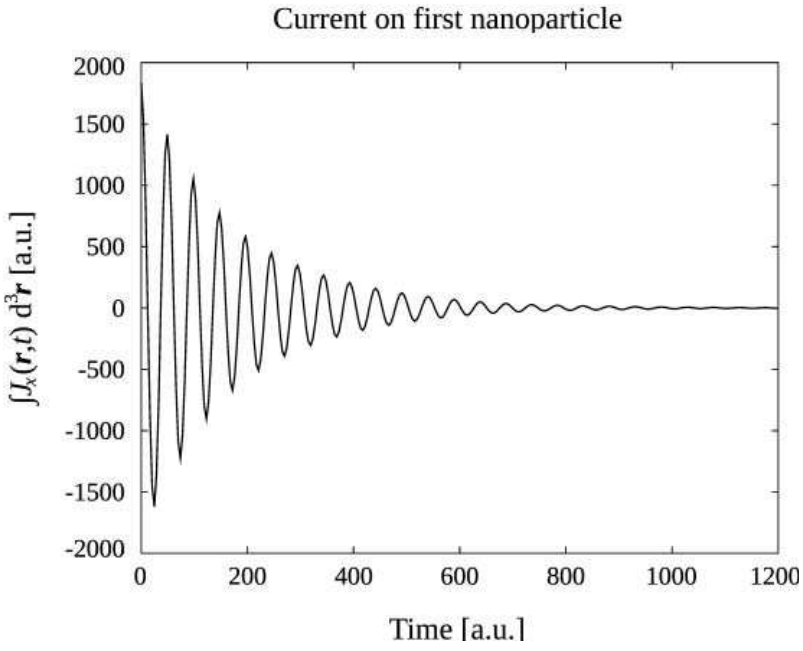

Figure 5.3: The time-resolved x-polarized current on the first nanoparticle. The current is induced on the first nanoparticle with a pulse as from a tip, and transfers to the other nanoparticles via plasmon propagation.

The simulations used are given in Eqs. (5.1) – (5.6) and Eqs. (5.10) – (5.20). The physical parameters can be found in Table 5.1 and the simulation parameters are in Table 5.2. The time-step used was 0.006 a.u., and the total grid had $150 \times 50 \times 50$ points, with a 2 a.u. grid spacing. Convergence with respect to the time-step, number of grid points, and grid spacing were confirmed.

silver	molecule
$\epsilon_{r,\infty} = 5.976$	
$\gamma_D = 9.582 \times 10^{-3}$	$\tau = 30$
$\omega_D = 0.3630$	

Table 5.1: The physical parameters for gold and for the molecule used in the simulations. All values with units are in a.u.

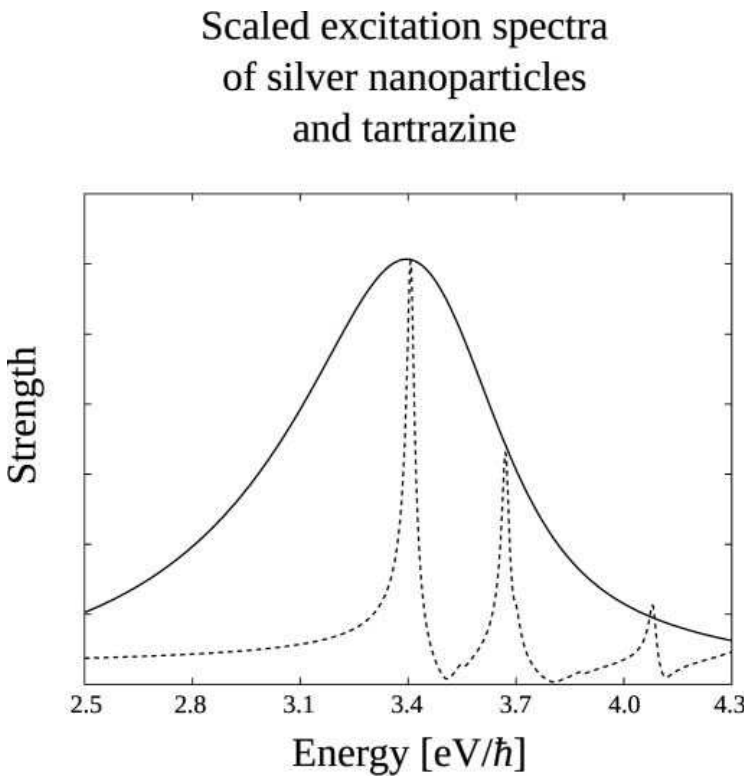

Figure 5.4: Overlap of the silver plasmon resonance (solid line) and the absorption spectrum of tartrazine (dashed line). The silver plasmon resonance curve was generated using FDTD, and the absorption spectrum of tartrazine was generated using TDPM3.

Fig. 5.5 shows the frequency resolved current on the third nanoparticle with and without the molecule. The molecule significantly reduces the current in the

grid	time
$N_x = 150$	
$N_y = 50$	$dt = 0.006$
$N_x = 50$	$t_{max} = 2024$
$dx = dx = dz = 2$	

Table 5.2: Time parameters used in simulations. All values are in a.u.

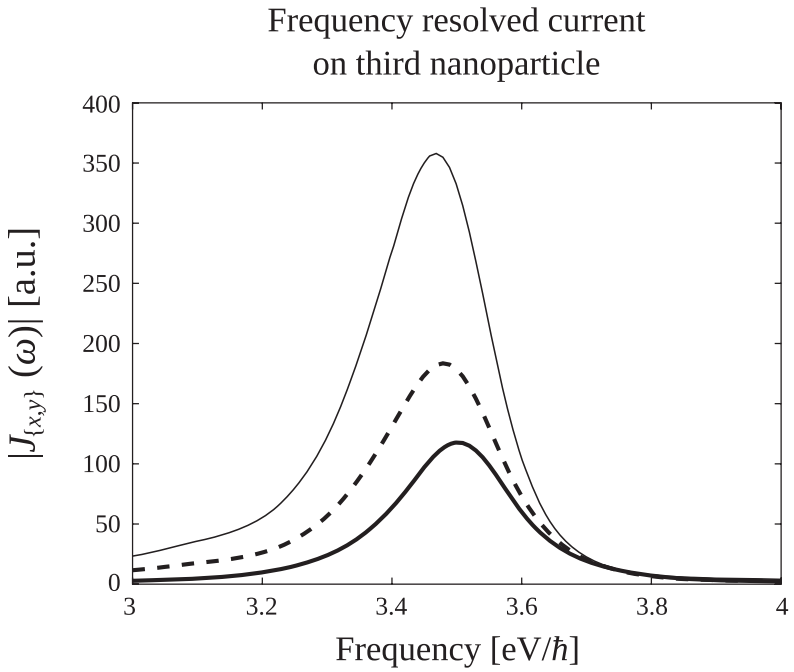

Figure 5.5: Frequency resolved current on the third nanoparticle in the x-direction (solid lines) with (bold) and without (narrow) the molecule and in the y-direction with the molecule (dashed line). The presence of the molecule rotates the x-polarized current into the y-direction, results in a y-polarized current on the third nanoparticle.

x-direction and increases the current in the y-direction.

The induced current on the molecule, shown in Fig. 5.6, effectively rotates the transferred current between the second nanoparticle and the third nanoparticle from the x-direction to the y-direction. This effect is a result of the strong transition dipole moment in tartrazine near the plasmonic frequency of silver. The molecule absorbs much of the current in the x-direction from the second nanoparticle and re-emits nearly all of the current in the y-direction.

We also investigated the effect of the molecular orientation of the molecule. Fig. 5.7 shows the frequency resolved x- and y-currents on the molecule and on the third nanoparticle for systems with the molecule oriented along the xy-axis,

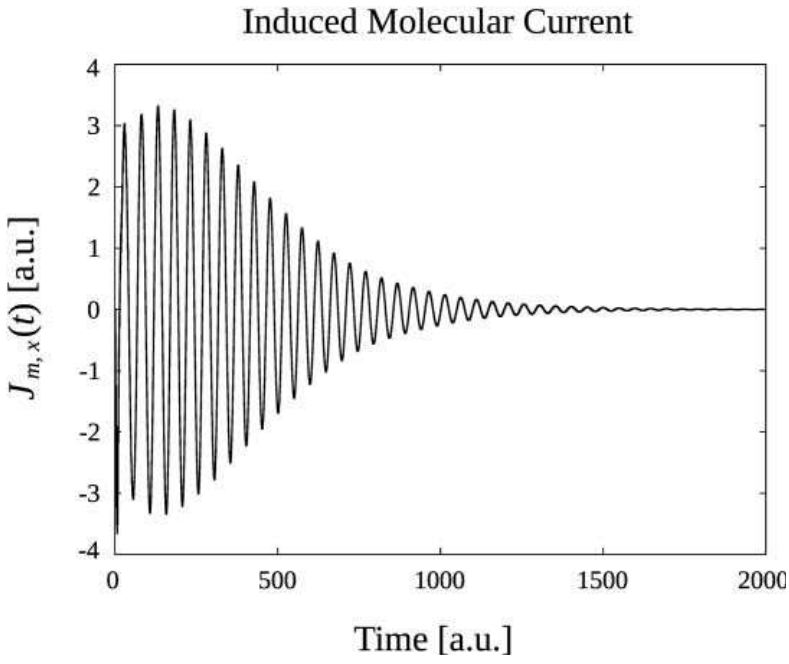

Figure 5.6: The x-polarized current on the molecule as a function of time. The y-polarized current (not shown) is slightly large than the x-polarized current.

the x-axis, and the y-axis. For a molecule oriented along the x-axis, the current on the molecule is entirely in the x-direction, and subsequently no y-oriented current is observed on the third nanoparticle. The x-polarized current in this orientation is very high, and actually results in an enhanced transfer from the second nanoparticle to the third, as shown in Fig. 5.7(e). For a y-oriented molecule, the current on the molecule is very small. The majority of the current is in the x-direction, but this current is negligible compared with the case that the molecule is oriented differently. The most interesting part is when the molecule is in the xy-direction. Then, one can either view the process as a molecule absorbing x-polarized radiation and then emitting xy-polarized current, or simply view it as a scattering process, as the molecule can only absorb and emit radiation in the xy-direction, so that the initial polarization of the light is projected to the molecular xy-direction.

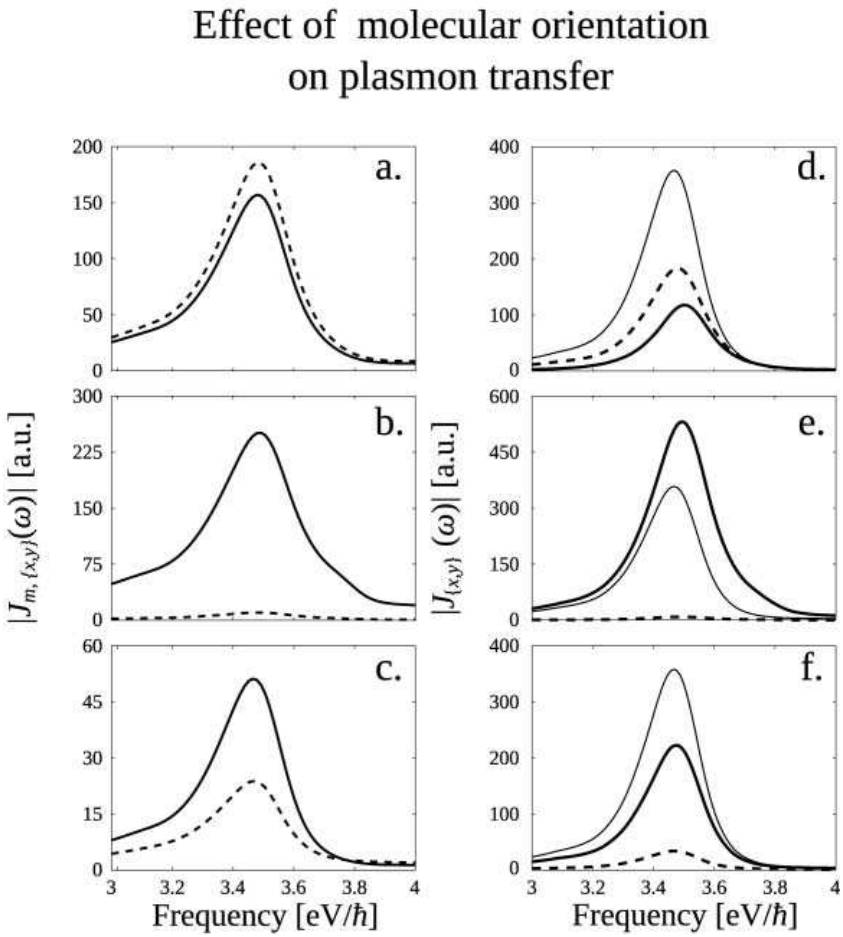

Figure 5.7: (a)-(c) The x-polarized (solid line) and y-polarized (dashed line) currents of the molecule oriented along the xy-axis, x-axis, and y-axis, respectively. (d)-(f) The frequency resolved current on the third nanoparticle for each of these orientations. The x-polarized currents are represented with a solid line, and the y-polarized currents with a dashed line. The bold lines are for simulations with a molecule, and narrow lines are for simulations without a molecule. Not the different scales on the y-axes.

Note the current on the third nanoparticle and on the molecule for the different orientations mentioned above. Specifically, when a molecule is oriented along the y-axis, very little energy is absorbed. The rotation of current in the nanoparticles

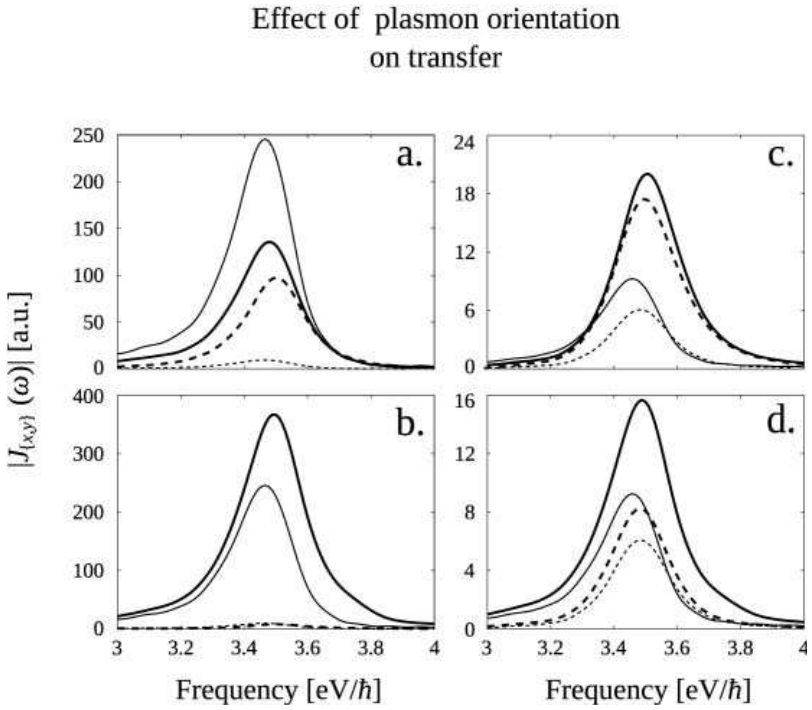

Figure 5.8: (a) and (b) The frequency resolved current on the third nanoparticle for systems in which the initial current is oriented along the xy axis for systems without the molecule (narrow lines) and with the molecules (bold line) oreiented along the xy-axis (a) and x-axis (b). The x-polarized current is shown with a solid line, and the y-current with a dashed line. (c) and (d) Systems ith an inital current in the y-direction, and a molecule oriented along the xy-axis and the x-axis. Note the different scale on the y-axis.

is not just a function of the molecules presence, but also the orientation, as it scatters the radiation.

We also investigated the effects of rotating the initial current on the first nanoparticle. In Fig. 5.8(a) and (b), we investigate systems with an initial current in the xy-direction and molecules in the xy- and x-directions, respectively. Notice that for systems without a molecule, almost no y-current is transmitted to the third nanoparticle; this is due to the fact that there is no mechanism to transmit

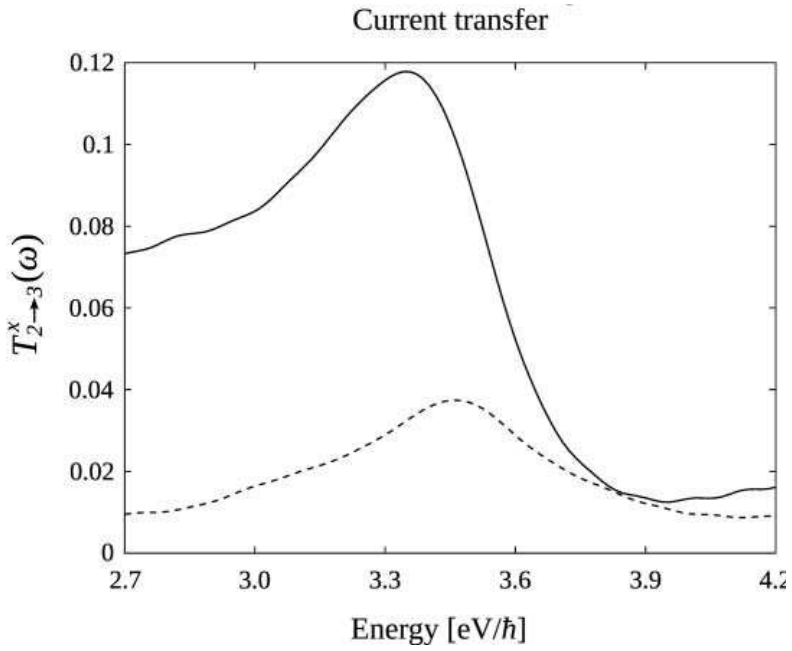

Figure 5.9: The percentage of x-polarized current transfer from the second to the third nanoparticle without (solid line) and with (dashed line) a molecule. The presence of a molecule significantly reduced x transfer.

y-current between the first and second nanoparticles. Thus, for systems with the molecule in the xy-direction, the molecule again rotates x-current into the y-direction. Likewise, the x-oriented molecule enhances the transmission of x-current, but has no effect on the y-current. For systems where the current is introduced in the y-direction, very little current reaches the third nanoparticle. In these cases, we observe similar behavior as before: the xy-oriented molecule rotates some current into the x-direction, and the x-oriented molecule enhances the transfer in the x-direction.

The molecule also has a strong effect on the energy transfer between the second and third nanoparticles. The transfer of the x-polarized current is defined as

$$T(\omega) = \left| \frac{J_{x,3}(\omega)}{J_{x,2}(\omega)} \right| \tag{5.21}$$

Fig. 5.9 shows the energy transfer between the second and third nanoparticles for system with and without a molecule around the absorption band of tartrazine and silver. The graph indicates the large decrease in energy transfer, about 65%, at and around the silver plasmon resonance in the presence of the molecule.

Comparing to previous work on a two-level molecular system (Ref. [144]), we note several differences.

Percentage-wise, tartrazine has a stronger effect on the current on the third nanoparticle than does the two-level molecule, where the overall current changes by as much as 35%. However, the shape of the curve changes less strongly here: tartrazine results in a reduction of current transfer less sharply pronounced around the excitation energy of the molecule. We attribute this difference to several factors. Mainly, tartrazine does not have as sharp an absorbance as the two-level molecule. Also, Fig. 5.4 shows that tartrazine has several excitation modes at or near silvers plasmon frequency. This leads to differences in absorption and re-emission.

These main differences arise from the fact that the properties of the two-level molecule were tunable, i.e., we were able to set the excitation frequency and more importantly the extinction coefficient. In contrast, the properties of tartrazine are determined by the physics of the molecule itself.

Finally, recall that the absorption of tartrazine in this work is determined by the minimum basis TDPM3 method. While the TDPM3-generated absorption spectrum is qualitatively similar to the experimentally generated absorption spectrum, the differences could change the effects on current transmission between the nanoparticles (see Fig. 5.10 for an overlay of TDPM3-generated and experimentally generated spectra; experimental spectrum is taken from Ref. [150]).

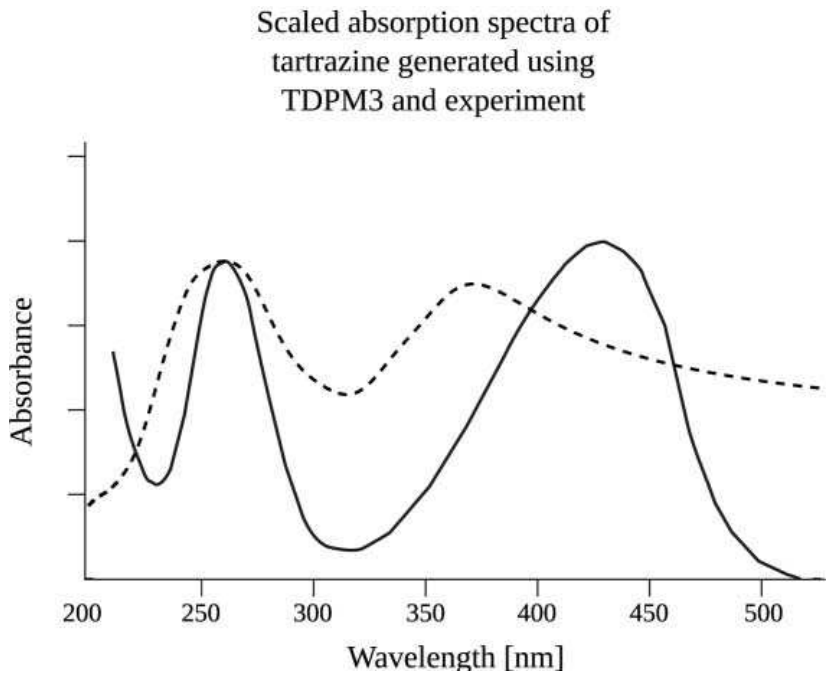

Figure 5.10: Overlay of the TDPM3-generated (dashed line) and experimentally generated (solid line) absorbance spectra of tartrazine.

5.4 Conclusions

To conclude, we show the strong effect of a single molecule can have on the transmission of current and energy between neighboring nanoparticles.

The presence of tartrazine results in a large decrease in the x-polarized current on the third nanoparticle. This current is rotated into the y-direction, and we observe y-polarized current on the third nanoparticle where none is found without the molecule. This effect can potentially have a multitude of applications in the areas of sensing and molecular switches. The enhancement of y-polarized current is sufficient so that devices sensitive enough to detect a single molecule could be conceived.

There are several directions for future research, such as enhancing the effect of a single molecule. This could be achieved with an alternate, more strongly

absorbing molecule or by a varied geometry. Another direction could be including more molecules, which could greatly enhance y-polarized current on the third nanoparticle or cause a resonant effect between the molecules.

The present work is a multiscale approach to model the interaction between molecules and metal surfaces. The method allows a simultaneous treatment of a quantum mechanical molecule interacting with a classical metal cluster. This combined approach allows for an accurate treatment of the respective components in the system without sacrificing efficiency.

The approach developed here is general. Because the interface between the classical FDTD routine and the TDPM3 routine does not depend on either specifically, other methods could be substituted. For example, the model could easily account for the introduction of TDDFT as an alternative to TDPM3. In addition, the fact that the metals are described by just a few parameters, substitution of any metal for which the necessary experimental data is available is possible.

An extension of the present work will be the modeling of complex moleculemetal surface interactions. A future direction would be a more sophisticated interface between the molecule(s) and metal.

CHAPTER 6

Near-field finite-difference time-domain method for simulation of electrodynamics on small scales

6.1 Introduction

The finite-difference time-dependent method (FDTD, also labeled here as Maxwells FDTD) is one of the main methods for quantitative simulations of electromagnetic systems [146,147,151–153] (alternatives include, e.g., the discrete dipole approximation (DDA) [154–156], plasmon hybridization [157], and frequency-domain approaches [158,159]). Recently, there have been much efforts directed at merging Maxwells FDTD with the time-dependent Schrödinger (or alternatively Heisenberg or Bloch) equations for describing near-field dynamics and the effects on or of molecules (see e.g., Ref. [160]). A difficulty in these simulations, however, is the tiny time step required in FDTD. Here, we show how to circumvent the time step difficulty for small structures (below 50 nm).

In Maxwell's FDTD, the time step dt needs to be smaller than $dx/(\sqrt{3}c)$, where dx is the minimal grid spacing and c is the velocity of light, $\sim$137 a.u. For example, for near field (NF) structures where the features are as small as 0.1 nm, $dt \sim 0.008$ a.u = 0.2 attoseconds. This is a tiny step when considering that in real-time electronic dynamics dt can be as big as $\sim$1 a.u.

A simple solution is to realize that in the near-field world, where the structures are much smaller than the wavelength, the electric field is mostly unrelated to the velocity of light; instead, the dominant component of the electric field is longitu-

dinal, i.e., the quasistatic gradient of the Coulomb integral over the instantaneous charge distribution:

$$\boldsymbol{E}_{\text{near-field}}(\boldsymbol{r},t) = -\frac{\nabla}{4\pi\epsilon_0}\int \frac{\rho(\boldsymbol{r}',t)}{|\boldsymbol{r}-\boldsymbol{r}'|}d^3\boldsymbol{r}' \tag{6.1}$$

We therefore propose here to propagate only the time-dependent density and currents (see precise definitions later), and to assume that the electric field is longitudinal. The relation between electric fields and currents remains, however, exactly as in Maxwell's FDTD so that the crucial frequency dependence of the permittivity, $\epsilon(\boldsymbol{r},\omega)$, is fully captured. The overall approach is therefore labeled NF. NF is simply the time dependent version of the usual frequency dependent Poisson approach (see, e.g., Ref. [159]).

For the evolution of NF in time, we develop here a leapfrog approach, analogous to Yee's method for Maxwell's FDTD. As we show, a very large time step is feasible in NF (2.5 a.u., $\sim$ 300 times bigger than the minimum time step in FDTD for small features) at a price of a convolution (Coulomb integral) each time step.

Note that as a matter of semantics we use the term NF rather than quasistatic. The latter term could be misleading as the frequencies involved here are as high as in any FDTD simulations (up to 6 eV in our simulations); the NF label only implies that the length scales are much smaller than the wavelength of the light. Also, formally NF is also a finite-difference time-dependent method, but for brevity we often label it just as NF.

Finally, we develop here a new and very accurate, 8- and 9-oscillator fit (containing a total of 24-27 terms) to the permittivity of gold and silver. The fit yields very closely the experimental values between near IR and UV. The main feature in the new fit is that all damping constants (explained below) are not overly large, so the fit can be used with the large time steps allowed in NF.

The remainder of the paper is developed as follows. The method is explained

in detail in Section 6.2, the fit is examined in Section 6.3, and Section 6.4 shows absorption profiles for both single spheres and dimers; the results are favorably compared to Mie theory (for single spheres) and numerical Maxwell's FDTD simulations (metal dimers). Discussion and conclusions follow in Section 6.5.

6.2 Methodology

6.2.1 Overall equations

For each material the permittivity is represented as a sum of Drude oscillators:

$$\epsilon(\omega) = \epsilon_\infty + \epsilon_0 \sum_{j=1}^{N_j} \frac{\beta_j}{\overline{\omega}_j^2 - i\alpha_j\omega - \omega^2} \tag{6.2}$$

where α_j, $\overline{\omega}_j$, β_j are (real) material-dependent paramters: most studies use N_j $\sim$ 2-4 Lorentzians (i.e., Drude-oscillators) (see e.g., Ref. [161] and references therein), but as mentioned, here we apply 8-9 Lorentzians to give an excellent fit over a wide frequency range. Further, the first version developed here requires a spatially constant ϵ_∞ (here we use $\epsilon_\infty = \epsilon_0$); the next version will relax this requirement, as explained in the conclusions. Eq. (6.2) is natural for metals, so in this first paper we only simulate metals + vacuum.

We aim for an overall time-dependent density which fulfills the continuity equation,

$$\frac{\partial \rho}{\partial t} = -\nabla \cdot \boldsymbol{J} \tag{6.3}$$

such that the permittivity will be associated with an overall polarization which fulfills the Poisson equation

$$\nabla \cdot (\epsilon(\boldsymbol{r}, \omega)\tilde{\boldsymbol{E}}(\boldsymbol{r}, \omega)) = 0 \tag{6.4}$$

where the Poisson equation vanishes since the density is due to the polarization in the metal, and there are no free charges in this version (they could be straightforwardly added). Also $\tilde{\boldsymbol{E}}$) referes to the field in frequency space. The frequency-dependent Poisson equation and the continuity equation are both fulfulled if we define currents and polarizations $\boldsymbol{J}_j(\boldsymbol{r},t)$, $\boldsymbol{P}_j(\boldsymbol{r},t)$, which are evolved as follows:

$$\frac{\partial \boldsymbol{P}_j(\boldsymbol{r},t)}{\partial t} = \boldsymbol{J}_j(\boldsymbol{r},t) \tag{6.5}$$

$$\frac{\partial \boldsymbol{J}_j(\boldsymbol{r},t)}{\partial t} = -\alpha_j(\boldsymbol{r})\boldsymbol{J}_j(\boldsymbol{r},t) - \overline{\omega}^2(\boldsymbol{r})\boldsymbol{P}_j(\boldsymbol{r},t) + \epsilon_0\beta_j(\boldsymbol{r})\boldsymbol{E}(\boldsymbol{r},t) \tag{6.6}$$

such that the total current and polarization are

$$\begin{aligned} \boldsymbol{J}(\boldsymbol{r},t) &= \sum_j \boldsymbol{J}_j(\boldsymbol{r},t) \\ \boldsymbol{P}(\boldsymbol{r},t) &= \sum_j \boldsymbol{P}_j(\boldsymbol{r},t) \end{aligned} \tag{6.7}$$

Equations Eqs. (6.5) – (6.7) give the the usual relation between the current and the electric field, i.e., when transforming from time to frequency, then at each point in space

$$\begin{aligned} \tilde{\boldsymbol{J}}(\boldsymbol{r},\omega) &= -i\omega(\epsilon(\boldsymbol{r},\omega) - \epsilon_0)\tilde{\boldsymbol{E}}(\boldsymbol{r},\omega) \\ \tilde{\boldsymbol{P}}(\boldsymbol{r},\omega) &= (\epsilon(\boldsymbol{r},\omega) - \epsilon_0)\tilde{\boldsymbol{E}}(\boldsymbol{r},\omega) \end{aligned}$$

The total density is

$$\rho = -\nabla \cdot \boldsymbol{P} \tag{6.8}$$

and the potential is obtained from the density by a convoluation:

$$\phi(\boldsymbol{r},t) = \frac{1}{4\phi\epsilon_0}\int \frac{\rho(\boldsymbol{r}',t)}{|\boldsymbol{r}-\boldsymbol{r}'|}d^3\boldsymbol{r}' \tag{6.9}$$

(The numerical approach for calculating the convolution integral is discussed later.) The total field is made from any external fields applied as well as the contribution of the potential, i.e.,

$$\boldsymbol{E}(\boldsymbol{r},t) = -\nabla\phi(\boldsymbol{r},t) + \boldsymbol{E}_{ext}(t) \tag{6.10}$$

A proof that this description yields the correct frequency-dependent Poisson equation is straightforward and presented later. Note that Eq. (6.3) and Eqs. (6.9) and (6.10) also yield

$$\frac{\partial\boldsymbol{E} - \boldsymbol{E}_{ext}}{\partial t} + \frac{\boldsymbol{J}_T}{\epsilon_0} = 0$$

where

$$\boldsymbol{J}_T = \frac{1}{\nabla^2}\nabla\nabla\cdot\boldsymbol{J}$$

i.e., Eq. (6.3) and Eqs. (6.9) and (6.10) are equivalent to the Maxwell equation, except that the curl of the magnetic field is neglected.

Finally, note that the electric field is not propagated independently; only the currents and polarizations are integrated forward in time, as shown below.

6.2.2 Leapfrog propagation

Eqs. (6.5) and (6.6) are simplest to propagate forward in time in a leapfrog fashion; i.e., the currents $\boldsymbol{J}_j(\boldsymbol{r},t)$ are stored at times $dt/2$, $dt+dt/2$, $2dt+dt/2$, ... , while the polarizations $\boldsymbol{P}_j(\boldsymbol{r},t)$ are stored at 0, dt, dt, ...

The discretization of the evolution equation for the current is then

$$\frac{\boldsymbol{J}_j(\boldsymbol{r}, t+\frac{1}{2}dt) - \boldsymbol{J}_j(\boldsymbol{r}, t-\frac{1}{2}dt)}{dt} = -\alpha_j(\boldsymbol{r})\frac{\boldsymbol{J}_j(\boldsymbol{r}, t+\frac{1}{2}dt) + \boldsymbol{J}_j(\boldsymbol{r}, t-\frac{1}{2}dt)}{2} - \overline{\omega}^2(\boldsymbol{r})\boldsymbol{P}_j(\boldsymbol{r}, t) + \epsilon_0\beta_j(\boldsymbol{r})\boldsymbol{E}(\boldsymbol{r}, t) \tag{6.11}$$

so that the evolution equation for the current is

$$\boldsymbol{J}_j\left(\boldsymbol{r}, t+\frac{dt}{2}\right) = \frac{1-\frac{\alpha_j(\boldsymbol{r})}{2}}{1+\frac{\alpha_j(\boldsymbol{r})}{2}}\boldsymbol{J}_j\left(\boldsymbol{r}, t-\frac{dt}{2}\right) - \frac{dt}{1+\frac{\alpha_j(\boldsymbol{r})}{2}}(\overline{\omega}^2(\boldsymbol{r})\boldsymbol{P}_j(\boldsymbol{r}, t) - \epsilon_0\beta_j(\boldsymbol{r})\boldsymbol{E}(\boldsymbol{r}, t)) \tag{6.12}$$

The evolution of the polarization is even simpler:

$$\boldsymbol{P}_j(t+dt) = \boldsymbol{P}_j(t) + dtJ_j\left(t+\frac{dt}{2}\right) \tag{6.13}$$

The initial conditions for the evolution are then

$$\begin{aligned} \boldsymbol{J}_j\left(t=-\frac{dt}{2}\right) &= 0, \\ \boldsymbol{P}_j(t=0) &= 0, \\ \boldsymbol{E}_{ext}(\boldsymbol{r}, t=m\ dt) &= f(t=m\ dt)\boldsymbol{E}_0, \end{aligned} \tag{6.14}$$

where $\boldsymbol{E}_0$ is the spatial profile of the external field (either uniform or concentrated in a given area); we chose a delta-function pulse for the time-dependent external field, i.e.,

$$f(t=m\ dt) = \begin{cases} 0, & m>0 \\ \frac{1}{dt}, & m=0 \end{cases} \tag{6.15}$$

but other choices, such as a step function, could have also been used.

In algorithmic form, the resulting formalism is straightforward:

Start with $\boldsymbol{J}_j = \boldsymbol{P}_j = 0$. Then, at each step:

- First calculate the density, potential, and electric field
- Then, update the current (Eq. (6.12))
- Finally, update the polarization (Eq. (6.13))

The form of NF shoudl allow for simple embedding, as discussed later.

6.2.3 Relation to frequency-space Poisson algorithm

The NF algorithm is reminiscent of two other formulations: Maxwell's FDTD, where the electric and magnetic fields are propagated rather than the polarizations, and where the current is also included; and the discrete dipole approximation.

The NF algorithm is also the time dependent version of the frequency dependent Poisson algorithm, whereby one solves

$$\nabla \cdot (\epsilon(r,\omega)\nabla\tilde{\phi}) = -\nabla \cdot (\epsilon(r,\omega)\tilde{E}_{ext}(r,\omega)) \tag{6.16}$$

(i.e., the same as Eq. (6.4), with $\boldsymbol{E} = \boldsymbol{E}_{ext} - \nabla\phi$, and $\boldsymbol{E}_{ext}$ is the external field). The proof relies on the fact that the density and potential are related, from the potential's definition, by the usual Coulomb potential, so that, in frequency space,

$$\begin{aligned}
\nabla \cdot (\epsilon(\boldsymbol{r},\omega)\tilde{\boldsymbol{E}}(\boldsymbol{r},\omega)) &= \nabla \cdot ((\epsilon(\boldsymbol{r},\omega) - \epsilon_0)\tilde{\boldsymbol{E}}(\boldsymbol{r},\omega)) \\
&\quad + \epsilon_0 \nabla \cdot (\tilde{\boldsymbol{E}}(\boldsymbol{r},\omega) - \tilde{\boldsymbol{E}}_e xt) + \epsilon_0 \nabla \cdot (\tilde{\boldsymbol{E}}_{ext}) \\
&= \nabla \cdot (\tilde{\boldsymbol{P}}(\boldsymbol{r},\omega)) - \epsilon_0 \nabla^2 \tilde{\phi}(\boldsymbol{r},\omega) + \epsilon_0 \nabla \cdot (\tilde{\boldsymbol{E}}_{ext}) \\
&= -\tilde{\phi}(\boldsymbol{r},\omega) + \tilde{\rho}(\boldsymbol{r},\omega) + \epsilon_0 \nabla \cdot (\tilde{\boldsymbol{E}}_{ext})
\end{aligned} \tag{6.17}$$

and if the external field is constant in space, the last term vanishes.

6.2.4 The convolution integral

A remaining issue is how to calculate the convolution integral. Here, we adopt the simplest approach, i.e., using a spatial Fourier transform; specifically, we write

$$\begin{aligned} \rho(r) &\rightarrow \tilde{\rho}(k) \\ \tilde{\phi}(k) &= \frac{4\pi}{k^2}\tilde{\rho}(k) \\ \tilde{\phi}(k) &\rightarrow \phi(r) \end{aligned}$$

For consistency, we also could use a similar approach when calculating the divergence of the polarization field, although we found in practice that the results are quite similar when a few-point formula is used for the calculation of the divergence.

There are many possible variations on this theme; for example, wrap-around effects can be accounted for by modifying the $4\pi/k^2$ coefficients; or the Poisson equation ($-\nabla^2\phi = \rho/\epsilon_0$) could be solved explicitly by iterations; these variants will be explored in future work.

6.2.5 Extinction cross section

The extinction cross section is calculated by the usual formulae from the polarization or current. Specifically, we use homogenous external field profile $\boldsymbol{E}_0\delta(t)$, which has a uniform frequency distribution ($\boldsymbol{E}_{ext}(\boldsymbol{r},\omega) = \boldsymbol{E}_0 = const.$) and get

$$\begin{aligned} C_{ext} &= \frac{4\pi\omega}{c|\boldsymbol{E}_0|^2}\mathrm{Im}\left[\int \boldsymbol{P}(\boldsymbol{r},\omega)d\boldsymbol{r}\right]\cdot\boldsymbol{E}_0 \\ &= \frac{4\pi\omega}{c|\boldsymbol{E}_0|^2}\mathrm{Re}\left[\int \boldsymbol{J}(\boldsymbol{r},\omega)d\boldsymbol{r}\right]\cdot\boldsymbol{E}_0 \end{aligned} \tag{6.18}$$

where the Fourier transform has a unit overall coefficient, i.e.,

$$\boldsymbol{J}(\boldsymbol{r},\omega)=\int_{-\infty}^{\infty}\boldsymbol{J}(\boldsymbol{r},t)e^{-i\omega t}dt$$

Therefore, we just need, as usual, to calculate the total spatial current, integrate it over time, and Fourier transform to frequency space.

As a reminder, the presence of the velocity of light in this quasistatic expression is due to the definition of the extinction coefficient as the ratio of the energy-dissipation rate and the incoming flux, as the latter is proportional to c.

6.3 Fitting the permittivity of gold and silver

The parameters in the fit, α_j, $\overline{\omega}_j$, β_j, have a clear physical meaning from Eq. (6.2), as well known from textbooks and previous work. For each local "oscillator" j, α_j is the damping, ω_j is the restoring frequency of the oscillator, and β_j (taken here as either positive or negative) is the contribution to the overall permittivity.

Here, we fitted the permittivity of gold and silver, over a wide frequency range (for gold 0.6-6.7 eV, the range of data for Johnson and Christy [1]). As mentioned above, there are several fits in the literature over narrower ranges, as well as a four-Lorentzians fit over the same range we covered (see Ref. [161] and references therein); these fits, however, have a wider range of values of the parameters. Here, a very large time step is used (2.5 a.u.); with such large time-steps, the damping constants α_j and oscillator frequencies cannot be too large, so, as mentioned, a refit is necessary.

The fit was done by standard methods. An objective is defined:

$$\begin{aligned}I\{\alpha_j,\overline{\omega}_j\}=\mathrm{Min}_{\{\beta_j\}}\Bigg[\frac{1}{\mathrm{eV}}\int g(\omega)\Big(&\mathrm{Re}\left[\epsilon(\omega)-\epsilon_{exp}(\omega)\right]^2\\&+C\mathrm{Im}\left[\epsilon(\omega)-\epsilon_{exp}(\omega)\right]^2\Big)d\omega+\frac{10^{-5}}{(\mathrm{eV})^2}\sum_j\beta_j^2\Bigg]\end{aligned}\tag{6.19}$$

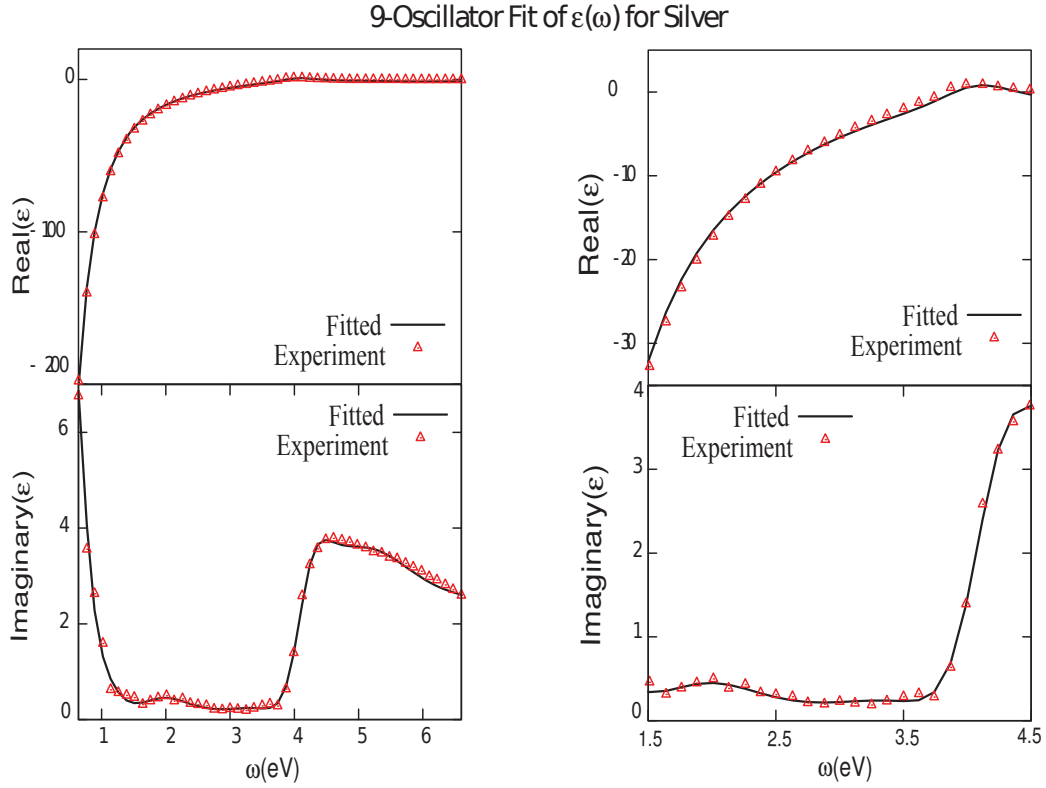

Figure 6.1: Comparison of the fitted permittivity of silver: The Johnson-Christy data (triangles) vs. the new fit. The upper and lower panels show the real and imaginary parts. The left side shows the fit over the a large range, and the right side zooms to a smaller frequency reange, 1.5-4.4 eV.

For each value of the set of parameters, $\{\alpha_j, \overline{\omega}_j\}$ the optimal coefficients $\{\beta_j\}$ are found analytically by differentiation of the two terms in the right-hand side of Eq. (6.19) since the objective is bilinear in the coefficients, β_j. The objective functional with the optimal coefficients was minimized with respect to the non-linear parameters, $\{\alpha_j, \omega_j\}$, by a steepest descent algorithm, with the damping and restoring frequencies allowed to vary only in a restricted range,

$$0.1 \text{ eV} < \alpha_j < 2 \text{ eV}$$

$$0.001 \text{ eV} < \overline{\omega}_j < 12 \text{ eV}$$

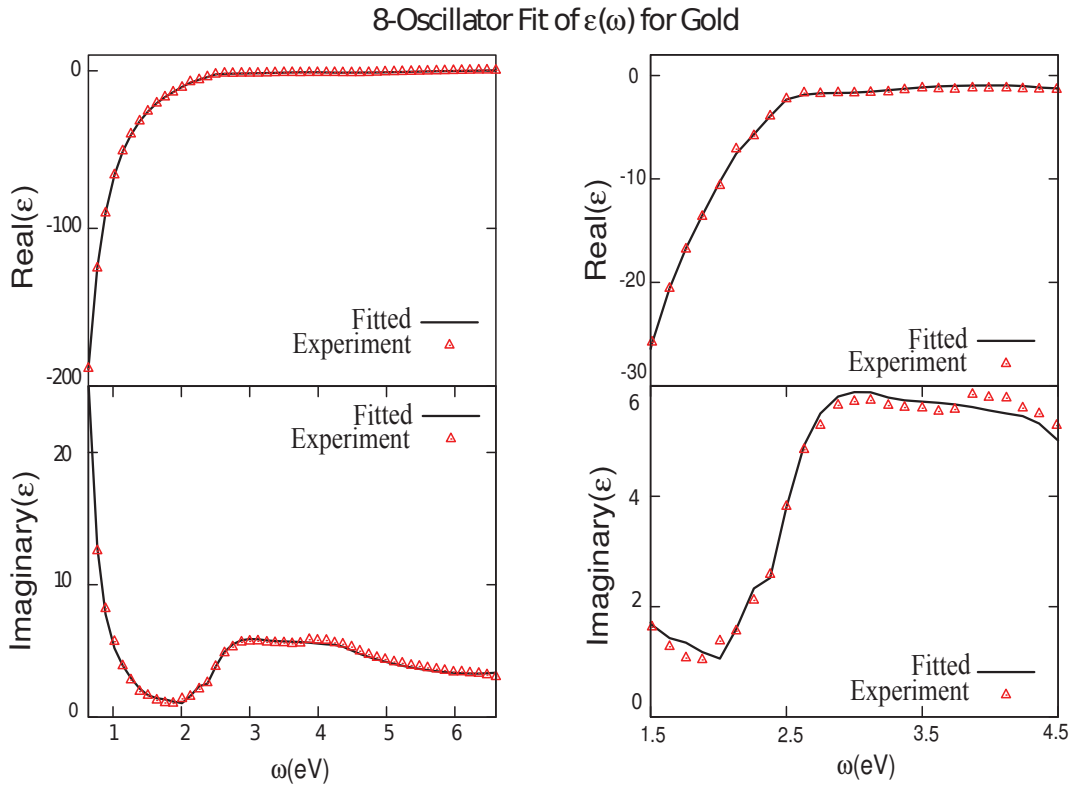

Figure 6.2: Similar to Fig. 6.1, for gold, using 8 Lorentzians.

and we chose a weight function which will de-emphasize the lower frequency part where the permittivity is larger but has less structure: $g(\omega) = \frac{\omega^2}{\omega^2 + (1\text{ eV})^2)}$.

Note that since the coefficients $\{\beta_j\}$ are real we could treat the real and imaginary part in the objective independently; therefore, for the best fit we have set the coefficient of the imaginary part as $C = 10$.

Table 6.1 and Table 6.2 show the fit parameters. Fig. (6.1) and (6.2) show the quality of the fit over the Johnson and Christy range. As shown the fit is very accurate. Of course, in many simulations a lower quality fit (or the one tailored to a smaller specific region of frequencies) will suffice, so fewer terms could be used. A similar fit could have been applied to other metals; dielectrics would be more challenging, as mentioned.

Since the goal of the fit was numerical, we should be careful with allocating

specific features in the permittivity (with their origin in inter- or intra-band transitions) to specific terms in the fit. However, we could tentatively relate some of the features of the permittivity to specific terms, for example, the features around 3 and 4 eV for gold or 4-5 eV for silver, where the permittivity changes rapidly.

$\overline{\omega}_j$ (eV)	α_j (eV)	β_j (eV)^2
0.2350	0.1551	95.62
0.4411	0.1480	-12.55
0.7603	1.946	-40.89
0.161	1.396	17.22
2.946	1.183	15.76
4.161	1.964	36.63
5.747	1.958	22.55
7.912	1.361	81.04

Table 6.1: Fitting parameters for gold.

$\overline{\omega}_j$ (eV)	α_j (eV)	β_j (eV)^2
0.1696	0.1795	135.0
0.3655	0.2502	-40.30
0.6312	2.114	-50.06
1.175	1.627	16.73
20.77	1.820	7.651
4.018	1.049	-15.36
4.243	0.9967	18.07
5.303	2.592	40.42
7.197	2.774	31.02

Table 6.2: Fitting parameters for silver.

6.4 Results

To test NF we studied two types of systems: first, a single uniform gold or silver sphere; then, two uniform gold and silver spheres of 10 nm diameter as a function of the distance between them.

Most dimer simulations below included a grid of $64 \times 32 \times 32$ points, with the grid spacing about 1/10th of the sphere radius; for single spheres, where high accuracy was required (as the results were compared to the analytical Mie theory, see below), we increased the number of grid points to 64^3 and interpolated the results to the infinite-cell limit. Future publications will investigate the overall dependence on cell length.

We first study the extinction cross section for a single sphere. We scaled the results by the sphere volume and present below the scaled extinction cross section,

$$C'_{ext} \equiv \frac{C_{ext}}{V} = \frac{C_{ext}}{\frac{\pi d^3}{6}}$$

where d is the sphere diameter.

Fig. 6.3 compares NF to the analytical solution of Maxwell's equations for a single sphere (Mie theory) for different sphere sizes. NF is formally exact in the long-wavelength limit, where the well-known extinction cross section is, from Mie theory,

$$\begin{aligned} C'_{ext} &= \frac{C_{abs} + C_{scat}}{V} \cong \frac{C_{abs}}{V} \\ &= \frac{3\omega}{c} \mathrm{Im}\left[\frac{\epsilon - 1}{\epsilon + 2}\right] (\mathrm{as} d \to 0) \end{aligned} \tag{6.20}$$

and we introduce the absorption and scattering cross section, where the latter is negligible for small spheres.

As Fig. 6.3 shows, the numerical NF simulations agree with the exact Mie-theory Maxwell results for small spheres. For small diameters ($d = 1$ nm, $d = 10$

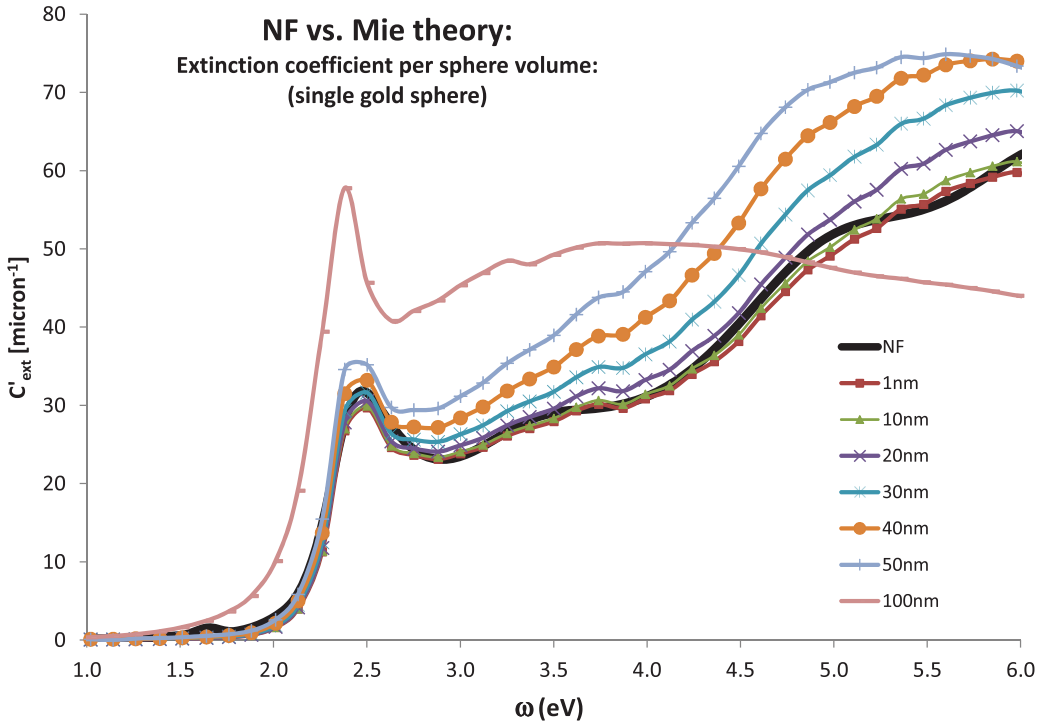

Figure 6.3: Scaled extinction coefficient ($C'_{ext} \equiv C_{ext}/C$) for small gold spheres using both Mie theory at various sizes as well as NF. The Mie theory results are calculated and marked at the experimental frequency point values taken from Johnson and Christy [1].

nm), the Mie-theory results equal to the limiting form in Eq. (6.20). The numerical NF simulations are slightly different from Eq. (6.20) due to grid-discretization and finite grid volume.

At low frequencies, where the wavelength is large, the larger-spheres Mie-theory results are reasonably similar to NF up to diameters of d $\sim$ 50 nm; at higher frequencies, good agreement is obtained until d $\sim$ 30 nm.

Fig. 6.4 shows the evolution of the spectral shape for Maxwell's FDTD vs. NF as a function of spacing for both gold and silver dimers. The external electric field polarization is parallel to the dimer axis, and we study the absorption for different dimer spacings. The agreement is quite good. The lowering of the absorption

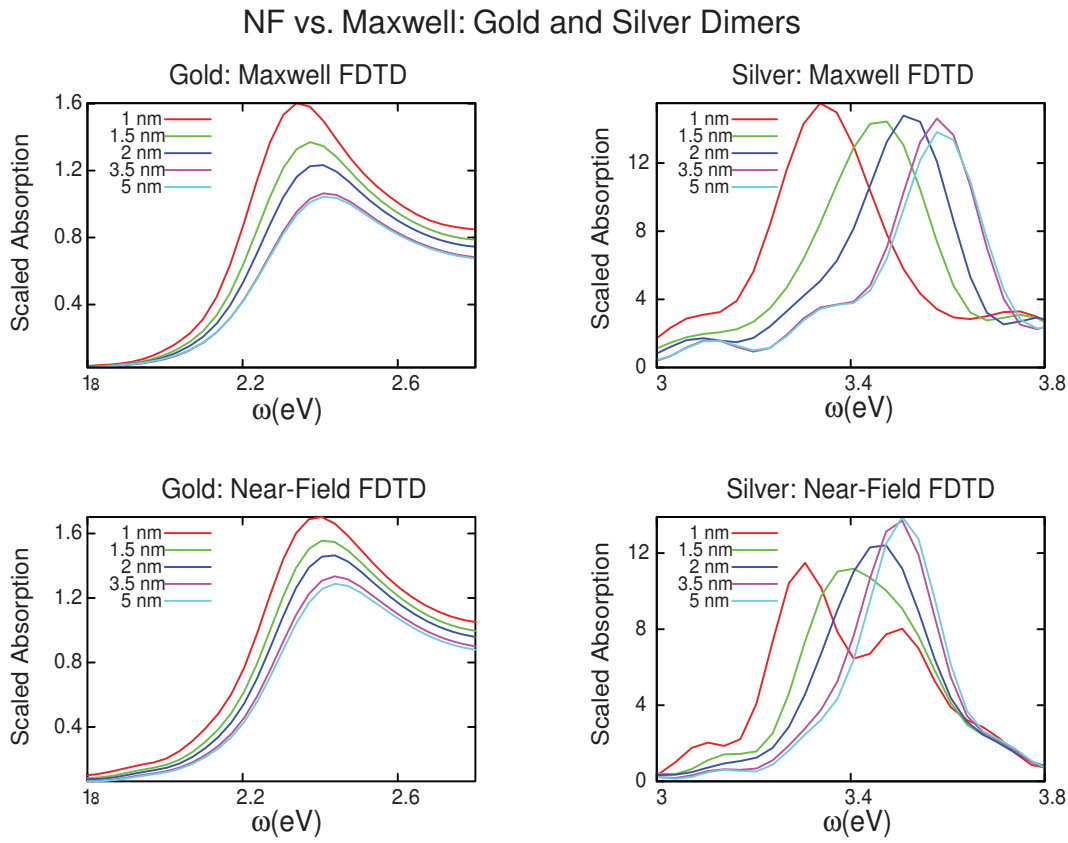

Figure 6.4: Evoluation of the spectral shape of the Maxwell FDTD (top) vs. NF (bottom) for spheres of diameter 10 nm, and an electric field parallel to the spheres. The left panels are for gold, and the right for silver. Each line refers to a different seration between two spheres. Maxwell FDTD and NF agree well, and, in particular, NF shows the redshift that is expected with the decrease in the separation between the spheres.

peak at low separations [137] (essentially due to hybridization of the plasmon modes [162]) is evident, and reproduced very similarly in both approaches. There are some differences for small inter-sphere spacings; these are mostly due to the different spatial discretization schemes. NF uses a spatial-Fourier transform to calculate the electric field potential, rather than the nearest-neighbor spatial differences in Maxwell's FDTD.

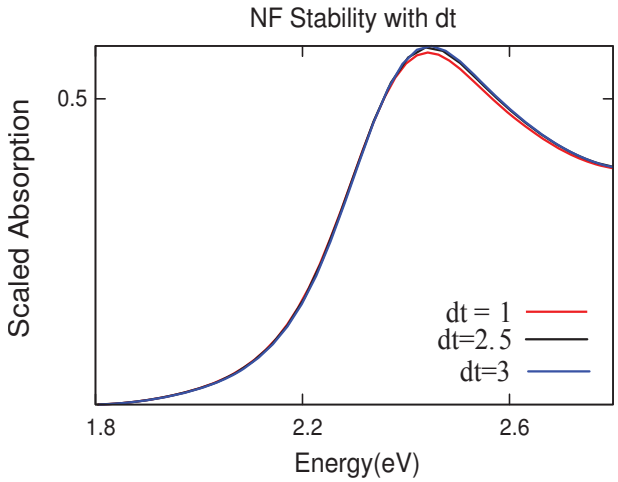

Figure 6.5: NF is stable and accurate even for large time-step, as shown by the dependence of the absorption of a single gold sphere on time step. The figure shows that even for time step of 3.0 a.u., algorithm is convergent.

Fig. 6.5 shows that the method is well converged even for large time-steps.

Finally, Fig. 6.6 compares the electric field intensities for a challenging case, two silver spheres with a minimum distance of about 1 nm. The time-dependent electric fields were Fourier transformed at a frequency of 3.26 eV, and we show the intensity of the Fourier transformed fields along a slice in the xy plane (near $z = 0$). The fields are quite similar; the differences are slightly due to the neglect of retardation effects in NF, but mostly due to the use of a different spatial discretization scheme. The intensities, which should be compared to the initial field intensity set at $|\tilde{\boldsymbol{E}}_0(\boldsymbol{r}, \omega)|^2 = 1$ are quite large, due to the well-known enhancement of fields in confined regions near metal edges.

6.5 Discussion and Conclusion

To summarize: The NF algorithm presented here is very efficient for systems with small scale dynamics, and enables very large time steps. There are several further

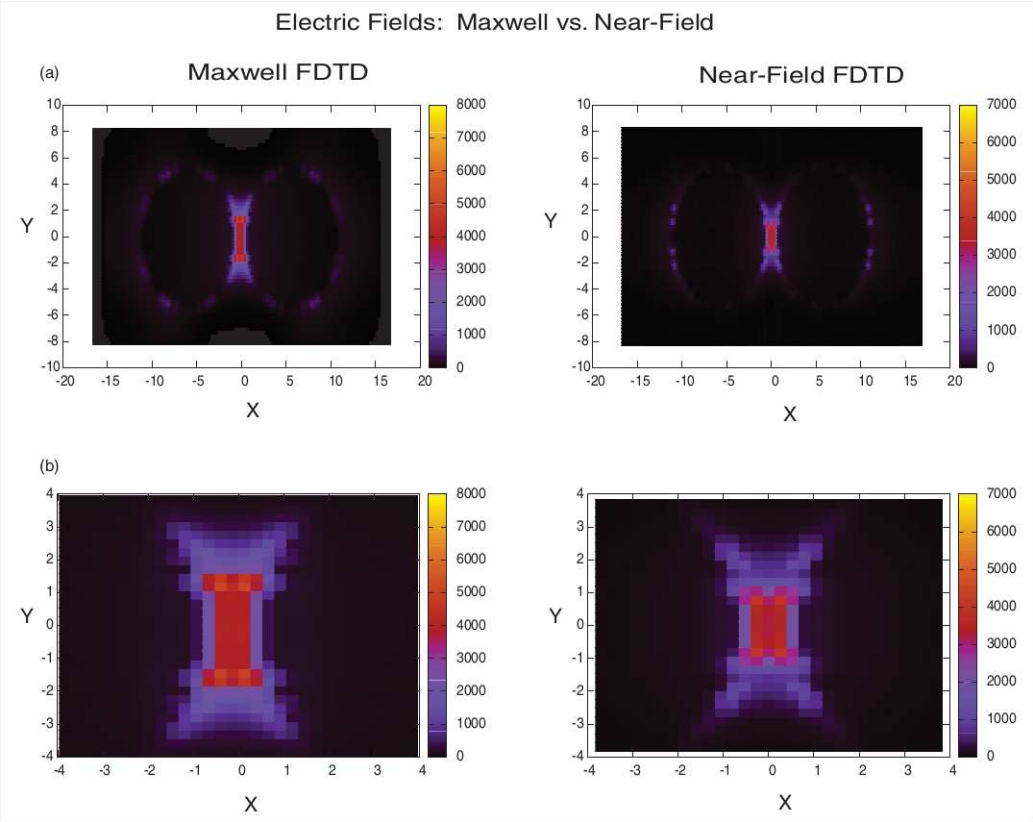

Figure 6.6: A 2D cut, near $z = 0$, of the intensity of the electric fields at $\omega = 3.26$ eV in Maxwell-FDTD and NF. All x, y distances are in nm. The top panels encompass the full dimers, while the bottom panels zoom in to the central region and show clearly the high intensity between the spheres. For comparison, the intensity of the external electric field is normalized to 1.

improvements and extensions which are discussed in detail below.

6.5.1 Convolutions and dielectrics

There are two challenges in the approach as it stands. First is the use of a convolution to get the electric field from the density; this is quasilinear in the number of points (if an FFT convolution algorithm is used), so it will not slow the approach significantly, but an alternative approach to convolution will still be

welcomed, as discussed below.

A different issue is, as mentioned, dielectrics, where the permittivity is almost constant over a large frequency range (and typically almost purely real). The difficulty is that the NF approach presented here requires that the frequency-independent term (associated with the first term in Eq. (6.2)) will be uniform (i.e., so that if a vacuum is used it equals ϵ_0), so that the Poisson equation could be easily solved. Possible solutions are as follows.

First is the combination of several terms as in Eq. (6.2) so that the sum of these terms will be fairly constant over a large frequency range; the difficulty is that then very wide Lorentzians (with large damping constants and large coefficients) will be needed, making the necessary time step quite small.

A second choice will be to use $\epsilon_\infty = const.$, i.e., the same static term for all the materials. This choice would have been useful for the description of, e.g., metals with a single dielectric (e.g., water) without vacuum, where the same ϵ_∞ constant of the dielectric could be used for ϵ_∞ of the metal (at the cost of an additional fit of the metal parameters with the new ϵ_∞.

A more elegant solution allows for dielectrics with multiple different values of ϵ_∞ and has no convolutions. In this modification, the potential will be treated as an independent Car-Parinello type variable, and its evolution will be determined by

$$\mu\ddot{\phi} = -\left(\nabla\cdot(\epsilon_s\nabla\phi) - \frac{\rho}{\epsilon_0}\right) \tag{6.21}$$

where ϵ_s is the frequency-independent part of the permittivity instead of the first term (ϵ_0) of the RHS of Eq. (6.2) for metals. Here, μ is an artificial Car-Parinello type mass. Since this equation is scalar it could be solved with a smaller time step than that used in the main set of equations of the NF approach (Eqs. (6.5) and (6.6)) without loss of efficiency.

6.5.2 Embedding and magnetic fields

We note that the NF approach as presented here is ideal for embedding into it a smaller region where the material is presented more accurately. This will amount to adding an additional "quantum" current into the system, $\boldsymbol{J}_Q$, which will be propagated by more accurate approaches; either orbital-free TDDFT, where the current is obtained by propagating a Schrödinger equation for a single orbital, or even TDDFT. The added current will be supplemented by an additional quantum density ρ_Q; embedding could be done by overlapping the two regions or by using a small transition region which will interpolate between the quantum and NF Poisson regions.

We also note that the method could potentially also be applicable to magnetic fields. While by its nature it cannot describe propagating far-field waves, it will be suitable to describe static magnetic fields or more generally near-fields due to the underlying currents.

6.5.3 Relation to FDTD features: Total-field scattered field (TF/SF) and absorbing layers

Finally, we comment on the equivalence in NF of two time-saving features in the usual Maxwell-FDTD.[ref 3] The first is the TF/SF approach, where only the electric field in the inner scattered region is represented. This feature is automatically included in NF for most cases; for example, a planar incident field is represented by a spatially homogenous $\boldsymbol{E}_0$; the reason is that the k-dependence ($\exp(i\boldsymbol{k}\cdot\boldsymbol{r})$) of the incident field is ignored in NF, as it only deals with sub-wavelength features.

The second modern feature in FDTD is boundaries. Modern FDTD methods often employ the perfectly matched layers approach, which is essentially equivalent to exterior scaling in molecular scattering. NF could, in principle, have employed

a similar approach; however, in practice, reflection is less of an issue in NF since the electric fields fall off quite rapidly in the subwavelength (near-field) regime. One could also pad the grids by a gradually rising layer of a conducting material, which will absorb any electric field which impinges on the boundaries.

References

[1] P. B. Johnson and R. W. Christy, Optical constants of the noble metals, *Phys. Rev. B* **6**, 4370 (1972).

[2] M. L. Tiago and J. R. Chelikowsky, Optical excitations in organic molecules, clusters, and defects studied by first-principles green's function methods, *Phys. Rev. B* **73**, 205334 (2006).

[3] S. Öğüt, J. R. Chelikowsky, and S. G. Louie, Quantum confinement and optical gaps in si nanocrystals, *Phys. Rev. Lett.* **79**, 1770 (1997).

[4] R. Reslan, K. Lopata, C. Arntsen, N. Govind, and D. Neuhauser, Electron transfer beyond the static picture: A tddft/td-zindo study of a pentacene dimer, *The Journal of Chemical Physics* **137**, (2012).

[5] J. C. Aguirre, C. Arntsen, S. Hernandez, R. Huber, A. M. Nardes, M. Halim, D. Kilbride, Y. Rubin, S. H. Tolbert, N. Kopidakis, B. J. Schwartz, and D. Neuhauser, Understanding local and macroscopic electron mobilities in the fullerene network of conjugated polymer-based solar cells: Time-resolved microwave conductivity and theory, *Advanced Functional Materials* **24**, 784 (2014).

[6] C. Arntsen, R. Reslan, S. Hernandez, Y. Gao, and D. Neuhauser, Direct delocalization for calculating electron transfer in fullerenes, *International Journal of Quantum Chemistry* **113**, 1885 (2013).

[7] D. Neuhauser, Y. Gao, C. Arntsen, C. Karshenas, E. Rabani, and R. Baer, Breaking the theoretical scaling limit for predicting quasiparticle energies: The stochastic *gw* approach, *Phys. Rev. Lett.* **113**, 076402 (2014).

[8] C. Arntsen, K. Lopata, M. R. Wall, L. Bartell, and D. Neuhauser, Modeling molecular effects on plasmon transport: Silver nanoparticles with tartrazine, *The Journal of Chemical Physics* **134**, (2011).

[9] A. Coomar, C. Arntsen, K. A. Lopata, S. Pistinner, and D. Neuhauser, Near-field: A finite-difference time-dependent method for simulation of electrodynamics on small scales, *The Journal of Chemical Physics* **135**, (2011).

[10] H. Hoppe and N. S. Sariciftci, Organic solar cells: An overview, *Journal of Materials Research* **19**, 1924 (2004).

[11] M. A. Green, K. Emery, Y. Hishikawa, W. Warta, and E. D. Dunlop, Solar cell efficiency tables (version 39), *Progress in Photovoltaics: Research and Applications* **20**, 12 (2012).

[12] J. Peet, J. Kim, N. E. Coates, W. L. Ma, D. Moses, A. J. Heeger, and G. C. Bazan, Efficiency enhancement in low-bandgap polymer solar cells by processing with alkane dithiols, *Nature materials* **6**, 497 (2007).

[13] B. A. Collins, Z. Li, J. R. Tumbleston, E. Gann, C. R. McNeill, and H. Ade, Absolute measurement of domain composition and nanoscale size distribution explains performance in ptb7:pc71bm solar cells, *Advanced Energy Materials* **3**, 65 (2013).

[14] R. A. J. Janssen and J. Nelson, Factors limiting device efficiency in organic photovoltaics, *Advanced Materials* **25**, 1847 (2013).

[15] J. Peet, C. Soci, R. C. Coffin, T. Q. Nguyen, A. Mikhailovsky, D. Moses, and G. C. Bazan, Method for increasing the photoconductive response in conjugated polymer/fullerene composites, *Applied Physics Letters* **89**, (2006).

[16] J. K. Lee, W. L. Ma, C. J. Brabec, J. Yuen, J. S. Moon, J. Y. Kim, K. Lee, G. C. Bazan, and A. J. Heeger, Processing additives for improved efficiency from bulk heterojunction solar cells, *Journal of the American Chemical Society* **130**, 3619 (2008).

[17] W. Ma, C. Yang, X. Gong, K. Lee, and A. Heeger, Thermally stable, efficient polymer solar cells with nanoscale control of the interpenetrating network morphology, *Advanced Functional Materials* **15**, 1617 (2005).

[18] K. Kim, J. Liu, M. A. G. Namboothiry, and D. L. Carroll, Roles of donor and acceptor nanodomains in 6% efficient thermally annealed polymer photovoltaics, *Applied Physics Letters* **90**, (2007).

[19] E. Verploegen, R. Mondal, C. J. Bettinger, S. Sok, M. F. Toney, and Z. Bao, Effects of thermal annealing upon the morphology of polymer-fullerene blends, *Advanced Functional Materials* **20**, 3519 (2010).

[20] A. L. Ayzner, C. J. Tassone, S. H. Tolbert, and B. J. Schwartz, Reappraising the need for bulk heterojunctions in polymerfullerene photovoltaics: The role of carrier transport in all-solution-processed p3ht/pcbm bilayer solar cells, *The Journal of Physical Chemistry C* **113**, 20050 (2009).

[21] A. M. Nardes, A. L. Ayzner, S. R. Hammond, A. J. Ferguson, B. J. Schwartz, and N. Kopidakis, Photoinduced charge carrier generation and decay in sequentially deposited polymer/fullerene layers: Bulk heterojunction vs planar interface, *The Journal of Physical Chemistry C* **116**, 7293 (2012).

[22] A. L. Ayzner, S. C. Doan, B. Tremolet de Villers, and B. J. Schwartz, Ultrafast studies of exciton migration and polaron formation in sequentially solution-processed conjugated polymer/fullerene quasi-bilayer photovoltaics, *The Journal of Physical Chemistry Letters* **3**, 2281 (2012).

[23] C. Tao, M. Aljada, P. E. Shaw, K. H. Lee, H. Cavaye, M. N. Balfour, R. J. Borthwick, M. James, P. L. Burn, I. R. Gentle, and P. Meredith, Controlling hierarchy in solution-processed polymer solar cells based on crosslinked p3ht, *Advanced Energy Materials* **3**, 105 (2013).

[24] D. H. Wang, J. S. Moon, J. Seifter, J. Jo, J. H. Park, O. O. Park, and A. J. Heeger, Sequential processing: Control of nanomorphology in bulk heterojunction solar cells, *Nano Letters* **11**, 3163 (2011).

[25] H. Li, Y.-F. Li, and J. Wang, Optimizing performance of layer-by-layer processed polymer solar cells, *Applied Physics Letters* **101**, (2012).

[26] C. W. Rochester, S. A. Mauger, and A. J. Moul, Investigating the morphology of polymer/fullerene layers coated using orthogonal solvents, *The Journal of Physical Chemistry C* **116**, 7287 (2012).

[27] A. Loiudice, A. Rizzo, M. Biasiucci, and G. Gigli, Bulk heterojunction versus diffused bilayer: The role of device geometry in solution p-doped polymer-based solar cells, *The Journal of Physical Chemistry Letters* **3**, 1908 (2012).

[28] R. A. Marcus and N. Sutin, Electron transfers in chemistry and biology, *Biochimica et Biophysica Acta (BBA)-Reviews on Bioenergetics* **811**, 265 (1985).

[29] K. V. Mikkelsen and M. A. Ratner, Electron tunneling in solid-state electron-transfer reactions, *Chemical Reviews* **87**, 113 (1987).

[30] W. Zhao, W. Ma, C. Chen, J. Zhao, and Z. Shuai, Efficient degradation of toxic organic pollutants with ni2o3/tio2-xbx under visible irradiation, *Journal of the American Chemical Society* **126**, 4782 (2004).

[31] B. ORegan and M. Gr atzel, A low-cost, high-efficiency solar cell based on dye-sensitized, *Nature* **353**, 737 (1991).

[32] W. Stier and O. V. Prezhdo, Nonadiabatic molecular dynamics simulation of light-induced electron transfer from an anchored molecular electron donor to a semiconductor acceptor, *The Journal of Physical Chemistry B* **106**, 8047 (2002).

[33] N. Tao, Electron transport in molecular junctions, *Nature Nanotechnology* **1**, 173 (2006).

[34] G. L. CLOSS and J. R. MILLER, Intramolecular long-distance electron transfer in organic molecules, *Science* **240**, 440 (1988).

[35] J.-L. Brdas, D. Beljonne, V. Coropceanu, and J. Cornil, Charge-transfer and energy-transfer processes in -conjugated oligomers and polymers: a molecular picture, *Chemical Reviews* **104**, 4971 (2004), PMID: 15535639.

[36] A. Nitzan and M. A. Ratner, Electron transport in molecular wire junctions, *Science* **300**, 1384 (2003).

[37] V. Lemaur, D. A. da Silva Filho, V. Coropceanu, M. Lehmann, Y. Geerts, J. Piris, M. G. Debije, A. M. van de Craats, K. Senthilkumar, L. D. A. Siebbeles, J. M. Warman, J.-L. Brdas, and J. Cornil, Charge transport properties in discotic liquid crystals: a quantum-chemical insight into structureproperty relationships, *Journal of the American Chemical Society* **126**, 3271 (2004), PMID: 15012158.

[38] Q. Wu and T. Van Voorhis, Extracting electron transfer coupling elements from constrained density functional theory, *The Journal of Chemical Physics* **125**, (2006).

[39] T. Stein, L. Kronik, and R. Baer, Reliable prediction of charge transfer excitations in molecular complexes using time-dependent density functional theory, *Journal of the American Chemical Society* **131**, 2818 (2009).

[40] C. Liu, D. Walter, D. Neuhauser, and R. Baer, Molecular recognition and conductance in crown ethers, *Journal of the American Chemical Society* **125**, 13936 (2003).

[41] H. Chen, M. A. Ratner, and G. C. Schatz, Time-dependent theory of the rate of photo-induced electron transfer, *The Journal of Physical Chemistry C* **115**, 18810 (2011).

[42] C.-P. Hsu, The electronic couplings in electron transfer and excitation energy transfer, *Accounts of Chemical Research* **42**, 509 (2009).

[43] L. A. Bartell, R. Reslan, M. R. Wall, R. D. Kennedy, and D. Neuhauser, Electron transfer with td-split, a linear response time-dependent method, *Chemical Physics* **391**, 62 (2011), Open problems and new solutions in time dependent density functional theory.

[44] R. J. Cave and M. D. Newton, Generalization of the mulliken-hush treatment for the calculation of electron transfer matrix elements, *Chemical Physics Letters* **249**, 15 (1996).

[45] L. A. Bartell, M. R. Wall, and D. Neuhauser, A time-dependent semiempirical approach to determining excited states, *The Journal of Chemical Physics* **132**, (2010).

[46] H. Eshuis and T. van Voorhis, The influence of initial conditions on charge transfer dynamics, *Phys. Chem. Chem. Phys.* **11**, 10293 (2009).

[47] R. J. Bartlett and M. Musiał, Coupled-cluster theory in quantum chemistry, *Rev. Mod. Phys.* **79**, 291 (2007).

[48] K. Kowalski and P. Piecuch, New coupled-cluster methods with singles, doubles, and noniterative triples for high accuracy calculations of excited electronic states, *The Journal of Chemical Physics* **120**, 1715 (2004).

[49] S. Hirata and M. Head-Gordon, Time-dependent density functional theory for radicals: An improved description of excited states with substantial double excitation character, *Chemical Physics Letters* **302**, 375 (1999).

[50] C. L. Moss, C. M. Isborn, and X. Li, Ehrenfest dynamics with a time-dependent density-functional-theory calculation of lifetimes and resonant widths of charge-transfer states of li^+ near an aluminum cluster surface, *Phys. Rev. A* **80**, 024503 (2009).

[51] K. Yabana and G. F. Bertsch, Time-dependent local-density approximation in real time, *Phys. Rev. B* **54**, 4484 (1996).

[52] A. Castro, H. Appel, M. Oliveira, C. A. Rozzi, X. Andrade, F. Lorenzen, M. A. L. Marques, E. K. U. Gross, and A. Rubio, octopus: a tool for the application of time-dependent density functional theory, *physica status solidi (b)* **243**, 2465 (2006).

[53] K. Lopata and N. Govind, Modeling fast electron dynamics with real-time time-dependent density functional theory: Application to small molecules and chromophores, *Journal of Chemical Theory and Computation* **7**, 1344 (2011).

[54] R. Baer and D. Neuhauser, Real-time linear response for time-dependent density-functional theory, *The Journal of Chemical Physics* **121**, 9803 (2004).

[55] J. D. Baker and M. C. Zerner, Applications of the random phase approximation with the indo/s hamiltonian: Uvvis spectra of free base porphin, *Chemical Physics Letters* **175**, 192 (1990).

[56] M. Valiev, E. Bylaska, N. Govind, K. Kowalski, T. Straatsma, H. V. Dam, D. Wang, J. Nieplocha, E. Apra, T. Windus, and W. de Jong, Nwchem: A comprehensive and scalable open-source solution for large scale molecular simulations, *Computer Physics Communications* **181**, 1477 (2010).

[57] M. Zerner, J. Ridley, A. Bacon, J. Head, W. Edwards, J. McKelvey, J. Cuberson, P. Knappe, M. Cory, B. Weiner, *et al.*, Zindo-mn, 2011.

[58] J. C. Slater and K. H. Johnson, Self-consistent-field $x\alpha$ cluster method for polyatomic molecules and solids, *Phys. Rev. B* **5**, 844 (1972).

[59] S. H. Vosko, L. Wilk, and M. Nusair, Accurate spin-dependent electron liquid correlation energies for local spin density calculations: a critical analysis, *Canadian Journal of Physics* **58**, 1200 (1980).

[60] J. P. Perdew, K. Burke, and M. Ernzerhof, Generalized gradient approximation made simple, *Phys. Rev. Lett.* **77**, 3865 (1996).

[61] P. J. Stephens, F. J. Devlin, C. F. Chabalowski, and M. J. Frisch, Ab initio calculation of vibrational absorption and circular dichroism spectra using density functional force fields, *The Journal of Physical Chemistry* **98**, 11623 (1994).

[62] P. A. Troshin, H. Hoppe, J. Renz, M. Egginger, J. Y. Mayorova, A. E. Goryachev, A. S. Peregudov, R. N. Lyubovskaya, G. Gobsch, N. S. Sariciftci, and V. F. Razumov, Material solubility-photovoltaic performance relationship in the design of novel fullerene derivatives for bulk heterojunction solar cells, *Advanced Functional Materials* **19**, 779 (2009).

[63] Y. Liang and L. Yu, A new class of semiconducting polymers for bulk heterojunction solar cells with exceptionally high performance, *Accounts of Chemical Research* **43**, 1227 (2010).

[64] C. J. Tassone, A. L. Ayzner, R. D. Kennedy, M. Halim, M. So, Y. Rubin, S. H. Tolbert, and B. J. Schwartz, Using pentaarylfullerenes to understand network formation in conjugated polymer-based bulk-heterojunction solar cells, *The Journal of Physical Chemistry C* **115**, 22563 (2011).

[65] R. D. Kennedy, M. Halim, S. I. Khan, B. J. Schwartz, S. H. Tolbert, and Y. Rubin, Crystal-packing trends for a series of 6,9,12,15,18-pentaaryl-1-hydro[60]fullerenes, *Chemistry A European Journal* **18**, 7418 (2012).

[66] M. T. Rispens, A. Meetsma, R. Rittberger, C. J. Brabec, N. S. Sariciftci, and J. C. Hummelen, Influence of the solvent on the crystal structure of pcbm and the efficiency of mdmo-ppv:pcbm 'plastic' solar cells, *Chem. Commun.* , 2116 (2003).

[67] R. D. Kennedy, A. L. Ayzner, D. D. Wanger, C. T. Day, M. Halim, S. I. Khan, S. H. Tolbert, B. J. Schwartz, and Y. Rubin, Self-assembling fullerenes for improved bulk-heterojunction photovoltaic devices, *Journal of the American Chemical Society* **130**, 17290 (2008).

[68] C. E. D. CHIDSEY, Free energy and temperature dependence of electron transfer at the metal-electrolyte interface, *Science* **251**, 919 (1991).

[69] R. C. I. MacKenzie, J. M. Frost, and J. Nelson, A numerical study of mobility in thin films of fullerene derivatives, *The Journal of Chemical Physics* **132**, (2010).

[70] H. Hoppe and N. S. Sariciftci, Morphology of polymer/fullerene bulk heterojunction solar cells, *J. Mater. Chem.* **16**, 45 (2006).

[71] G. Li, V. Shrotriya, Y. Yao, J. Huang, and Y. Yang, Manipulating regioregular poly(3-hexylthiophene) : [6,6]-phenyl-c61-butyric acid methyl ester blends-route towards high efficiency polymer solar cells, *J. Mater. Chem.* **17**, 3126 (2007).

[72] L. Hedin, New method for calculating the one-particle green's function with application to the electron-gas problem, *Phys. Rev.* **139**, A796 (1965).

[73] C. Friedrich and A. Schindlmayr, Many-body perturbation theory: the gw approximation, *NIC Series* **31**, 335 (2006).

[74] A. Fetter and J. Walecka, *Quantum Theory of Many-Particle Physics*, McGraw-Hill, New York, 1971.

[75] M. S. Hybertsen and S. G. Louie, First-principles theory of quasiparticles: Calculation of band gaps in semiconductors and insulators, *Phys. Rev. Lett.* **55**, 1418 (1985).

[76] M. S. Hybertsen and S. G. Louie, Electron correlation in semiconductors and insulators: Band gaps and quasiparticle energies, *Phys. Rev. B* **34**, 5390 (1986).

[77] W. G. Aulbur, M. Städele, and A. Görling, Exact-exchange-based quasiparticle calculations, *Phys. Rev. B* **62**, 7121 (2000).

[78] A. Stan, N. E. Dahlen, and R. van Leeuwen, Fully self-consistent gw calculations for atoms and molecules, *EPL (Europhysics Letters)* **76**, 298 (2006).

[79] M. Shishkin and G. Kresse, Self-consistent *gw* calculations for semiconductors and insulators, *Phys. Rev. B* **75**, 235102 (2007).

[80] P. Huang and E. A. Carter, Advances in correlated electronic structure methods for solids, surfaces, and nanostructures, *Annual Review of Physical Chemistry* **59**, 261 (2008), PMID: 18031211.

[81] P. E. Trevisanutto, C. Giorgetti, L. Reining, M. Ladisa, and V. Olevano, Ab initio gw many-body effects in graphene, *Phys. Rev. Lett.* **101**, 226405 (2008).

[82] C. Rostgaard, K. W. Jacobsen, and K. S. Thygesen, Fully self-consistent gw calculations for molecules, *Phys. Rev. B* **81**, 085103 (2010).

[83] P. Liao and E. A. Carter, Testing variations of the gw approximation on strongly correlated transition metal oxides: hematite ([small alpha]-fe2o3) as a benchmark, *Phys. Chem. Chem. Phys.* **13**, 15189 (2011).

[84] J. A. Berger, L. Reining, and F. Sottile, Efficient *gw* calculations for sno_2, zno, and rubrene: The effective-energy technique, *Phys. Rev. B* **85**, 085126 (2012).

[85] N. Marom, F. Caruso, X. Ren, O. T. Hofmann, T. Körzdörfer, J. R. Chelikowsky, A. Rubio, M. Scheffler, and P. Rinke, Benchmark of *gw* methods for azabenzenes, *Phys. Rev. B* **86**, 245127 (2012).

[86] M. J. van Setten, F. Weigend, and F. Evers, The gw-method for quantum chemistry applications: Theory and implementation, *Journal of Chemical Theory and Computation* **9**, 232 (2013).

[87] L. Y. Isseroff and E. A. Carter, Importance of reference hamiltonians containing exact exchange for accurate one-shot *gw* calculations of cu_2o, *Phys. Rev. B* **85**, 235142 (2012).

[88] S. Refaely-Abramson, S. Sharifzadeh, N. Govind, J. Autschbach, J. B. Neaton, R. Baer, and L. Kronik, Quasiparticle spectra from a nonempirical optimally tuned range-separated hybrid density functional, *Phys. Rev. Lett.* **109**, 226405 (2012).

[89] F. Caruso, P. Rinke, X. Ren, A. Rubio, and M. Scheffler, Self-consistent *gw*: All-electron implementation with localized basis functions, *Phys. Rev. B* **88**, 075105 (2013).

[90] J. C. Grossman, M. Rohlfing, L. Mitas, S. G. Louie, and M. L. Cohen, High accuracy many-body calculational approaches for excitations in molecules, *Phys. Rev. Lett.* **86**, 472 (2001).

[91] G. Onida, L. Reining, and A. Rubio, Electronic excitations: density-functional versus many-body green's-function approaches, *Rev. Mod. Phys.* **74**, 601 (2002).

[92] S. Refaely-Abramson, R. Baer, and L. Kronik, Fundamental and excitation gaps in molecules of relevance for organic photovoltaics from an optimally tuned range-separated hybrid functional, *Phys. Rev. B* **84**, 075144 (2011).

[93] F. Caruso, P. Rinke, X. Ren, M. Scheffler, and A. Rubio, Unified description of ground and excited states of finite systems: The self-consistent *gw* approach, *Phys. Rev. B* **86**, 081102 (2012).

[94] X. Blase, C. Attaccalite, and V. Olevano, First-principles *GW* calculations for fullerenes, porphyrins, phtalocyanine, and other molecules of interest for organic photovoltaic applications, *Phys. Rev. B* **83**, 115103 (2011).

[95] S. V. Faleev, M. van Schilfgaarde, and T. Kotani, All-electron self-consistent *gw* approximation: Application to si, mno, and nio, *Phys. Rev. Lett.* **93**, 126406 (2004).

[96] S. Y. Quek, L. Venkataraman, H. J. Choi, S. G. Louie, M. S. Hybertsen, and J. B. Neaton, Aminegold linked single-molecule circuits: experiment and theory, *Nano Letters* **7**, 3477 (2007), PMID: 17900162.

[97] S. Y. Quek, J. B. Neaton, M. S. Hybertsen, E. Kaxiras, and S. G. Louie, Negative differential resistance in transport through organic molecules on silicon, *Phys. Rev. Lett.* **98**, 066807 (2007).

[98] K. S. Thygesen and A. Rubio, Conserving *gw* scheme for nonequilibrium quantum transport in molecular contacts, *Phys. Rev. B* **77**, 115333 (2008).

[99] P. Myöhänen, A. Stan, G. Stefanucci, and R. van Leeuwen, Kadanoff-baym approach to quantum transport through interacting nanoscale systems: From the transient to the steady-state regime, *Phys. Rev. B* **80**, 115107 (2009).

[100] M. DellAngela, G. Kladnik, A. Cossaro, A. Verdini, M. Kamenetska, I. Tamblyn, S. Y. Quek, J. B. Neaton, D. Cvetko, A. Morgante, and L. Venkataraman, Relating energy level alignment and amine-linked single molecule junction conductance, *Nano Letters* **10**, 2470 (2010).

[101] J. B. Neaton, M. S. Hybertsen, and S. G. Louie, Renormalization of molecular electronic levels at metal-molecule interfaces, *Phys. Rev. Lett.* **97**, 216405 (2006).

[102] I. Tamblyn, P. Darancet, S. Y. Quek, S. A. Bonev, and J. B. Neaton, Electronic energy level alignment at metal-molecule interfaces with a *gw* approach, *Phys. Rev. B* **84**, 201402 (2011).

[103] H.-V. Nguyen, T. A. Pham, D. Rocca, and G. Galli, Improving accuracy and efficiency of calculations of photoemission spectra within the many-body perturbation theory, *Phys. Rev. B* **85**, 081101 (2012).

[104] J. Deslippe, G. Samsonidze, D. A. Strubbe, M. Jain, M. L. Cohen, and S. G. Louie, Berkeleygw: A massively parallel computer package for the calculation of the quasiparticle and optical properties of materials and nanostructures, *Computer Physics Communications* **183**, 1269 (2012).

[105] T. A. Pham, H.-V. Nguyen, D. Rocca, and G. Galli, Gw calculations using the spectral decomposition of the dielectric matrix: Verification, validation, and comparison of methods, *Phys. Rev. B* **87**, 155148 (2013).

[106] D. Foerster, P. Koval, and D. Snchez-Portal, An o(n3) implementation of hedin's gw approximation for molecules, *The Journal of Chemical Physics* **135**, (2011).

[107] X. Gonze, B. Amadon, P.-M. Anglade, J.-M. Beuken, F. Bottin, P. Boulanger, F. Bruneval, D. Caliste, R. Caracas, M. Ct, T. Deutsch, L. Genovese, P. Ghosez, M. Giantomassi, S. Goedecker, D. Hamann, P. Hermet, F. Jollet, G. Jomard, S. Leroux, M. Mancini, S. Mazevet,

M. Oliveira, G. Onida, Y. Pouillon, T. Rangel, G.-M. Rignanese, D. Sangalli, R. Shaltaf, M. Torrent, M. Verstraete, G. Zerah, and J. Zwanziger, Abinit: First-principles approach to material and nanosystem properties, *Computer Physics Communications* **180**, 2582 (2009), 40 {YEARS} {OF} CPC: A celebratory issue focused on quality software for high performance, grid and novel computing architectures.

[108] R. Baer and E. Rabani, Expeditious stochastic calculation of multiexciton generation rates in semiconductor nanocrystals, *Nano Letters* **12**, 2123 (2012).

[109] D. Neuhauser, E. Rabani, and R. Baer, Expeditious stochastic approach for mp2 energies in large electronic systems, *Journal of Chemical Theory and Computation* **9**, 24 (2013).

[110] D. Neuhauser, E. Rabani, and R. Baer, Expeditious stochastic calculation of random-phase approximation energies for thousands of electrons in three dimensions, *The Journal of Physical Chemistry Letters* **4**, 1172 (2013).

[111] R. Baer, D. Neuhauser, and E. Rabani, Self-averaging stochastic kohn-sham density-functional theory, *Phys. Rev. Lett.* **111**, 106402 (2013).

[112] Q. Ge, Y. Gao, R. Baer, E. Rabani, and D. Neuhauser, A guided stochastic energy-domain formulation of the second order mllerplesset perturbation theory, *The Journal of Physical Chemistry Letters* **5**, 185 (2014).

[113] L. W. Wang and A. Zunger, Electronic structure pseudopotential calculations of large (.apprx.1000 atoms) si quantum dots, *The Journal of Physical Chemistry* **98**, 2158 (1994).

[114] D. Neuhauser, Bound state eigenfunctions from wave packets: Timeenergy resolution, *The Journal of Chemical Physics* **93**, 2611 (1990).

[115] M. Hutchinson, A stochastic estimator of the trace of the influence matrix for laplacian smoothing splines, *Communications in Statistics - Simulation and Computation* **18**, 1059 (1989).

[116] D. A. Drabold and O. F. Sankey, Maximum entropy approach for linear scaling in the electronic structure problem, *Phys. Rev. Lett.* **70**, 3631 (1993).

[117] L.-W. Wang, Calculating the density of states and optical-absorption spectra of large quantum systems by the plane-wave moments method, *Phys. Rev. B* **49**, 10154 (1994).

[118] R. Silver, H. Roeder, A. Voter, and J. Kress, *Maximum Entropy and Bayesian Methods*, Springer, Berlin, 1996.

[119] R. Kosloff, Time-dependent quantum-mechanical methods for molecular dynamics, *The Journal of Physical Chemistry* **92**, 2087 (1988).

[120] R. Kosloff, Propagation methods for quantum molecular dynamics, *Annual Review of Physical Chemistry* **45**, 145 (1994).

[121] S. Baroni, S. de Gironcoli, A. Dal Corso, and P. Giannozzi, Phonons and related crystal properties from density-functional perturbation theory, *Rev. Mod. Phys.* **73**, 515 (2001).

[122] D. Neuhauser and R. Baer, Efficient linear-response method circumventing the exchange-correlation kernel: Theory for molecular conductance under finite bias, *The Journal of Chemical Physics* **123**, (2005).

[123] E. Runge and E. K. U. Gross, Density-functional theory for time-dependent systems, *Phys. Rev. Lett.* **52**, 997 (1984).

[124] N. Troullier and J. L. Martins, Efficient pseudopotentials for plane-wave calculations, *Phys. Rev. B* **43**, 1993 (1991).

[125] L. Kronik, T. Stein, S. Refaely-Abramson, and R. Baer, Excitation gaps of finite-sized systems from optimally tuned range-separated hybrid functionals, *Journal of Chemical Theory and Computation* **8**, 1515 (2012).

[126] T. Stein, J. Autschbach, N. Govind, L. Kronik, and R. Baer, Curvature and frontier orbital energies in density functional theory, *The Journal of Physical Chemistry Letters* **3**, 3740 (2012).

[127] B. W. Larson, J. B. Whitaker, X.-B. Wang, A. A. Popov, G. Rumbles, N. Kopidakis, S. H. Strauss, and O. V. Boltalina, Electron affinity of phenylc61butyric acid methyl ester (pcbm), *The Journal of Physical Chemistry C* **117**, 14958 (2013).

[128] K. Akaike, K. Kanai, H. Yoshida, J. Tsutsumi, T. Nishi, N. Sato, Y. Ouchi, and K. Seki, Ultraviolet photoelectron spectroscopy and inverse photoemission spectroscopy of [6,6]-phenyl-c61-butyric acid methyl ester in gas and solid phases, *Journal of Applied Physics* **104**, (2008).

[129] R. Del Sole, L. Reining, and R. W. Godby, Gwγ approximation for electron self-energies in semiconductors and insulators, *Phys. Rev. B* **49**, 8024 (1994).

[130] J. Linderberg and Y. Öhrn, *Propagators in quantum chemistry*, John Wiley & Sons, New York, 2004.

[131] M. M. Rieger, L. Steinbeck, I. White, H. Rojas, and R. Godby, The {GW} space-time method for the self-energy of large systems, *Computer Physics Communications* **117**, 211 (1999).

[132] G. Samsonidze, M. Jain, J. Deslippe, M. L. Cohen, and S. G. Louie, Simple approximate physical orbitals for *gw* quasiparticle calculations, *Phys. Rev. Lett.* **107**, 186404 (2011).

[133] A. J. Haes, C. L. Haynes, A. D. McFarland, G. C. Schatz, R. P. Van Duyne, and S. Zou, Plasmonic materials for surface-enhanced sensing and spectroscopy, *MRS Bulletin* **30**, 368 (2005).

[134] W. Murray and W. Barnes, Plasmonic materials, *Advanced Materials* **19**, 3771 (2007).

[135] S. Link and M. A. El-Sayed, Size and temperature dependence of the plasmon absorption of colloidal gold nanoparticles, *The Journal of Physical Chemistry B* **103**, 4212 (1999).

[136] C. Burda, X. Chen, R. Narayanan, and M. A. El-Sayed, Chemistry and properties of nanocrystals of different shapes, *Chemical Reviews* **105**, 1025 (2005).

[137] S. A. Maier, P. G. Kik, and H. A. Atwater, Observation of coupled plasmon-polariton modes in au nanoparticle chain waveguides of different lengths: Estimation of waveguide loss, *Applied Physics Letters* **81**, 1714 (2002).

[138] S. A. Maier, P. G. Kik, H. A. Atwater, S. Meltzer, E. Harel, B. E. Koel, and A. A. Requicha, Local detection of electromagnetic energy transport below the diffraction limit in metal nanoparticle plasmon waveguides, *Nature materials* **2**, 229 (2003).

[139] L. Yin, V. K. Vlasko-Vlasov, J. Pearson, J. M. Hiller, J. Hua, U. Welp, D. E. Brown, and C. W. Kimball, Subwavelength focusing and guiding of surface plasmons, *Nano Letters* **5**, 1399 (2005).

[140] J. Dintinger, S. Klein, and T. Ebbesen, Moleculesurface plasmon interactions in hole arrays: Enhanced absorption, refractive index changes, and all-optical switching, *Advanced Materials* **18**, 1267 (2006).

[141] S. Nie and S. R. Emory, Probing single molecules and single nanoparticles by surface-enhanced raman scattering, *Science* **275**, 1102 (1997).

[142] S. Mackowski, S. Wrmke, A. J. Maier, T. H. P. Brotosudarmo, H. Harutyunyan, A. Hartschuh, A. O. Govorov, H. Scheer, and C. Bruchle, Metal-enhanced fluorescence of chlorophylls in single light-harvesting complexes, *Nano Letters* **8**, 558 (2008).

[143] J. Zhao, L. Jensen, J. Sung, S. Zou, G. C. Schatz, and R. P. Van Duyne, Interaction of plasmon and molecular resonances for rhodamine 6g adsorbed on silver nanoparticles, *Journal of the American Chemical Society* **129**, 7647 (2007).

[144] K. Lopata and D. Neuhauser, Multiscale maxwellschrdinger modeling: A split field finite-difference time-domain approach to molecular nanopolaritonics, *The Journal of Chemical Physics* **130**, (2009).

[145] D. Neuhauser and K. Lopata, Molecular nanopolaritonics: Cross manipulation of near-field plasmons and molecules. i. theory and application to junction control, *The Journal of Chemical Physics* **127**, (2007).

[146] A. Taflove and S. C. Hagness, *Computationai Electrodynamics: The Finite-Difference Time-Domain Method*, Artech House, Boston, 2005.

[147] S. K. Gray and T. Kupka, Propagation of light in metallic nanowire arrays: Finite-difference time-domain studies of silver cylinders, *Phys. Rev. B* **68**, 045415 (2003).

[148] J. J. P. Stewart, Optimization of parameters for semiempirical methods i. method, *Journal of Computational Chemistry* **10**, 209 (1989).

[149] A. Vial, A.-S. Grimault, D. Macias, D. Barchiesi, and M. L. de la Chapelle, Improved analytical fit of gold dispersion: Application to the modeling of extinction spectra with a finite-difference time-domain method, *Phys. Rev. B* **71**, 085416 (2005).

[150] V. Bagirova and L. Mit'kina, Determination of tartrazine in drugs, *Pharmaceutical Chemistry Journal* **37**, 558 (2003).

[151] A. Taflove, Review of the formulation and applications of the finite-difference time-domain method for numerical modeling of electromagnetic wave interactions with arbitrary structures, *Wave Motion* **10**, 547 (1988), Special Issue on Numerical Methods for Electromagnetic Wave Interactions.

[152] K. Shlager and J. Schneider, A selective survey of the finite-difference time-domain literature, *Antennas and Propagation Magazine, IEEE* **37**, 39 (1995).

[153] C. Girard, Near fields in nanostructures, *Reports on Progress in Physics* **68**, 1883 (2005).

[154] B. T. Draine and P. J. Flatau, Discrete-dipole approximation for scattering calculations, *J. Opt. Soc. Am. A* **11**, 1491 (1994).

[155] M. Yurkin and A. Hoekstra, The discrete dipole approximation: An overview and recent developments, *Journal of Quantitative Spectroscopy and Radiative Transfer* **106**, 558 (2007), {IX} Conference on Electromagnetic and Light Scattering by Non-Spherical Particles.

[156] T. Jensen, L. Kelly, A. Lazarides, and G. Schatz, Electrodynamics of noble metal nanoparticles and nanoparticle clusters, *Journal of Cluster Science* **10**, 295 (1999).

[157] P. Nordlander and E. Prodan, Plasmon hybridization in nanoparticles near metallic surfaces, *Nano Letters* **4**, 2209 (2004).

[158] D. J. Masiello and G. C. Schatz, On the linear response and scattering of an interacting molecule-metal system, *The Journal of Chemical Physics* **132**, (2010).

[159] Y. Sivan, S. Xiao, U. K. Chettiar, A. V. Kildishev, and V. M. Shalaev, Frequency-domain simulations of a negative-index material with embedded gain, *Opt. Express* **17**, 24060 (2009).

[160] K. Lopata and D. Neuhauser, Nonlinear nanopolaritonics: Finite-difference time-domain maxwellschrdinger simulation of molecule-assisted plasmon transfer, *The Journal of Chemical Physics* **131**, (2009).

[161] F. Hao and P. Nordlander, Efficient dielectric function for {FDTD} simulation of the optical properties of silver and gold nanoparticles, *Chemical Physics Letters* **446**, 115 (2007).

[162] P. Nordlander, C. Oubre, E. Prodan, K. Li, and M. I. Stockman, Plasmon hybridization in nanoparticle dimers, *Nano Letters* **4**, 899 (2004).